NASA/TM–20210024081

Test and Analysis of the 8-foot Diameter Cylindrical Sandwich Composite Test Article CTA8.2B

As part of the NASA Engineering and Safety Center Shell Buckling Knockdown Factor Project

Cyrus J. R. Kosztowny, Kyongchan Song, Marc R. Schultz, Nathaniel W. Gardner, and Adam Przekop
Langley Research Center, Hampton, Virginia

Michelle Tillotson Rudd
Marshall Space Flight Center, Huntsville, Alabama

July 2024

NASA STI Program Report Series

Since its founding, NASA has been dedicated to the advancement of aeronautics and space science. The NASA scientific and technical information (STI) program plays a key part in helping NASA maintain this important role.

The NASA STI program operates under the auspices of the Agency Chief Information Officer. It collects, organizes, provides for archiving, and disseminates NASA's STI. The NASA STI program provides access to the NTRS Registered and its public interface, the NASA Technical Reports Server, thus providing one of the largest collections of aeronautical and space science STI in the world. Results are published in both non-NASA channels and by NASA in the NASA STI Report Series, which includes the following report types:

- TECHNICAL PUBLICATION. Reports of completed research or a major significant phase of research that present the results of NASA Programs and include extensive data or theoretical analysis. Includes compilations of significant scientific and technical data and information deemed to be of continuing reference value. NASA counterpart of peer-reviewed formal professional papers but has less stringent limitations on manuscript length and extent of graphic presentations.

- TECHNICAL MEMORANDUM. Scientific and technical findings that are preliminary or of specialized interest, e.g., quick release reports, working papers, and bibliographies that contain minimal annotation. Does not contain extensive analysis.

- CONTRACTOR REPORT. Scientific and technical findings by NASA-sponsored contractors and grantees.

- CONFERENCE PUBLICATION. Collected papers from scientific and technical conferences, symposia, seminars, or other meetings sponsored or co-sponsored by NASA.

- SPECIAL PUBLICATION. Scientific, technical, or historical information from NASA programs, projects, and missions, often concerned with subjects having substantial public interest.

- TECHNICAL TRANSLATION. English-language translations of foreign scientific and technical material pertinent to NASA's mission.

Specialized services also include organizing and publishing research results, distributing specialized research announcements and feeds, providing information desk and personal search support, and enabling data exchange services.

For more information about the NASA STI program, see the following:

- Access the NASA STI program home page at http://www.sti.nasa.gov

- Help desk contact information:

https://www.sti.nasa.gov/sti-contact-form/
and select the "General" help request type.

NASA/TM–20210024081

Test and Analysis of the 8-foot Diameter Cylindrical Sandwich Composite Test Article CTA8.2B

As part of the NASA Engineering and Safety Center Shell Buckling Knockdown Factor Project

Cyrus J. R. Kosztowny, Kyongchan Song, Marc R. Schultz, Nathaniel W. Gardner, and Adam Przekop
Langley Research Center, Hampton, Virginia

Michelle Tillotson Rudd
Marshall Space Flight Center, Huntsville, Alabama

National Aeronautics and
Space Administration

Langley Research Center
Hampton, Virginia 23681-2199

July 2024

Acknowledgments

This work was conducted as part of the NASA Engineering and Safety Center (NESC) Shell Buckling Knockdown Factor Project, NESC assessment number 07-010-E. The CTA8.2B test article was manufactured in an autoclave process by the Composite Technology Center at MSFC (EM42) under the direction of Will Guin and John Bausano.

The testing was performed under the direction of Nicholas Hall and Lucas Day by the Structural Strength Test Group (ET30) at MSFC.

The authors would also like to thank Michael Lindell (LaRC) for his work in generating scripts used in postprocessing analysis data for many of the composite SBKF tests.

Available from:

NASA STI Program / Mail Stop 050
NASA Langley Research Center
Hampton, VA 23681-2199

Table of Contents

List of Figures

List of Tables

Nomenclature

3D	Three-dimensional
AFT	Aft end of the test article
CTA8.2B	Cylindrical sandwich composite test article SBKF-P3-CYL-CTA8.2B
D312	LaRC Structural Mechanics and Concepts Branch
DAS	Data acquisition system
DIC	Digital image correlation
DoF	Degrees of freedom
EDI	Electronic displacement indicator
ET30	MSFC Structural Strength Test Group
FEA	Finite element analysis
FEM	Finite element model
FWD	Forward end of the test article
gsm	Gram per square meter
HS-DIC	High speed digital image correlation
IML	Inner mold line
kips	1,000 pounds
LaRC	Langley Research Center
LCS	Load Control System
LS	Load sequence
LTAE	Load Test Annex East
M_{cr}	Linear critical buckling bending moment
MSFC	Marshall Space Flight Center
NDE	Nondestructive evaluation
NESC	NASA Engineering and Safety Center
OML	Outer mold line
P_{cr}	Linear critical buckling uniformly distributed axial compressive force obtained from perfect finite element model
P_{cr}^{CL}	Linear critical buckling combined axial compression and bending force obtained from perfect finite element model
P_{cr}^{NL}	Geometrically nonlinear critical buckling uniformly distributed axial compressive force obtained from finite element model with geometric imperfections
pcf	Pound per cubic foot
psf	Pound per square foot
SBKF	Shell Buckling Knockdown Factor Project
SLS	Space Launch System
SLTMAS	Structural Loads Test Measurement Acquisition System
TA	Test article
δ_{DxxxA}	Axial displacement measurements measured with or calculated from electronic displacement indicators where “xxx” denotes specific indicators

1.0 Introduction

The buckling response of thin-walled cylindrical structures have long been shown to be sensitive to various imperfections. That is, imperfections related to load introduction, boundary conditions, material property variation, and geometric deviations can all contribute to experimentally obtained buckling loads being lower than the buckling loads predicted for perfect representations of the same thin-walled cylindrical structure [1]. To account for the influence of geometry-based imperfections of a thin-walled cylindrical structure on buckling response, a design factor (also known as a buckling knockdown factor) is used during the design phase. Guidelines for buckling knockdown factors are readily available in NASA SP-8007, Buckling of Thin Walled Circular Cylinders [2], which was updated in 2020. Prior to this recent update, NASA SP-8007 had not been updated since 1969, and since that time, computational analysis, experimental testing, and manufacturing methods have significantly improved. The NASA Engineering and Safety Center (NESC) Shell Buckling Knockdown Factor Project (SBKF, NESC Assessment 07-010-E) had the goal of developing buckling design recommendations for select classes of metallic and composite launch-vehicle structures [3]. Specifically, the test and analysis results from the fourth SBKF composite test article SBKF-P3-CYL-CTA8.2B, which is referred to as CTA8.2B, are described in this paper. This test was the fourth in a series of four tests on sandwich composite cylinders that will be used to experimentally validate analysis methods, which in turn can be used to develop new analysis-based shell buckling design guidelines for typical sandwich composite launch-vehicle cylindrical structures. Publications describing previous test validation with analysis are available in Refs. [4–6]. CTA8.2B was designed to occupy one corner of the design space with approximately equal bending stiffnesses in the axial and transverse directions and have a larger ratio of radius to effective shell thickness. Each test article had a unique design and was designed to occupy a specific region of the design space. CTA8.2B was an 8-foot diameter honeycomb-core sandwich cylinder that was fabricated and tested at the NASA Marshall Space Flight Center (MSFC). The primary objectives of this test were to interrogate the structural capability of a composite test article, and to verify the test article design and analysis approach for cylinders subjected to axial compression and combined axial and bending loads.

First, descriptions of the test article design and test are given in Section 2.0, and modeling and analysis methods used in support of the test article design and testing activities are described briefly in Section 3.0. Then, select test results are presented and compared to predicted results in Section 4.0, and concluding remarks are presented in Section 5.0. Finally, drawings of CTA8.2B and references used to support the test and analysis are provided in the Appendix.

2.0 Test Description

CTA8.2B and corresponding test system and facilities were designed to enable the buckling testing of relevant launch-vehicle-like thin-walled cylindrical structures. The test article was designed to be representative of a typical composite launch-vehicle cylinder. However, CTA8.2B was not designed to be representative of any specific previous, current, or future launch-vehicle structure. The testing of CTA8.2B occurred from October 26 through November 2, 2020 in the Load Test Annex East (LTAE) in Building 4619 at MSFC under the direction of the Structural Strength Test Group (ET30). A special-purpose test apparatus was designed and fabricated for the SBKF test effort. The test apparatus was designed to apply up to 1.5 million pounds of total force in axial compression and bending. A load control system (LCS) was used to apply the test loads and included load control and displacement control options. Numerous types of instrumentation and photographic/video systems were utilized during the test and include strain gages, displacement transducers, load cells, and low-speed and high-speed digital image correlation (DIC). This section contains a brief overview of the test objectives, test article, instrumentation, test facility, and test load sequences. Additional details on the testing of CTA8.2B can be found in the test plan [7] and test and checkout procedure [8].

2.1 Test Objective

CTA8.2B was the fourth and final composite test article designed and tested as part of the SBKF project. The test had the following primary objectives:

- Obtain test data to verify the predicted behavioral characteristics of the as-designed, as-built test article subjected to a uniform axial compression load and a combination of axial compression and bending load.
- Obtain test data for analysis-tool and model validation.

2.2 Test Article

The 8-ft diameter, 100-in. long test article CTA8.2B was designed by researchers at the NASA Langley Research Center (LaRC) in the Structural Mechanics and Concepts Branch (D312). The CTA8.2B facesheets were manufactured with an automated fiber placement robotic machine, the core was placed by hand, and then subjected to an autoclave process for cure by the Composite Technology Center (EM42) at the NASA Marshall Space Flight Center (MSFC). The honeycomb-core sandwich composite shell was constructed with carbon-epoxy facesheets composed of unidirectional IM7/8552-1 carbon fiber-epoxy 190 grams per square meter (gsm) towpreg and aluminum core (Hexcel 3.1-1/8-0.0007N-5056 and Hexcel 8.1-1/8-0.002N-5056) as provided in the fabrication drawing (Figure 57 in the Appendix).

2.2.1 Design

CTA8.2B was intentionally designed to fail by global buckling prior to any local-buckling or structural-strength failure. A maximum-strain material failure criterion was used in addition to other sandwich composite failure criteria to ensure core shear crimping, facesheet wrinkling, and facesheet dimpling, core crushing, facesheet rupture, core transverse shear-strength, and other failure modes had acceptable margins. The test article had co-cured padup plies at each end to facilitate uniform load introduction and minimize localized effects and excessive bending near the attachment rings. The padups, additional unidirectional plies to locally thicken the facesheets near the forward (FWD) end of the test article and the aft (AFT) end of the test article, were also intended to help the global buckling to initiate in the acreage region of the test article and away from either end. The quasi-isotropic 6-ply facesheets had a total layup of $[60/\text{-}60/0]_s$ and the core was 0.20-in. thick. A thin 0.06 pound per square foot (psf) Cytec FM 300-2M adhesive film was used to adhere the core to each facesheet, and Henkel Hysol EA 9396.6MD epoxy paste adhesive was used as a core-splice adhesive to join separate core sheets as provided in the layup drawing (Figure 58 in the Appendix). In the first 10 inches from each end of the test article (all dimensions are given in the final trimmed configuration as shown in Figure 59 in the Appendix), both inner mold line (IML) and outer mold line (OML) facesheet padups contained four padup plies interleaved with the acreage plies resulting in the thickest layup shown in Table 1. Also in the first 10 inches from both ends, Hexcel 8.1-1/8-0.002N-5056 aluminum core was used. This 8.1 pound per cubic foot (pcf) core was of greater density than the 3.1 pcf core used in the central 80 inches of the test-article design. In the next 4 in., both IML and OML padups comprised the same layup as the first 10 inches except with Hexcel 3.1-1/8-0.0007N-5056 aluminum core. One padup ply was dropped from each of the IML and OML facesheets at 13.5 in., 14.5 in., 18.0 in., and 20.0 in. The stacking sequences corresponding to each of the localized layups are also shown in Table 1. Since only one (+ or -) 45° padup ply was dropped at a time, the individual facesheets between 13.5 in. and 20.0 in. stations were not symmetric. However, the sandwich composite design was symmetric about the core midsurface. The test article was manufactured on a constant-diameter tool. As such, the additional thickness of the padups shifted the sandwich composite midsurface to the OML direction when compared to the acreage section containing the fewest number of plies. The acreage region between the padups was 60 inches long and was considered the main region of interest during the experimental test and analysis effort.

The approximate weight of the test article without the metallic attachment rings was 228.0 lb. The nominal weight of the design was estimated at 217.6 lb. This estimate included estimates for Henkel Hysol EA 9396 paste epoxy adhesive used to fill in honeycomb core splices up to 0.25 inches in width. The 10 lb discrepancy was investigated and attributed to potential tolerances of the adhesives, core, and facesheet material, and error in the weigh scale. With tolerances and error combined, an estimated upper bound on the cylinder weight was 227.9 lb and was acceptably close to the measured weight.

Table 1. IML* facesheet layup in acreage and padup sections

CTA8.2B cylinder sections, measured from either FWD or AFT end, in inches	Stacking sequence, in degrees. Bold denotes a padup ply
20.0 to test article midlength (acreage)	[60/-60/0/0/-60/60]
18.0 to 20.0	[60/-60/**45**/0/0/-60/60]
14.5 to 18.0	[60/-60/**45**/0/0/-60/**-45**/60]
13.5 to 14.5	[60/-60/**45**/0/0/**45**/-60/**-45**/60]
0.0 to 13.5	[60/**-45**/-60/**45**/0/0/**45**/-60/**-45**/60]

*OML facesheet layup is symmetric with the IML facesheet.

2.2.2 Nondestructive Evaluation and Inspection

Prior to potting, nondestructive evaluation (NDE) was performed to inspect the test article by shearography [9] and structured-light scanning [10] techniques. From the NDE of the test article, a total of seven anomalies were detected and measured. The map of indication locations from shearography is shown in Figure 1, and the size and facesheet location of each anomaly is listed in Table 2. One indication was determined to be a delamination in one of the facesheets, but the other six were not able to be characterized with high-degrees of confidence. Because of the location and size of the indications, the SBKF team decided that the failure load sequence would be under combined compression and bending loading instead of pure axial compression in an effort to avoid any adverse influence of these NDE indications. Specifically, it was decided that the bending component of the load would be toward the 0° circumferential location to ensure no indications were in-line with the area of expected maximum compression and could therefore cause premature material failure prior to buckling.

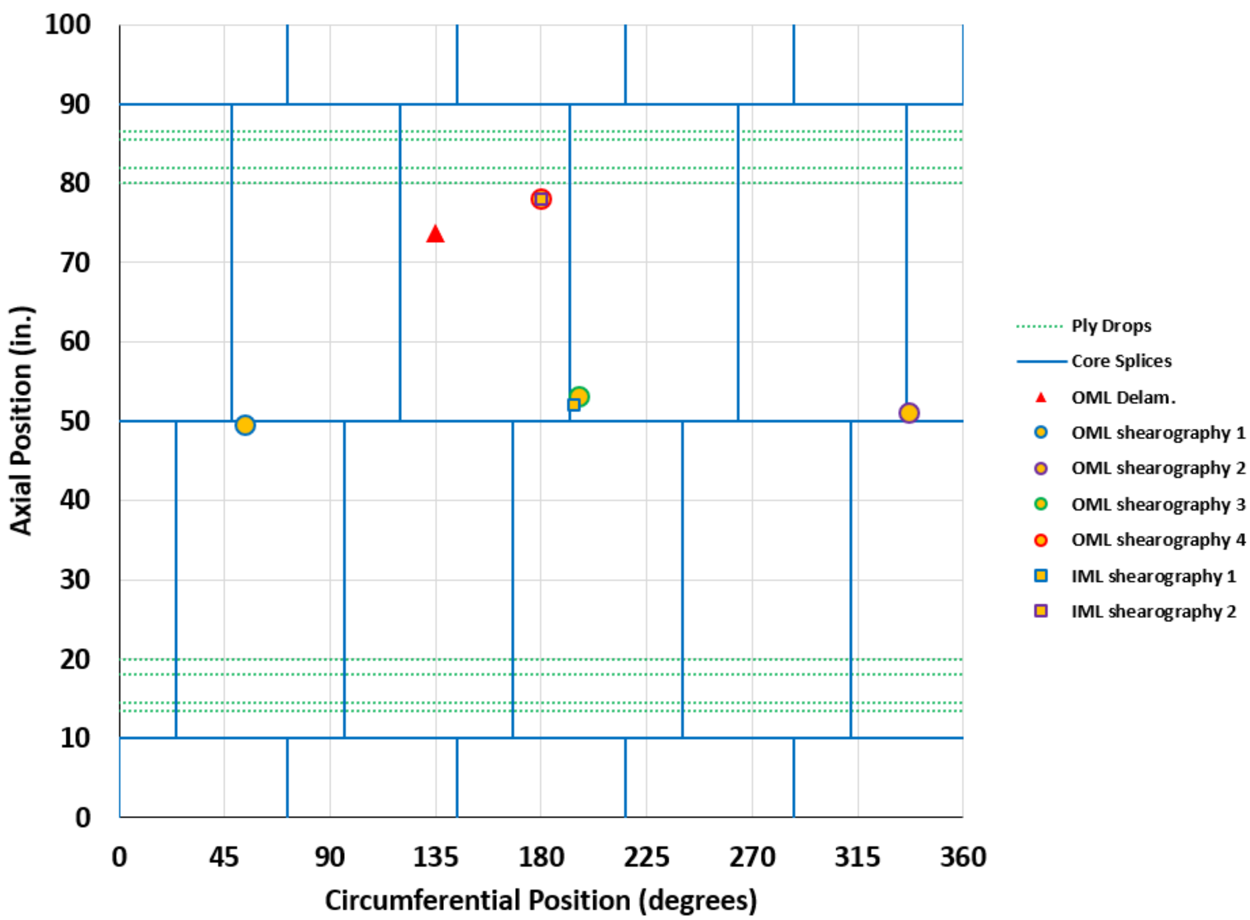

Figure 1. Map of shearography-based indications.

Table 2. Shearography-based indication description

Surface and Indication	Indicated Size (Height x Width), inches
OML delamination	0.60 x 0.30
OML shearography 1	0.50 x 0.25
OML shearography 2	0.50 x 0.50
OML shearography 3	1.00 x 1.00
OML shearography 4	0.75 x 0.25
IML shearography 1	1.00 x 0.50
IML shearography 2	0.50 x 0.25

2.2.3 As-manufactured State Prior to Installation

Structured light scans of test article OML and IML surfaces were performed, after the test article had been potted into pi-shaped aluminum attachment rings, to determine the geometric imperfections of the test article. By using a script written in Python specifically for this project, the structured light scans were able to be processed to return information about the test article midsurface radial position (midsurface defined herein as the mean radial position between the OML and IML surfaces) and the shell thickness (shell thickness defined herein as the difference between the OML and IML surfaces) at any location on the test article. The midsurface radial position and shell thickness data were later implemented into, and used in, the development of the *as-manufactured* finite element method (FEM) analysis models. The IML surface radial position contour is shown in Figure 2. The OML surface radial position contour is shown in Figure 3. The calculated midsurface radial position contour of the test article is shown in Figure 4. The shell thickness contour is shown in Figure 5. When interpreting Figure 4 and Figure 5, it is important to remember that both calculated contours account for the presence of the padup plies at the axial coordinates below -30.0 in. and above 30.0 in. The potted section within the aluminum attachment rings were truncated out of the contour images to highlight the distinct, but overall small magnitude, geometric variations.

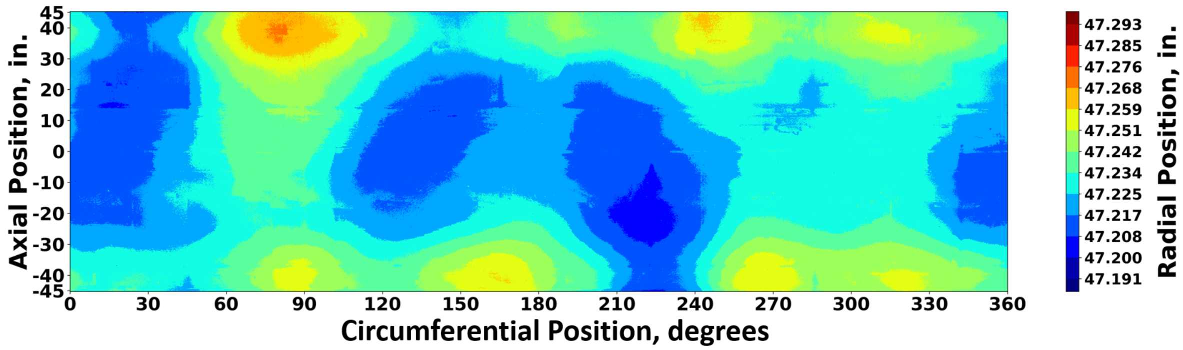

Figure 2. IML surface radial position for CTA8.2B.

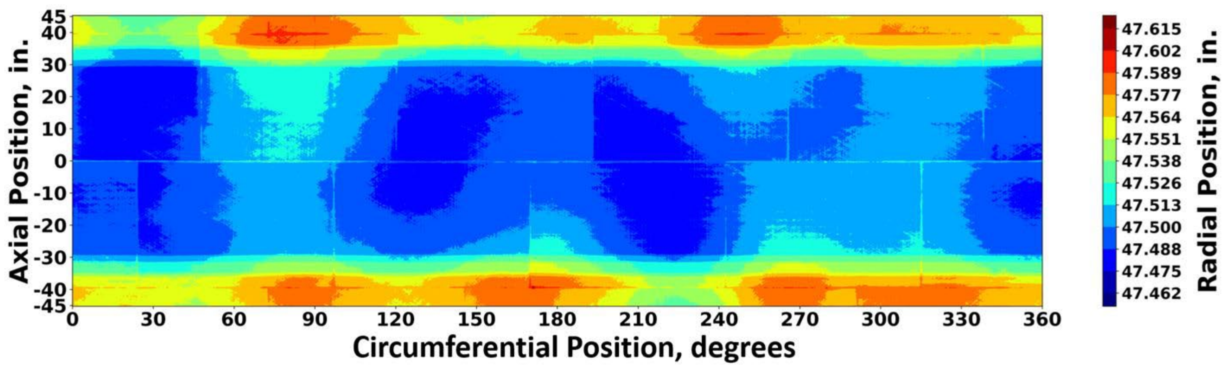

Figure 3. OML surface radial position for CTA8.2B.

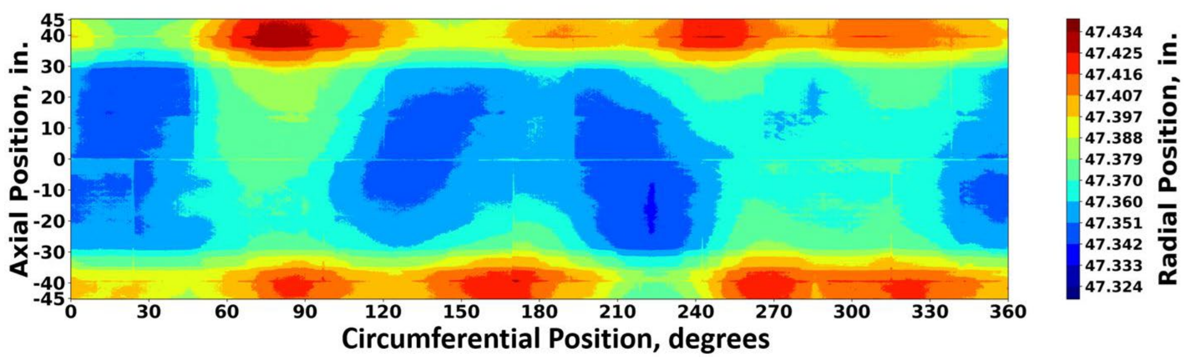

Figure 4. Calculated midsurface radial position for CTA8.2B.

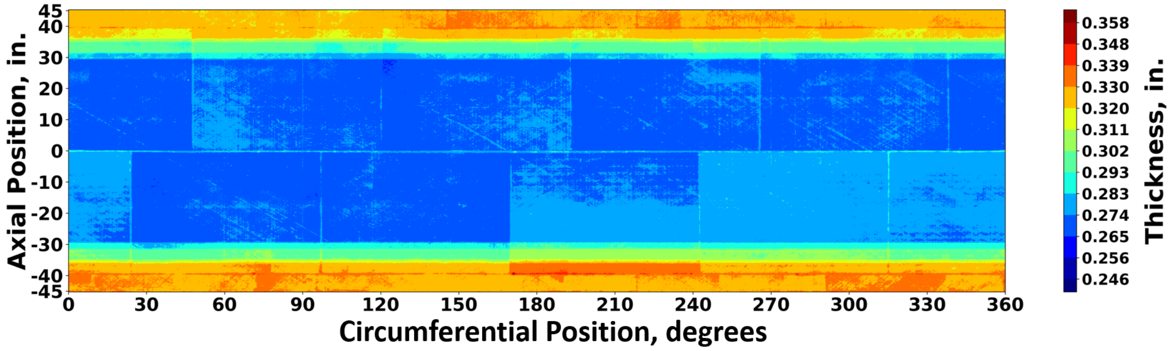

Figure 5. Calculated shell thickness for CTA8.2B.

The calculated midsurface position shown in Figure 4 exhibits an undulating pattern of multiple wavelengths around the circumference of the test article extending top to bottom. The calculated shell thickness in Figure 5 does not correlate to the calculated midsurface radial position and indicates that the combination of midsurface position and thickness were independent parameters to describe the geometry of a shell structure. The thicker sections of the test article resulting from the padups were clearly visible beyond the acreage section. Also, the core sheets and the core splices become noticeable within the acreage as the lighter blue horizontal and vertical lines on an irregular grid pattern.

2.3 Test Facility

Testing was conducted in the MSFC in building 4619-LTAE under the direction of the ET30 Structural Strength Test Group. The test assembly was designed, analytically verified, and fabricated to meet program test objectives. The test assembly was a self-reacting load system composed of an upper and lower load spider, 16 load struts, upper and lower transition sections, the test-article assembly, and eight load lines. Each load line consisted of a hydraulic cylinder, 4-in.-diameter loading rod (pipe), a load cell, and attachment hardware. The load lines were controlled independently in load control or stroke (displacement) control to apply uniform compression or combined compression and bending with a maximum load capability of 1.5 million pounds of axial compression force and 80,000 pounds of axial tension force. Provisions were made to remove any test-assembly dead weight from the test article prior to the beginning of each load sequence. The MSFC design drawings for each of the components that comprise the test assembly, and an overview of the test assembly itself, are indicated in Figure 6. For the testing described herein, the load lines accommodated a stroke of ±2.0 in. during testing.

2.4 Test Article Installation

CTA8.2B was oriented to a known, specific circumferential orientation for testing, as shown in Figure 7. Having a known orientation was important for these tests so that the structural response, including strains and displacements, could be fully compared to the predictions. Knowing the orientation was particularly important during tests that applied a bending moment because the maximum compression load introduced into the test article needed to occur in a specified location around the cylinder. It was also required that the top and bottom loading fixtures be aligned with each other so that the load lines were vertical and oriented parallel with the test article's longitudinal axis. Proper alignment of the load lines ensured that undesirable torsion or bending loads were negligible during testing. The load attachment rings were indexed with respect to the test article circumferential reference location to ensure proper alignment in the built-up test assembly, as specified in the assembly drawing (Figure 60 in the Appendix) and [7]. The attachment ring alignment, relative circumferential index angle, parallelism, and perpendicularity were verified and documented per the assembly procedure also in [7].

CTA8.2B interfaced with the test assembly via a set of attachment rings. The rings were one-piece 6061-T6 aluminum with a pi-shaped cross section that interfaced with the transition section (90M12372 in Figure 6) and in which the test article was seated. The attachment rings weighed approximately 358 lb each. CTA8.2B was placed in the groove, potted with Micor Micorox® Standard Grout [11] material, and mechanically fastened in place according to the assembly procedure described in the assembly drawing (Figure 60 in the Appendix) and [7]. The potting material was not considered a structural transfer mechanism between the test article and attachment rings in terms of loading because a release film composed of Loctite® Frekote 700-NC™ [12] was applied in the process of installing CTA8.2B in the attachment rings to make the bond weak and instead to rely on the test-article ends being in bearing contact at the "bottom" of the attachment ring grooves. The potting material, however, was considered part of the primary mechanism against the out-of-plane rotation of the test article. Furthermore, mechanical fasteners (bolts through both attachment ring flanges, the potting material, and the test article) were used as a handling and a failsafe feature.

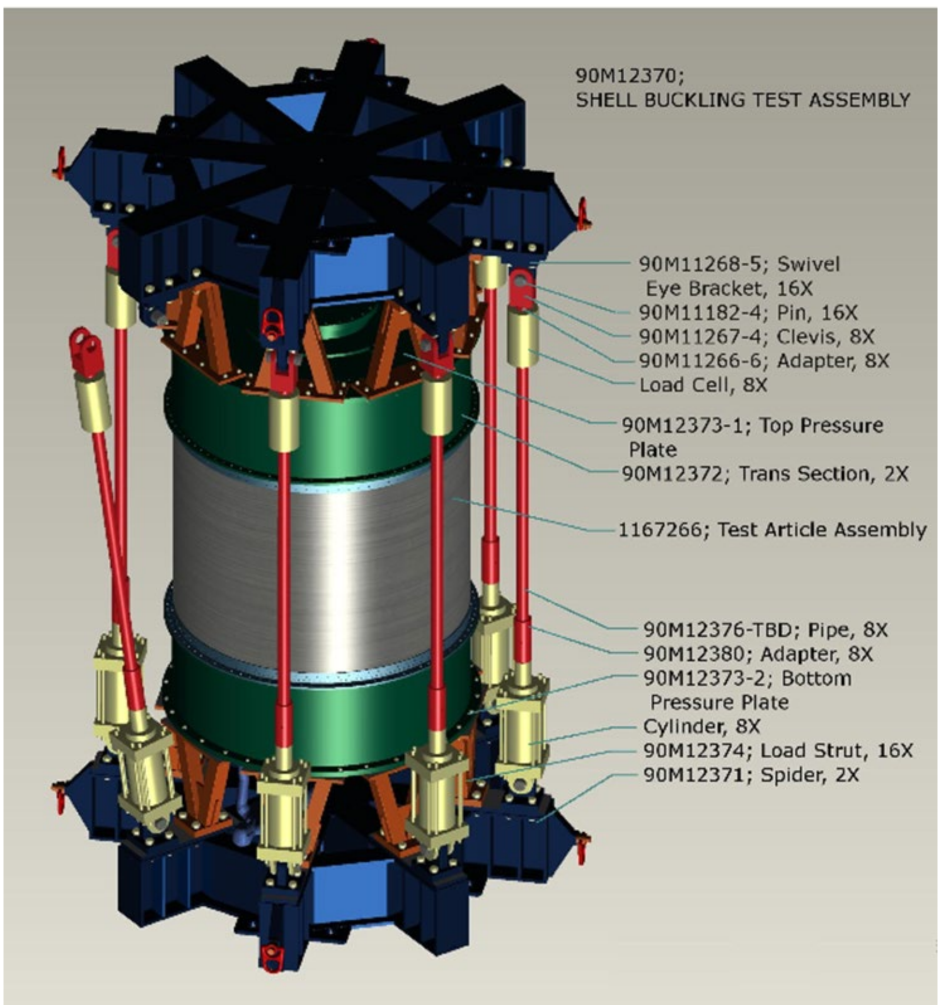

Figure 6. SBKF test assembly at MSFC, MSFC drawing #90M12370.

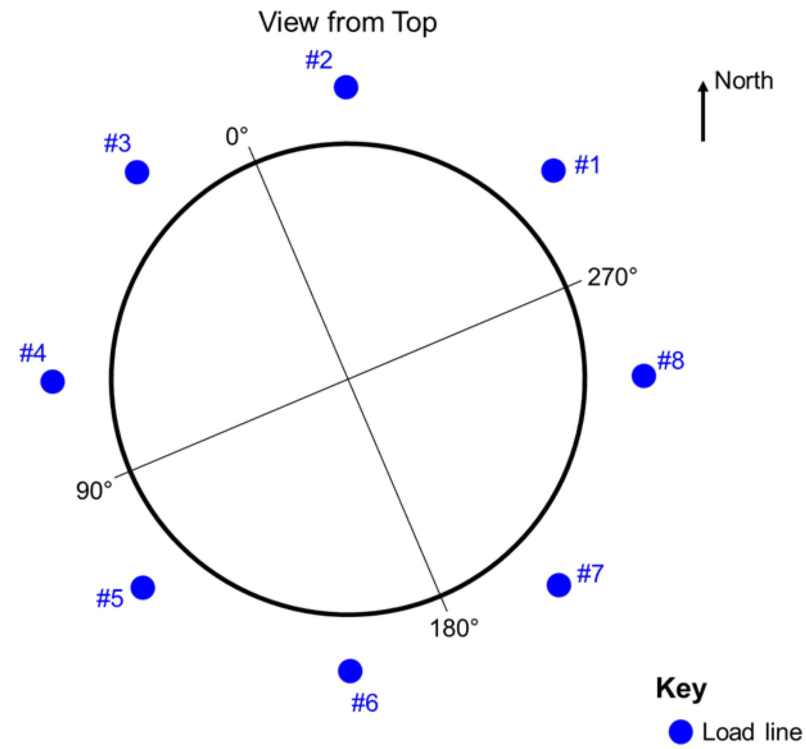

Figure 7. Test article orientation, load-line layout, and numbering convention, top view.

2.5 Test Article Instrumentation

Several types of instrumentation and photographic/video systems were utilized during the testing of CTA8.2B and included strain gages, displacement transducers, load cells, and low-speed digital image correlation (DIC) and high-speed digital image correlation (HS-DIC) techniques. In addition, digital photos and video were obtained during the setup, testing, and tear-down of the test article to document the test process. All measured data obtained during the test was synchronized with respect to time, load signal from load line #1, and a triangle wave signal to enable posttest data synchronization. All test systems, i.e. digital image correlation systems, MTS FlexTest60 control system, data acquisition system (DAS), and high-speed video systems were subjected to pretest checkout to verify proper operation, setup, and functionality.

2.5.1 Displacement Measurement

Axial, radial, and tangential displacement measurements of the test article and the test-article attachment rings were obtained during the test. Actuator displacements were measured using Temposonic displacement transducers attached to the hydraulic cylinders and were used as position control sensors for the MTS FlexTest60 control system. Additionally, the axial displacement of the AFT and FWD attachment rings were used to calculate the end-shortening of the test article (i.e. the relative axial motion of the FWD attachment ring with respect to the AFT attachment ring). As such, the axial displacement of both attachment rings was measured at four locations spaced 90° around the circumference. The measurement locations are shown in Table 3 and Figure 8, Figure 9, and Figure 10. Additionally, the axial displacement of the AFT ring was measured at one location on the OML attachment ring flange as shown in Table 3 and Figure 8,

Figure 9, and Figure 10; this additional OML measurement was used to calculate rotation (about the tangent) of the AFT attachment ring.

The axial end-shortening of the test article was calculated at four axial-measurement locations around the circumference (0°, 90°, 180°, and 270°) as follows:

$$0°:\ \delta_{D000A} = \delta_{D113A} - \delta_{D317A}$$

$$90°:\ \delta_{D090A} = \delta_{D114A} - \delta_{D318A}$$

$$180°:\ \delta_{D180A} = \delta_{D115A} - \delta_{D319A}$$

$$270°:\ \delta_{D270A} = \delta_{D116A} - \delta_{D320A}$$

where δ_{D113A}, δ_{D114A}, δ_{D115A}, δ_{D116A} and δ_{D317A}, δ_{D318A}, δ_{D319A}, δ_{D320A} correspond to electronic displacement indicator (EDI) measurements on the AFT and FWD attachment rings, respectively, and δ_{D000A}, δ_{D090A}, δ_{D180A}, δ_{D270A} correspond to the derived end-shortening displacements at the 0°, 90°, 180°, and 270° locations, respectively. These end-shortening displacement equations presume that the measured AFT and FWD displacements were negative downward. The measurement locations are shown in Table 3 and Figure 8, Figure 9, and Figure 10. The naming convention of the EDIs are associated with their function and position as presented in Figure 8. The average of the four axial EDI calculations are calculated to provide a global test article end-shortening measurement.

The radial displacement in the proximity of the predicted global buckling event origination were measured using four additional EDIs installed on the IML side of the cylinder, These EDIs designated D425R through D428R were installed as shown in Table 3, Figure 8 and Figure 9.

The out-of-plane deflections of the test article and attachment rings were measured at 13 locations. Specifically, displacements were measured at the midlength (see note in Table 3 for additional midlength location information) of the test article and on both attachment rings at four circumferential locations spaced 90° as shown in Table 3 and Figure 8, Figure 9, and Figure 10.

The relative rotational movement of the AFT and FWD attachment rings were monitored by measuring the tangential motion of both attachment rings at one circumferential location as shown in Table 3 and Figure 8, Figure 9, and Figure 11. These tangential displacement measurements were used to characterize the rotation of the rings about the cylinder axis (tangent to the edge of the attachment ring).

NOTE: All arrow markers in Figure 8, Figure 9, Figure 10, and Figure 11 indicate the direction of positive displacement associated with the displacement measurement. Sign conventions are also described in Table 3.

Table 3. EDI description

EDI ID+	Measurement range	Measurement description	Sign convention
D101R, D102R, D103R, D104R, D309R, D310R, D311R, D312R	±1.0 in.	Radial displacement on the AFT and FWD attachment rings to characterize local or rigid-body displacements	Outward radial displacement: +
D205R#, D206R#, D207R#, D208R#	±2.0 in.	Radial displacement at the midlength of the test article	Outward radial displacement: +
D113A*, D114A*, D115A*, D116A*	±1.0 in.	Axial displacement of the AFT attachment ring on the IML flange (for test-article end-shortening and ring-rotation calculations)	Upward axial displacement: +
D317A*, D318A*, D319A*, D320A*	±2.0 in.	Axial displacement of the FWD attachment ring on the IML flange (for test-article end-shortening calculation)	Upward axial displacement: +
D121T, D322T	±1.0 in.	Tangential displacement at a point on the AFT and FWD attachment rings to characterize relative torsional displacements	Displacement in positive theta: +
D123S	±1.0 in.	Radial displacement on the AFT and attachment ring to characterize ring clevis rotation or deformation	Outward radial displacement: +
D124O	±1.0 in.	Axial displacement of the AFT attachment ring on the OML flange (for test-article end-shortening and ring-rotation calculations)	Upward axial displacement: +
D425R, D426R, D427R, D428R	±1.0 in.	Radial displacement at selected locations associated with the global buckling onset	Outward radial displacement: +

#All midlength radial EDI’s were placed 0.5 in. down (in negative axial direction) and 0.4 in. to the negative degree (clockwise from top).

*All axial EDI’s were placed 0.4 in. to the positive degree (counterclockwise from top).

+Unless otherwise indicated, EDI’s were installed per SBKF-P3-CYL-CTA8.2B test plan[7].

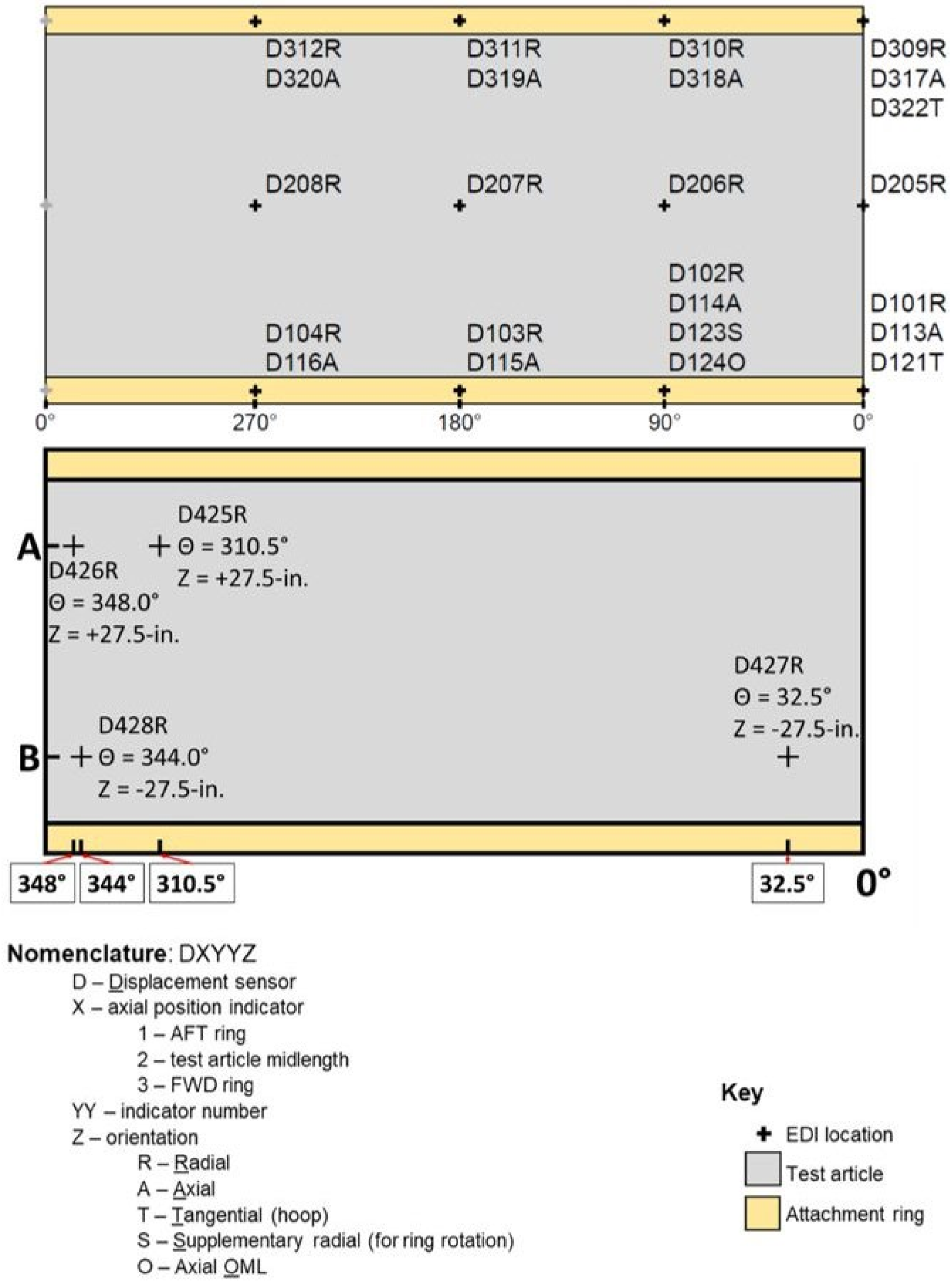

Figure 8. Locations of EDIs, viewed from IML.

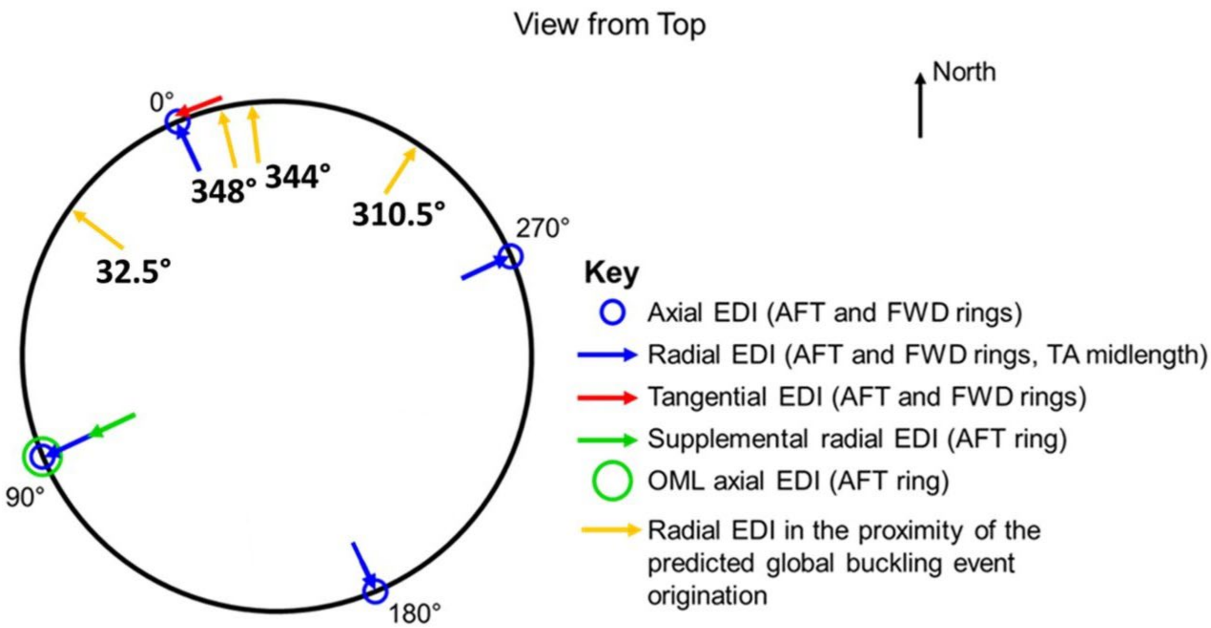

Figure 9. Locations of EDIs, viewed from above.

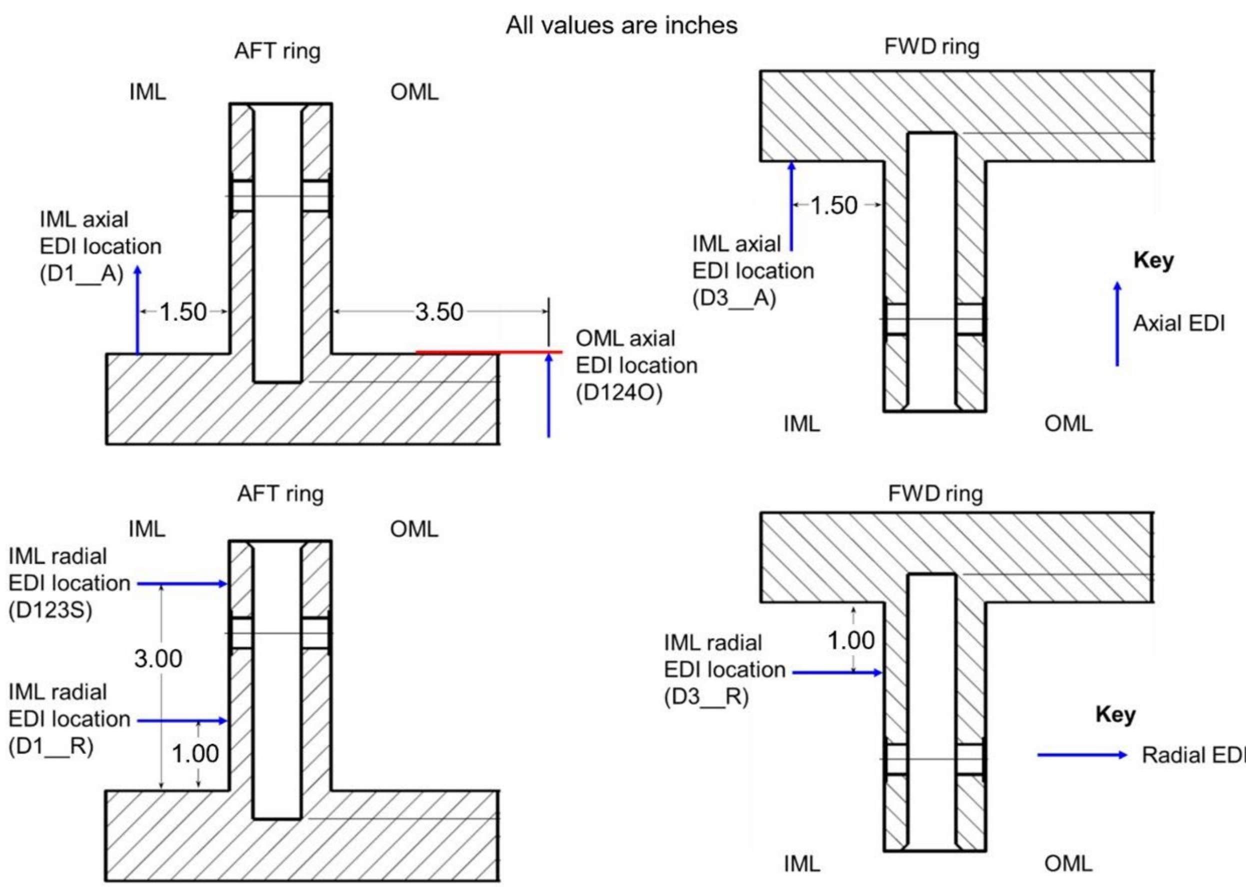

Figure 10. Axial and radial EDI locations on the attachment rings.

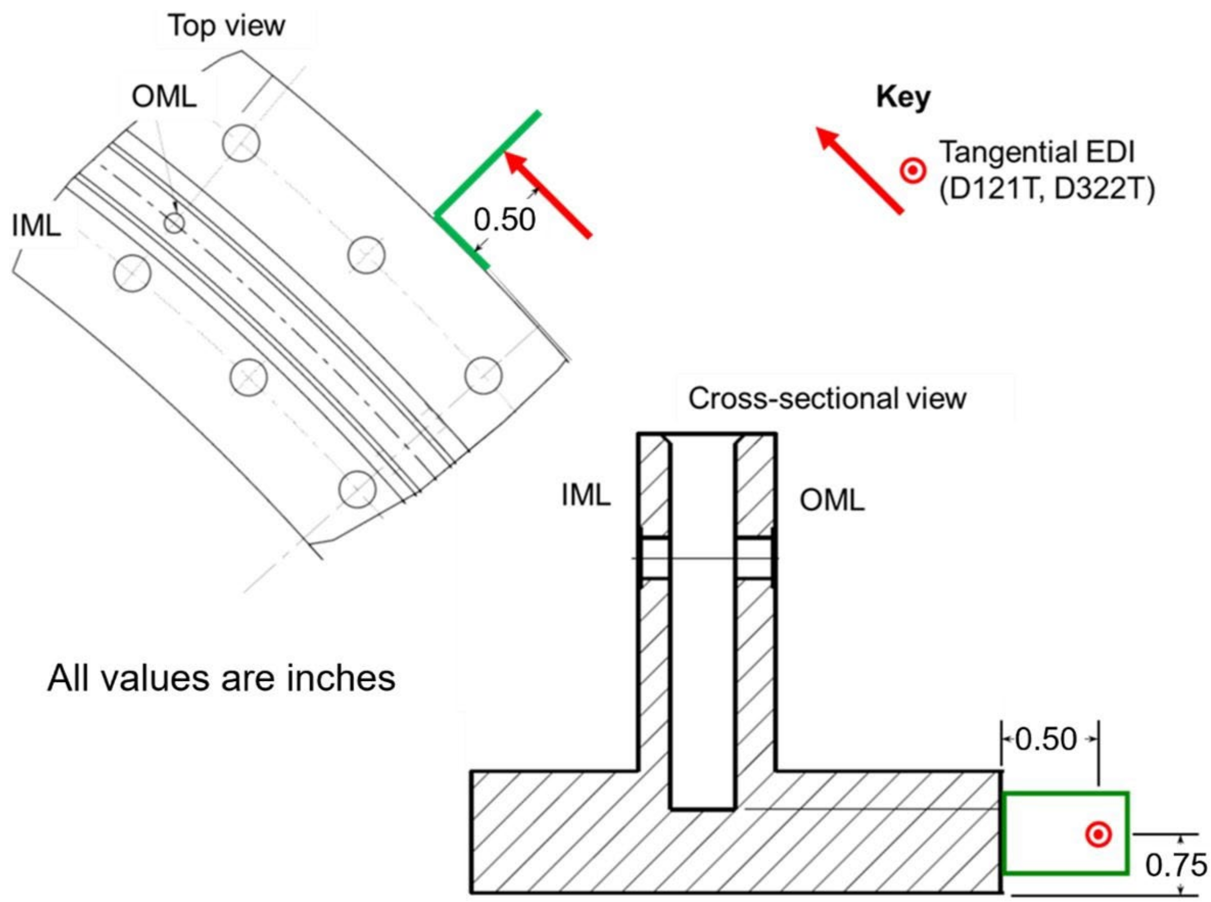

Figure 11. Tangential EDI locations on the attachment rings.

2.5.2 Strain Measurement

Strain measurements on the test article were required to assess uniformity of the load introduction into the shell during loading and monitor the local strain response of the test article during the prebuckling and postbuckling phases of testing. To this end, strain gage locations were chosen to measure strains in both acreage and padup areas. Two gage types were used: CEA-06-187UW-350 (uniaxial) and CEA-06-125UT-350 (biaxial). These gages had appropriate temperature and strain range for the expected loading and environmental conditions during the test. The gage patterns and labeling convention were specified in LaRC drawing 1286637 as specified in the instrumentation drawing (Figure 62 in the Appendix). Each gage was applied per manufacturer's recommendations for graphite-epoxy composite material and the MSFC Test Team standard installation procedures.

2.5.3 Three-Dimensional Digital Image Correlation

A photogrammetry technique, known as three-dimensional digital image correlation (3-D-DIC) was implemented during the test. The technique was used to track pixel subsets through a series of images, from the undeformed (or reference state) to deformed state, and allowed for surface shape, displacements, and strains to be calculated. 3-D-DIC utilized pairs of cameras in a stereo configuration to view and monitor the speckle pattern as it changed during loading and deformation. To facilitate the technique, the outer surface of the test article had applied a high contrasting speckle pattern of black speckles on a white background. The planform locations of the global 3-D low-speed camera systems, which were equally spaced around the circumference of the OML (centered approximately 45° apart), with an overlapping field-of-view in order to fully capture and characterize the behavior of the test-article are shown in Figure 12. Using such a high-contrasting speckle pattern, along with proper lighting, camera system calibrations, and camera parameters (e.g., sensor resolution direction, focus, lens aperture settings and depth-of-field, and relative angles (stereo angles) per system) the maximum resolution displacement and strain data was generated. All of the DIC systems were synchronized and the synchronization was verified and documented. The analog load signal from load line #1 and a triangle-wave synchronization signal were recorded for posttest correlation.

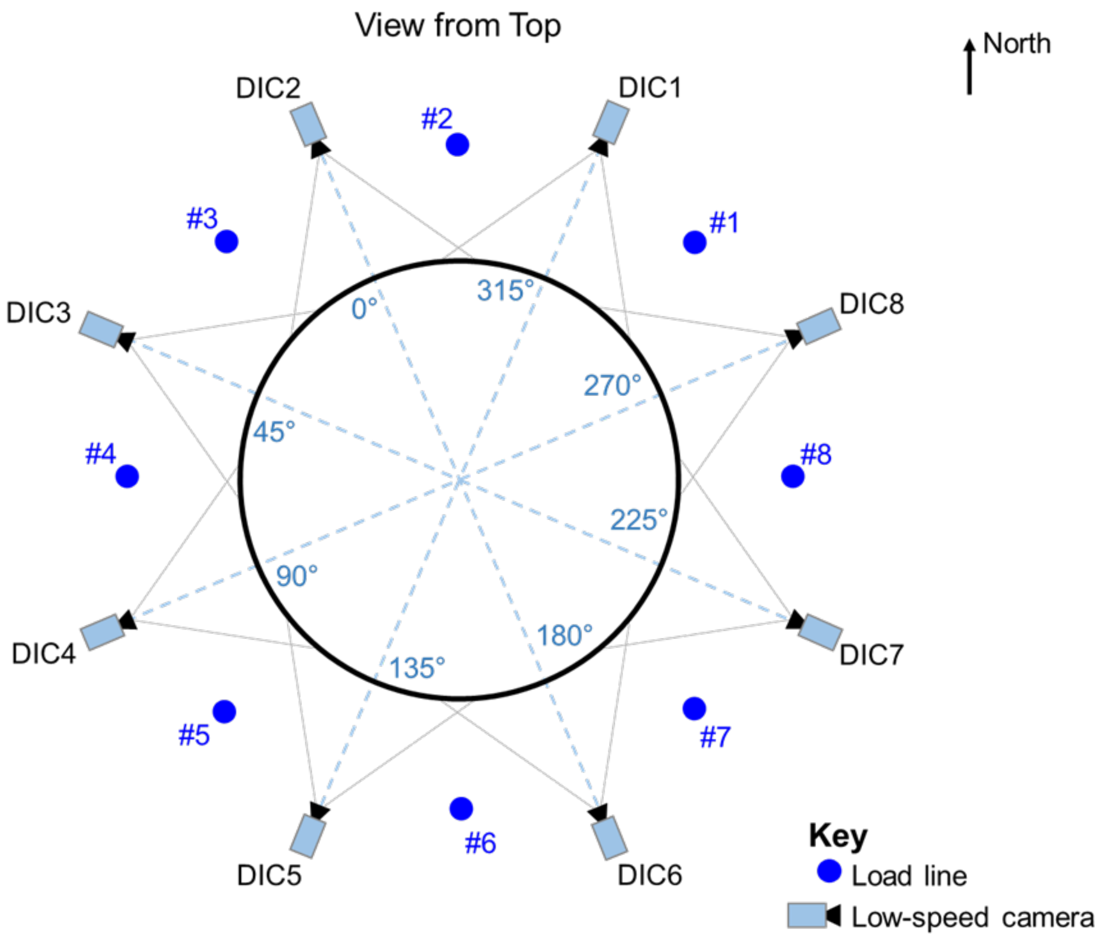

Figure 12. Eight low-speed DIC systems.

2.5.3.1 Low-Speed Digital Image Correlation (Global Systems)

A total of eight low-speed camera pairs were set up around the circumference of the OML, centered approximately 45° apart, for the global view of the test article. Each field-of-view was approximately 100 in. tall (including the test article acreage and the attachment rings) and 70° wide (allowing for 15° overlap between adjacent systems). Due to the resolution of the low-speed cameras and the field-of-view, a speckle size of 0.1-0.2 in. was ideal; however, due to the high-speed camera systems with the lower resolution, a speckle size of 0.3-0.5 in. was used on the test article (as discussed later) and a speckle size of 0.15-0.25 in. was used on the attachment rings.

2.5.3.2 Low-Speed Digital Image Correlation (Local Systems)

Based upon the NDE inspection, damage locations were detected, measured, and reported, as discussed in Section 2.2.2. Two of these locations were selected and marked as areas of interest for additional observation. These locations were centered at the 135° and 270° circumferential locations and 23.75-in. and 34.40-in. axial location above the midline, respectively, as shown in Figure 13. Therefore, two additional low-speed camera pairs were set up at these locations to monitor the behavior of the test article more closely at these locations. Due to the size of the damage areas, a much smaller field-of-view was required in order to maximize the resolution of the local systems. However, with a smaller field-of-view, a smaller speckle pattern was also required, and a technique was implemented in order to measure the local areas of interest without jeopardizing the correlation and accuracy of the global DIC systems. Combining system resolution requirements was achieved by using an optimized multiscale pattern via local greyscale variation [13], where the local pattern was embedded within the larger global pattern as shown in Figure 14. Use of a global-local speckle pattern allowed for the low-speed local DIC systems to be utilized alongside the low-speed and high-speed global DIC systems without correlation and accuracy interference. For local system 1 (135°) and local system 2 (270°), the field-of-view was approximately 26-in. tall (axial) and 26-in. wide (circumferential) with a speckle size of 0.04-0.06 in. or approximately 10 times smaller than the global speckle pattern size.

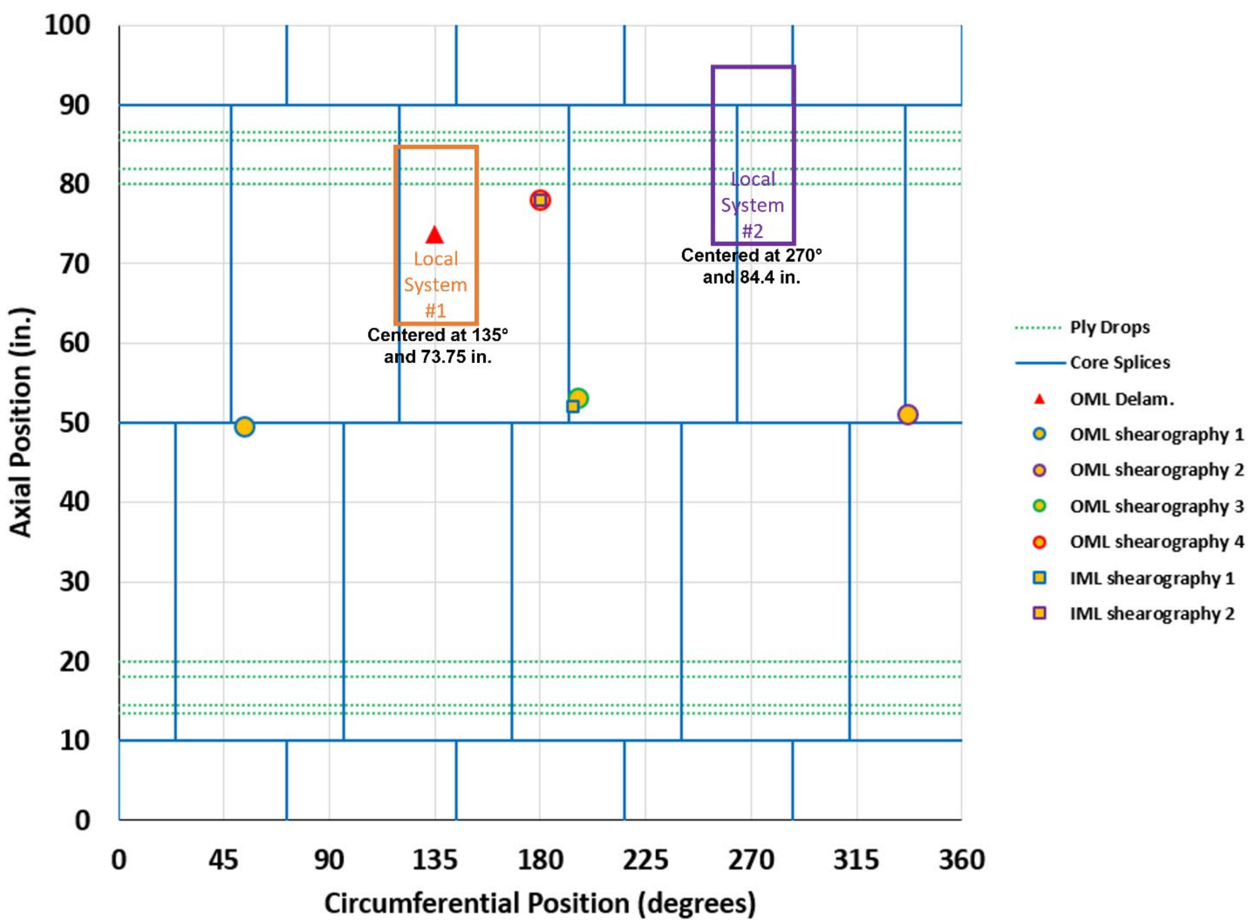

Figure 13. Local DIC system locations.

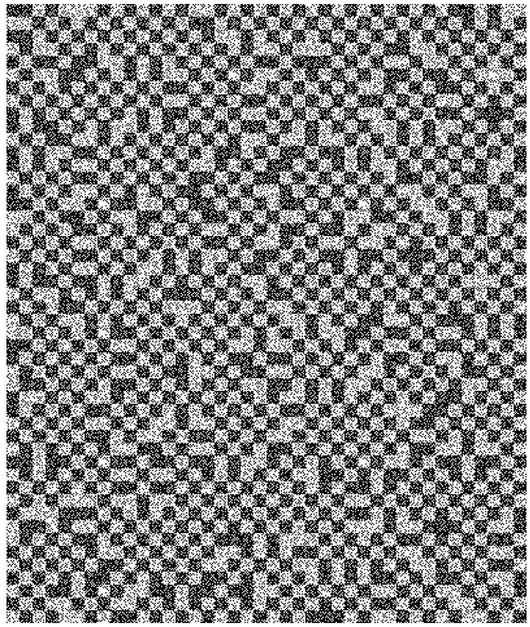

Figure 14. Optimized global-local DIC pattern.

2.5.3.3 High-Speed Digital Image Correlation

A total of six high-speed camera pairs were set-up around the circumference of the OML, as shown in Figure 15, to continuously record at 10,000 frames per second (fps). Due to the number of camera pairs and the test stand (camera mounting locations), the camera systems were not equally spaced. However, they were still located in a position to allow for overlapping coverage between adjacent camera systems. The high-speed camera systems were available to measure the buckling displacement response of the entire OML during all load sequences, but were primarily used during the failure load sequence to capture the dynamic failure event and damage initiation and propagation. Due to the high frame rate (10,000 fps) and the limited resolution of the cameras, the optimal speckle size was larger than that of the low-speed systems at 0.45 – 0.65 in. In order to properly correlate over the field-of-view and provide the best accuracy and data for all DIC systems (low-speed global and local), the speckle pattern of the global low-speed system was adjusted to be closer to the lower end of the optimal size for the global high-speed which was why a global speckle pattern of 0.3-0.5 in. was chosen for the entire acreage of the test article. The cameras were synchronized with respect to each other and had a common, manual, center-trigger recording function (i.e., 1.55 seconds of data from before the trigger and 1.0 seconds data after the trigger). The cameras were programmed to acquire images at a rate of 10,000 fps in a continuous write-overwrite loop, with a total recording time of approximately 2.55 seconds, to each camera's buffer until the high-speed DIC operator triggered the manual post-trigger recording after the buckling or failure event.

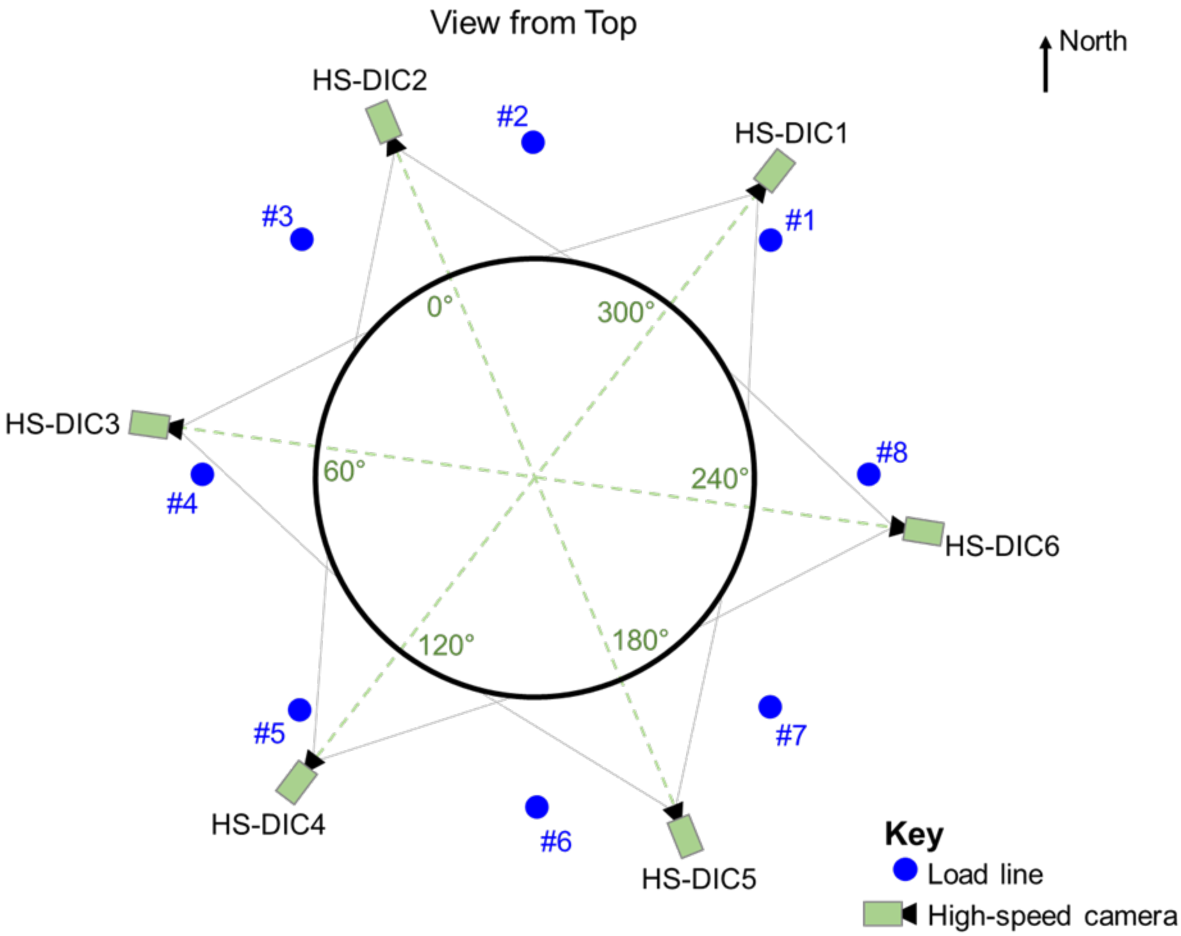

Figure 15. Six HS-DIC systems.

2.6 Test Load Sequences

A series of 12 load sequences (LS1 – LS12) were created for flexibility during the testing of CTA8.2B, but only a subset of these were ever planned to be selected. During testing, LS1-LS6, LS10, and LS12 were performed. Seven of the load sequences, LS1 – LS6 and LS10, were considered subcritical because the load levels applied to the test article were not expected to cause buckling or structural failure. The combined compression and bending load sequence to failure was identified as LS12. The predicted linear buckling load, P_{cr}, for the idealized, geometrically perfect test article with the attachment rings and nominal material properties subjected to a uniform axial compression load was 979,643 lbf and was obtained using an eigenanalysis (i.e. linear buckling analysis) within the general-purpose finite element software Abaqus[1] [14]. The predicted axial buckling load, P_{cr}^{NL}, from a geometrically nonlinear analyses of a FEM with as-manufactured measured radial and thickness imperfections and the entire test apparatus was predicted to be

[1] The use of a trademarks or names of a company are for accurate reporting and does not constitute an official endorsement, either expressed or implied, of such products or companies by the National Aeronautics and Space Administration.

836,900 lbf. For the purposes of this test, the critical bending moment, M_{cr}, was defined as the bending moment that will produce a maximum compressive line load that was the same as the uniform line load at P_{cr} for uniform axial compression. As such, M_{cr} was calculated to be 23.51×10^6 in-lbf. Each load sequence was defined in terms of a percentage of the critical axial compression load, P_{cr}, and percentage of critical bending moment, M_{cr}. The as-ran load sequences are described in the following sections. As will be discussed, the final critical load sequence, LS12, was combined loading for 90% axial compression and 10% bending in the 0° direction. The predicted linear buckling load for LS12, P_{cr}^{CL}, was 977,283 lbf, and the predicted nonlinear buckling load for LS12 using the FEM with the as-manufactured measured radial and thickness imperfections and the entire test apparatus was 761,600 lbf. The eight load sequences are described in the following sections.

Note: A positive load value corresponds to a tension load in the load line and results in a compression load in the test article. Also, each load sequence is started by ramping to the tare load (i.e., the actuator loads that remove the weight of the upper loading structure from the test article), the instrumentation is rezeroed at the tare load, and the loads in Table 4 - Table 11 are the loads measured from tare.

2.6.1 Load Sequence 1: 0.2 P_{cr} Axial Compression

A uniform axial compression load was applied to the test article to a maximum of 195,928 lbf total applied load (20% of P_{cr}) in the load steps specified in Table 4 and then unloaded to the tare load. A pause occurred at each load step to assess the behavior of the test article and test system. The purpose of this test was to exercise the test apparatus, remove slack from the system, check for uniformity of load application, and check the functionality of all control and measurements systems involved in the test. The control system loaded the test article in load control up to the designated total load with an average load rate of approximately 13,000 lbf/min based on the total load (an average load rate of approximately 1,600 lbf/min in each load line). Actuator loads of each step for LS1 are summarized in Table 4.

Table 4. Actuator loads (lbf) for LS1

Load Step	Actuator #1	Actuator #2	Actuator #3	Actuator #4	Actuator #5	Actuator #6	Actuator #7	Actuator #8	Total Load
#1	4,898	4,898	4,898	4,898	4,898	4,898	4,898	4,898	39,184
#2	9,796	9,796	9,796	9,796	9,796	9,796	9,796	9,796	78,368
#3	14,695	14,695	14,695	14,695	14,695	14,695	14,695	14,695	117,560
#4	19,593	19,593	19,593	19,593	19,593	19,593	19,593	19,593	156,744
#5	24,491	24,491	24,491	24,491	24,491	24,491	24,491	24,491	195,928

2.6.2 Load Sequence 2: 0.4 P_{cr} Axial Compression

A uniform axial compression load was applied to the test article in LS2. The load was increased to a maximum of 391,856 lbf compression (40% of P_{cr}) in the load steps specified in Table 5 and then unloaded to the tare load. A pause occurred at the end of each load step to assess the behavior of the test article and test system. The purpose of this test was to exercise the test system, and to verify that the applied loads and strains matched closely with the desired input loads and predicted strains and displacements. The control system loaded the test article in load control up to the designated total load with an average load rate of approximately 26,000 lbf/min based on the total load (an average load rate of approximately 3,300 lbf/min in each load line). Actuator loads of each step for LS2 are summarized in Table 5.

Table 5. Actuator loads (lbf) for LS2

Load Step	Actuator #1	Actuator #2	Actuator #3	Actuator #4	Actuator #5	Actuator #6	Actuator #7	Actuator #8	Total Load
#1	9,796	9,796	9,796	9,796	9,796	9,796	9,796	9,796	78,368
#2	19,593	19,593	19,593	19,593	19,593	19,593	19,593	19,593	156,744
#3	29,389	29,389	29,389	29,389	29,389	29,389	29,389	29,389	235,112
#4	39,186	39,186	39,186	39,186	39,186	39,186	39,186	39,186	313,488
#5	48,982	48,982	48,982	48,982	48,982	48,982	48,982	48,982	391,856

2.6.3 Load Sequence 3: 0.2 P_{cr} and 0.2 M_{cr}, Bending towards 0° Circumferential Position

A combined axial and bending load was applied to the test article in LS3. The load was increased to a total load of 195,928 lbf (total of all load line loads and 20% of P_{cr}) with maximum compression load occurring at the 0° circumferential location in the load steps specified in Table 6 and then unloaded to the tare load. A pause occurred at the end of each load step to assess the behavior of the test article and test system. The purpose of this test was to exercise the test system in the presence of combined axial compression and bending (bending in which maximum compression loads were applied to the test article between load lines 2 and 3), and to verify that the applied loads and strains matched closely the desired input loads and predicted strains and displacements. The control system loaded the test article in load control up to the designated total load with an average load rate of approximately 26,000 lbf/min based on the total load (an average load rate of approximately 3,300 lbf/min in each load line). Actuator loads of each step for LS3 are summarized in Table 6.

Table 6. Actuator loads (lbf) for LS3

Load Step	Actuator #1	Actuator #2	Actuator #3	Actuator #4	Actuator #5	Actuator #6	Actuator #7	Actuator #8	Total Load
#1	6,261	8,189	8,189	6,261	3,535	1,607	1,607	3,535	39,184
#2	12,523	16,379	16,379	12,523	7,070	3,214	3,214	7,070	78,372
#3	18,784	24,568	24,568	18,784	10,605	4,821	4,821	10,605	117,556
#4	25,046	32,758	32,758	25,046	14,140	6,428	6,428	14,140	156,744
#5	31,307	40,947	40,947	31,307	17,675	8,035	8,035	17,675	195,928

2.6.4 Load Sequence 4: 0.2 P_{cr} and 0.2 M_{cr}, Bending towards 90° Circumferential Position

A combined axial and bending load was applied to the test article in LS4. The load was kept the same as LS3 at a total load of 195,928 lbf (total of all load line loads and 20% of P_{cr}) with maximum compression load occurring at the 90° circumferential location in the load steps specified in Table 7 and then unloaded to the tare load. A pause occurred at the end of each load step to assess the behavior of the test article and test system. The purpose of this test was to exercise the test system in the presence of combined axial compression and bending (bending in which maximum compression loads were applied to the test article between load lines 4 and 5), and to verify that the applied loads and strains matched closely the desired input loads and predicted strains and displacements. The control system loaded the test article in load control up to the designated total load with an average load rate of approximately 26,000 lbf/min based on the total load (an average load rate of approximately 3,300 lbf/min in each load line). Actuator loads of each step for LS4 are summarized in Table 7.

Table 7. Actuator loads (lbf) for LS4

Load Step	Actuator #1	Actuator #2	Actuator #3	Actuator #4	Actuator #5	Actuator #6	Actuator #7	Actuator #8	Total Load
#1	1,607	3,535	6,261	8,189	8,189	6,261	3,535	1,607	39,184
#2	3,214	7,070	12,523	16,379	16,379	12,523	7,070	3,214	78,372
#3	4,821	10,605	18,784	24,568	24,568	18,784	10,605	4,821	117,556
#4	6,428	14,140	25,046	32,758	32,758	25,046	14,140	6,428	156,744
#5	8,035	17,675	31,307	40,947	40,947	31,307	17,675	8,035	195,928

2.6.5 Load Sequence 5: 0.2 P_{cr} and 0.2 M_{cr}, Bending towards 180° Circumferential Position

A combined axial and bending load was applied to the test article in LS5. The load the same as LS3 and LS4 at a total load of 195,928 lbf (total of all load line loads and 20% of P_{cr}) with maximum compression load occurring at the 180° circumferential location in the load steps specified in Table 8 and then unloaded to the tare load. A pause occurred at the end of each load step to assess the behavior of the test article and test system. The purpose of this test was to exercise the test system in the presence of combined axial compression and bending (bending in which maximum compression loads were applied to the test article between load lines 6 and 7), and to verify that the applied loads and strains matched closely the desired input loads and predicted strains and displacements. The control system loaded the test article in load control up to the designated total load with an average load rate of approximately 26,000 lbf/min based on the total load (an average load rate of approximately 3,300 lbf/min in each load line). Actuator loads of each step for LS5 are summarized in Table 8.

Table 8. Actuator loads (lbf) for LS5

Load Step	Actuator #1	Actuator #2	Actuator #3	Actuator #4	Actuator #5	Actuator #6	Actuator #7	Actuator #8	Total Load
#1	3,535	1,607	1,607	3,535	6,261	8,189	8,189	6,261	39,184
#2	7,070	3,214	3,214	7,070	12,523	16,379	16,379	12,523	78,372
#3	10,605	4,821	4,821	10,605	18,784	24,568	24,568	18,784	117,556
#4	14,140	6,428	6,428	14,140	25,046	32,758	32,758	25,046	156,744
#5	17,675	8,035	8,035	17,675	31,307	40,947	40,947	31,307	195,928

2.6.6 Load Sequence 6: 0.2 P_{cr} and 0.2 M_{cr}, Bending towards 270° Circumferential Position

A combined axial and bending load was applied to the test article in LS6. The load kept the same as LS3-LS5 at a total load of 195,928 lbf (total of all load line loads and 20% of P_{cr}) with maximum compression load occurring at the 270° circumferential location in the load steps specified in Table 9 and then unloaded to the tare load. A pause occurred at the end of each load step to assess the behavior of the test article and test system. The purpose of this test was to exercise the test system in the presence of combined axial compression and bending (bending in which maximum compression loads were applied to the test article between load lines 1 and 8), and to verify that the applied loads and strains matched closely the desired input loads and predicted strains and displacements. The control system loaded the test article in load control up to the designated total load with an average load rate of approximately 26,000 lbf/min based on the total load (an average load rate of approximately 3,300 lbf/min in each load line). Actuator loads of each step for LS6 are summarized in Table 9.

Table 9. Actuator loads (lbf) for LS6

Load Step	Actuator #1	Actuator #2	Actuator #3	Actuator #4	Actuator #5	Actuator #6	Actuator #7	Actuator #8	Total Load
#1	8,189	6,261	3,535	1,607	1,607	3,535	6,261	8,189	39,184
#2	16,379	12,523	7,070	3,214	3,214	7,070	12,523	16,379	78,372
#3	24,568	18,784	10,605	4,821	4,821	10,605	18,784	24,568	117,556
#4	32,758	25,046	14,140	6,428	6,428	14,140	25,046	32,758	156,744
#5	40,947	31,307	17,675	8,035	8,035	17,675	31,307	40,947	195,928

2.6.7 Load Sequence 10: 0.54 P_{cr} and 0.06 M_{cr}, Bending towards 0° Circumferential Position

A combined axial and bending load was applied to the test article in LS10. The load was increased to a total load of 529,008 lbf (total of all load line loads and 54% of P_{cr}) with maximum compression load occurring at the 0° circumferential location in the load steps specified in Table 10 and then unloaded to the tare load. A pause occurred at the end of each load step to assess the behavior of the test article and test system. The purpose of this test was to exercise the test system in the presence of combined axial compression and bending (bending in which maximum compression loads were applied to the test article between load lines 2 and 3), and to verify that the applied loads and strains matched closely the desired input loads and predicted strains and displacements. The control system loaded the test article in load control up to the designated total load with an average load rate of approximately 24,000 lbf/min based on the total load (an average load rate of approximately 3,000 lbf/min in each load line). Actuator loads for LS10 are summarized in Table 10.

Table 10. Actuator loads (lbf) for LS10

Load Step	Actuator #1	Actuator #2	Actuator #3	Actuator #4	Actuator #5	Actuator #6	Actuator #7	Actuator #8	Total Load
#1	11,362	11,844	11,844	11,362	10,680	10,198	10,198	10,680	88,168
#2	22,724	23,688	23,688	22,724	21,360	20,396	20,396	21,360	176,336
#3	34,086	35,532	35,532	34,086	32,041	30,595	30,595	32,041	264,508
#4	45,447	47,375	47,375	45,447	42,721	40,793	40,793	42,721	352,672
#5	56,809	59,219	59,219	56,809	53,401	50,991	50,991	53,401	440,840
#6	68,171	71,063	71,063	68,171	64,081	61,189	61,189	64,081	529,008

2.6.8 Load Sequence 12: 1.08 P_{cr} and 0.12 M_{cr}, Bending towards 0° Circumferential Position

A combined 90% of axial and 10% of bending load with maximum compression load occurring at the 0° circumferential location was applied to the test article in LS12 until failure of the test article occurred; the programmed load sequence is summarized in Table 11. A pause did occur at the end of each load step from step 1 to step 5 to assess the behavior of the test article and test system. No pause occurred after step 5. The control system loaded the test article in load control up to the buckling load with an average load rate of approximately 24,000 lbf/min based on the total load (an average load rate of approximately 3,000 lbf/min in each load line). After the failure event, the LCS initiated a system hold as described in [7], the DAS operator triggered the high-speed DAS, the HS-DIC operator triggered the high-speed camera recording, and the DIC operator documented the DIC image number associated with the buckling event. Actuator loads for LS12 are summarized in Table 11. Load levels identified in Table 11 as 70% and 100% of the predicted critical load (see footnotes 1 and 4) corresponded to the minimum and maximum expected buckling load during the test, respectively. Load steps 11 and 12 were programmed into the LCS in the circumstance the test article did not fail prior to application of load step 9.

Table 11. Actuator loads (lbf) for LS12

Load Step	Percent Critical Line Load	Actuator #1	Actuator #2	Actuator #3	Actuator #4	Actuator #5	Actuator #6	Actuator #7	Actuator #8	Total Load
#1	20%	22,724	23,688	23,688	22,724	21,360	20,396	20,396	21,360	176,336
#2	30%	34,086	35,531	35,531	34,086	32,041	30,595	30,595	32,041	264,506
#3	40%	45,447	47,375	47,375	45,447	42,721	40,793	40,793	42,721	352,672
#4	50%	56,809	59,219	59,219	56,809	53,401	50,991	50,991	53,401	440,840
#5	60%	68,171	71,063	71,063	68,171	64,081	61,189	61,189	64,081	529,008
#6	70%[1]	79,533	82,906	82,906	79,533	74,761	71,387	71,387	74,761	617,174
#7	80%[2]	90,895	94,750	94,750	90,895	85,441	81,585	81,585	85,441	705,342
#8	90%[3]	102,257	106,594	106,594	102,257	96,122	91,784	91,784	96,122	793,514
#9	100%[4]	113,618	118,438	118,438	113,618	106,802	101,982	101,982	106,802	881,680
#10	110%	124,980	130,281	130,281	124,980	117,482	112,180	112,180	117,482	969,846
#11	120%	136,342	142,125	142,125	136,342	128,162	122,378	122,378	128,162	1,058,014
	Facility max load	187,500	187,500	187,500	187,500	187,500	187,500	187,500	187,500	1,500,000

[1] 70% of predicted combined critical line loads, P_{cr}, and minimum expected buckling load

[2] 80% of predicted combined critical line loads, P_{cr}

[3] 90% of predicted combined critical line loads, P_{cr}

[4] 100% of predicted combined critical line loads, P_{cr}, and maximum expected buckling load

3.0 Analysis Description

Prior to the construction of CTA8.2B, multiple failure modes were assessed using analytical and numerical techniques to provide confidence that the test article would fail in global buckling prior to other strength-based failure or local buckling failure modes. The two pretest analyses and predictions are summarized in this section. The closed form solutions to check for material failure such as face sheet wrinkling, facesheet dimpling, and core shear crimping are mentioned in 3.1. Results from an axisymmetric modeling effort, which was used to assess the face sheet and core stresses in the area near the attachment ring are mentioned in 3.2. Lastly, the predicted prebuckling and postbuckling response of a FEM with shell elements with and without imperfections, also known as the global model, is presented in 3.3.

3.1 Closed-Form Analysis

Various closed-form analyses were conducted during the design of CTA8.2B. Closed-form solutions were used to calculate various sandwich cylinder failure modes including the linear global buckling, shear crimping, facesheet wrinkling, and facesheet dimpling loads, and maximum facesheet strain. A primary advantage of the closed-form analyses was the ability to quickly assess feasibility of numerous designs. Some closed-form analysis is also able to investigate metrics that were difficult to determine via finite element analysis (FEA) such as facesheet wrinkling and dimpling – two modes that are difficult to determine with a global FEA. Formulation, results, and discussion of the closed-form analyses pertaining to CTA8.2B are provided in [15] and are not duplicated in this report.

Closed-form analyses, however, do have certain limitations. Often the nominal geometries must be used and therefore all effects of geometric imperfections ignored. Geometric imperfections have repeatedly been shown to be influential in accurately predicting the compressive response of thin cylindrical shells. Idealized structures and boundary conditions are often required to be used in closed-form analysis and therefore are ineffective when investigating structures with discrete ply drops or tailor-made load introduction fixtures such as the aluminum attachment rings used for testing CTA8.2B.

3.2 Axisymmetric Finite Element Analysis and Ply-drop Testing Campaign

Numerous axisymmetric FEA models were created to investigate various stresses at otherwise difficult to analyze discontinuities such as core splices and facesheet padup ply drops in addition to boundary conditions during the design of CTA8.2B. Axisymmetric analyses indicated the potential for stress concentrations around the regions of the ply drops. To demonstrate the stress concentrations were a numerical artifact and not physical (as was believed), an experimental ply drop study was performed. To perform this study, coupon-sized specimens with ply drops were manufactured and axially loaded in compression until failure. The ply drop test campaign resulted in the conclusion that the stress concentrations associated with ply drops were not as severe as numerically indicated because the test specimens were able to sustain a compressive load up to and beyond the loads associated with material failure. Further details of the ply drop test campaign specimens are provided in Figure 63 and Figure 64 (in the Appendix). Modeling details, analysis results, and discussion of the axisymmetric analysis effort pertaining to CTA8.2B are provided in [15] and are not duplicated in this report. Axisymmetric models have the advantage of being able to capture finer geometric details in the models than closed-form or certain FEA shell-based analyses. Axisymmetric analyses were limited by the inability to include as-manufactured geometric imperfection data.

3.3 Global Finite Element Analysis

A FEM consisting of the test article, load introduction attachment rings, loading structure, and load lines was developed to predict the pre- and postbuckling response of CTA8.2B. This model is referred to as the global FEM. Four-noded, reduced-integration Abaqus S4R [16] shell elements were used for all of the test article and load introduction attachment rings, with other beam (B31), and truss (T3D2) elements for the rest of the test structure as shown in Figure 16. Element size for test article was 0.5-in. in the axial direction by 0.5° (or approximately 0.41-in.) in the circumferential direction and resulted in approximately 154,000 elements and 932,000 degrees of freedom (DoF) following guidance and method from [17]. The bottom nodes of the test fixture struts (i.e. beam elements) were kinematically constrained to a single central reference node. The reference node was fixed resulting in an effective simulation of the fixed bottom boundary conditions of the test. Load lines, modeled as truss elements, were kinematically attached to the top loading structure. Loads were applied to the bottom of the load lines for each of the load sequences. Such loading resulted in tensile loads in the load lines transmitted through the upper loading structure and resulted in compressive loads being imparted on the test article. Two types of models were developed; FEMs with perfect geometry and FEMs with radial midsurface and shell thickness geometric imperfections measured from structured light scans.

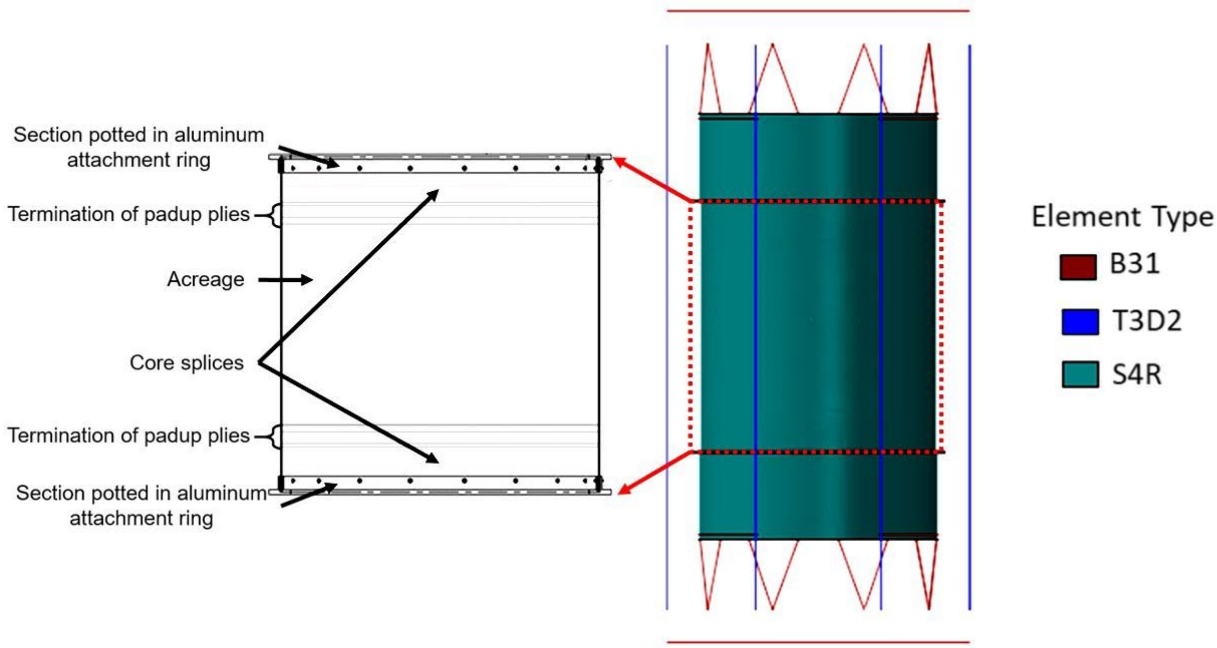

Figure 16. Finite element model sections of CTA8.2B.

Multiple analyses were completed to understand the prebuckling, buckling, and postbuckling behavior of CTA8.2B. First, a linear bifurcation buckling analysis was performed on the FEM with perfect geometry to obtain the perfect linear buckling load, P_{cr}. Second, a nonlinear buckling analysis was performed on the FEM with the perfect mesh (no radial or thickness imperfections) utilizing a general static solver preload step followed by a transient dynamic step to capture buckling and postbuckling response. Finally, the nonlinear analysis was repeated by perturbing the mesh in a stress-free manner to incorporate the CTA8.2B as-manufactured measured imperfections. In addition to the peak load, radial and axial displacements, the predicted axial and hoop strains on the OML and IML facesheet were investigated.

4.0 Analysis Results and Comparison with Experimental Observation

Multiple analyses were conducted pre- and posttest to gain an understanding of how the test article responded under various loading conditions. Additionally, CTA8.2B was the first composite test article in the SBKF program to differentiate between the as-manufactured imperfections calculated from the structured light scans and the as-installed imperfections calculated in part by updating the midsurface radial position prior to testing to failure using DIC-based data to calculate how the test article changed shape after installation into the test stand.

Thin-shell cylindrical structures are sensitive to many types of imperfections. For the composite portion of the SBKF, geometric-based imperfections of the midsurface and shell thickness variation have been the primary focus when correlating test and analysis results. The geometry of CTA8.2B was measured using the structured light scanning technique to produce data about the OML and IML surfaces. A description of how structured light data was produced, processed, and implemented into finite element models for the as-manufactured imperfections is given in [18]. Prior to testing CTA8.2B, however, it was observed that there were measurable changes to the position of the OML surface of previous test articles (CTA8.2 and CTA8.3) after they had been installed into the test stand. Such changes in shape were, at that time, unaccounted for in the modeling effort for pretest predictions and were only implemented posttest. Therefore, DIC was used to measure the OML surface geometry of CTA8.2B once installed in the test stand, but before testing started so that the *as-installed* geometry could be processed and implemented into the analyses. The analyses with these as-installed imperfections provided a second set of pretest predictions to use and compare with the experimental response of the test article.

An overview of the pretest FEM analysis using the as-manufactured geometry of CTA8.2B is provided first in the following subsection. Next, an overview of the pretest FEM analysis using the as-installed geometry of CTA8.2B is presented and compared with the experimental results. Since the pretest predictions using the as-installed geometry were closer to experimental observations, test-analysis correlation discussion will be limited to the failure sequence (LS12) and the analysis model using the as-installed geometric imperfections.

4.1 Global Finite Element Model with As-Manufactured Imperfections

As-manufactured geometric imperfections were collected via the structured light scanning technique. CTA8.2B was scanned after the test article had been secured within both aluminum attachment rings but before installation into the test structure. Structured light scan data of both the IML and OML surfaces were available so both radial midsurface position and shell thickness imperfections were calculated. An SBKF-developed codePy_TIGIRS [18] was used to modify a perfect-geometry model by implementing the calculated radial midsurface position and shell thickness imperfections into a FEM analysis model of CTA8.2B [18]. The results of implementing the radial midsurface position and shell thickness as-manufactured imperfections into an FEM analysis are shown in Figure 17 and Figure 18, respectively. These figures were generated by extracting shell-section, element, and node information from an Abaqus analysis results file so the features in the figures were representative of what was in the analysis model. The calculated midsurface radial position and shell thickness contours, in Figure 4 and Figure 5, respectively, are in good agreement with the contours of the as-manufactured FEM. The range of the midsurface radial position contours are 47.324 – 47.434 in. and 47.341 – 47.425 in. for the calculated and as-manufactured FEM, respectively. The range of the shell thickness contours are 0.246 – 0.358 in. and 0.264 – 0.336 in. for the calculated and as-manufactured FEM, respectively. The extreme positive and negative axial positions in the as-manufactured FEM contours contain the region of the model that includes the load introduction attachment rings and consequently return a thickness contour exceeding that of the provided range of values. In both the midsurface radial position and shell thickness contours, the as-manufactured FEM contours exhibit slightly reduced range compared to the calculated contours. In the midsurface radial position contours, for example, the smallest as-manufactured FEM contour is approximately 0.02-in. larger than the smallest contour in the calculated contour. The largest as-manufactured FEM contour is approximately 0.01-in. smaller than the largest contour in the calculated contour. Similar patterns occur for the shell thickness contours, but the magnitude is on the order of 0.02-in. for both the smallest and largest contours. The slight reduction in contour range extrema for the as-manufactured FEM contours is attributed to the averaging of point values during the implementation of the as-manufactured imperfections into the FEM. Additional details of how the as-manufactured imperfections were implemented into the CTA8.2B FEM are provided in [18].

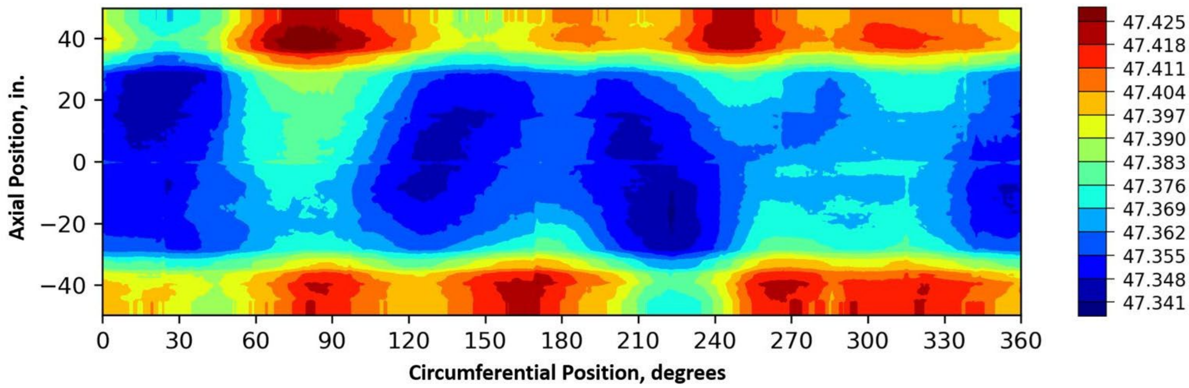

Figure 17. FEM as-manufactured radial midsurface position contour.

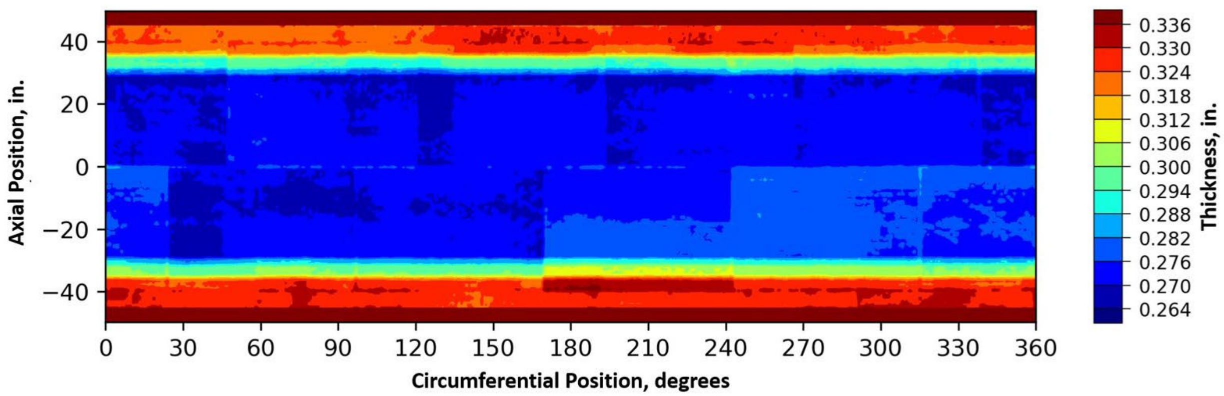

Figure 18. FEM as-manufactured shell thickness contour.

When subjected to the loading conditions of 90% axial compression combined with 10% bending over the 0° circumferential position for LS12, buckling initiation was predicted to occur at 761.6 kips with an initial radial inward buckle near the 27.5-in. axial and 348° circumferential location. Contours of predicted axial and radial displacements and axial and hoop strains at the buckling initiation load are shown in Figure 19, Figure 20, Figure 21, and Figure 22, respectively.

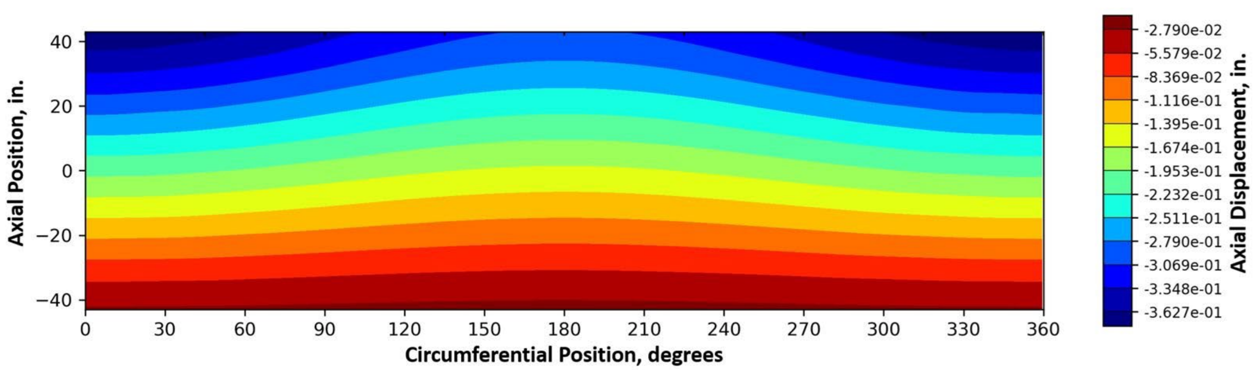

Figure 19. FEM as-manufactured axial displacement contour at buckling initiation.

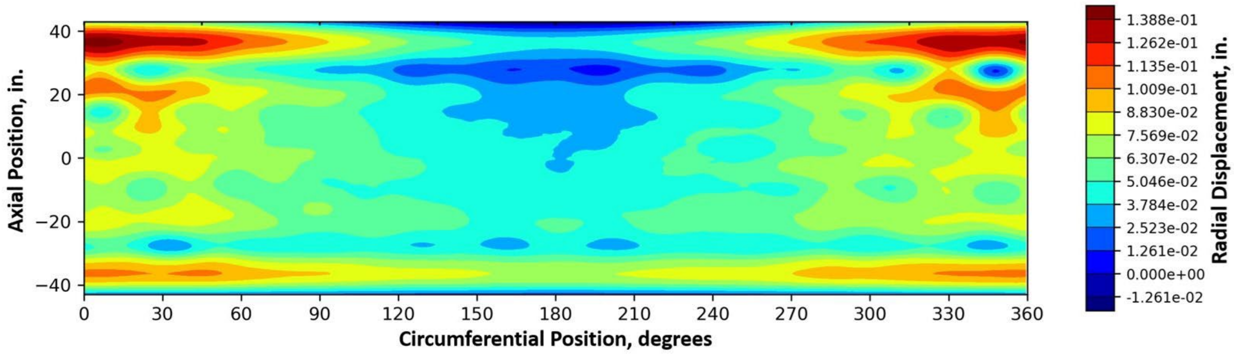

Figure 20. FEM as-manufactured radial displacement contour at buckling initiation.

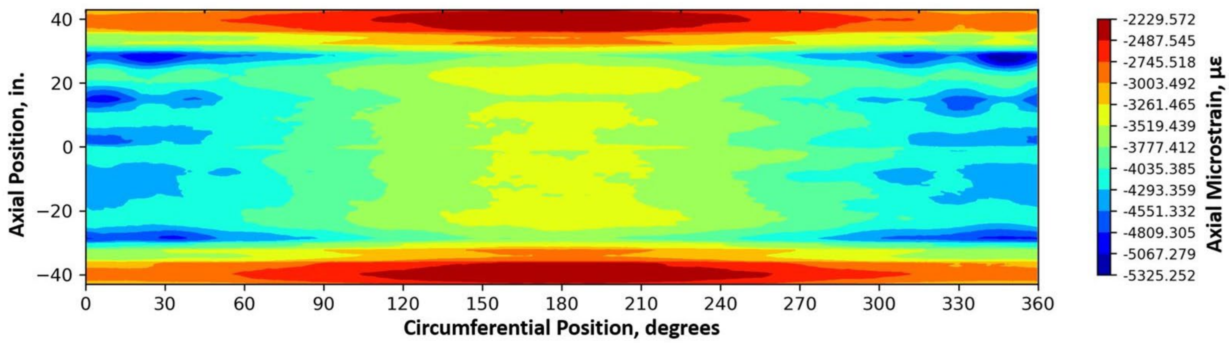

Figure 21. FEM as-manufactured axial strain contour at buckling initiation.

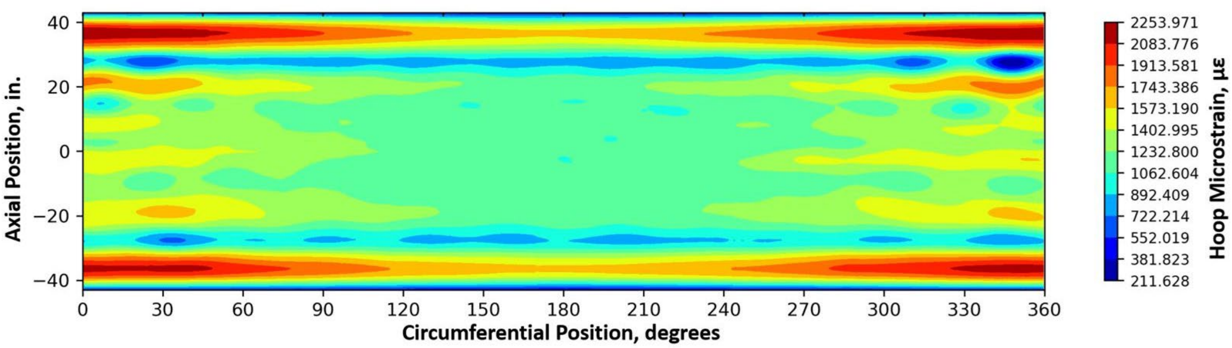

Figure 22. FEM as-manufactured hoop strain contour at buckling initiation.

The local dimples with the most-radially inward displacement observed in the experiment correlated well to the regions in the analysis that exhibited large inward radial displacement growth at buckling initiation. The experimental maximum load was 704.88 kips with an observed buckling initiation location near 27.5-in. axial and 331° circumferential location. The test article failed at 92.6% of the predicted maximum load (and 72.1% of the linear buckling combined load) and approximately 17° (approximately 13.6 inches) away from the predicted primary buckling initiation location when the as-manufactured imperfections were used in the analysis. Since the analysis using the updated as-installed geometry was also generated for the pretest predictions and this updated analysis resulted in closer agreement with the observed experimental response of the test article, further comparisons between the test and analysis are provided in that analysis section.

4.2 Global Finite Element Model with As-Installed Imperfections

The FEM with the as-installed geometry used the updated as-installed radial midsurface position rather than the as-manufactured radial midsurface position. To update the radial midsurface position, a set of DIC images were first collected after the test article was installed into the test structure. The DIC images were processed to generate a dataset representing the OML surface of the test article. The OML-surface DIC-based data was used to update the radial midsurface position in the model by altering the radial position such that, when combined with shell half-thickness, the new position would be equal to the DIC-based OML surface position. One assumption in this method was that the local thicknesses of the test article did not change from the time the as-manufactured data were collected to when the as-installed data were collected. The test structure, mesh, elements, material properties, analysis steps, etc. were kept identical to the analysis model with the as-manufactured imperfections.

To demonstrate the effects of the small changes in geometry from the as-manufactured imperfections (calculated from the structured light data) to the as-installed imperfections (calculated by updating the shell midsurface radial position via DIC-based data), the predicted load-displacement responses from various analyses of CTA8.2B are shown in Figure 23. Specifically, the presented results are from a geometrically perfect eigenanalysis with axial compression perturbation loading, a geometrically perfect nonlinear analysis with axial compression loading, nonlinear analyses with axial compression loading with as-manufactured and as-installed imperfections, and nonlinear analyses with combined 90% axial and 10% bending loading with as-manufactured and as-installed imperfections. The load sequence of pure axial compression to failure (LS8) was not experimentally performed, but these results are included in the figure to serve as reference to the predictions for the perfect geometry case. For the case of pure axial compression, the predicted buckling load for the perfect case (dashed red line) and pure axial compression was 979.6 kips, the predicted buckling load for the perfect case with combined loading was 977.3 kips, and the predicted buckling loads for the models with as-manufactured (solid blue line) and as-installed (dashed blue line) geometric imperfections were 836.9 kips and 812.5 kips, respectively. These predicted loads were 85.4% and 82.9% of the perfect load case, respectively. The predicted responses for the LS12 load case of combined 90% axial compression and 10% bending are shown by the solid green line and dashed green line, respectively. In this figure and in subsequent combined-loading cases, the vertical axis is the total load (the sum of the load applied by the load line). The predicted buckling load for LS12 was 761.6 kips with the as-manufactured imperfection and 751.3 kips with the as-installed imperfection. Therefore, the predicted buckling loads for the model with the as-installed imperfection were lower than those models with the as-manufactured imperfection by 2.9% for the pure axial compression case and by 1.4% for the combined loading case of LS12.

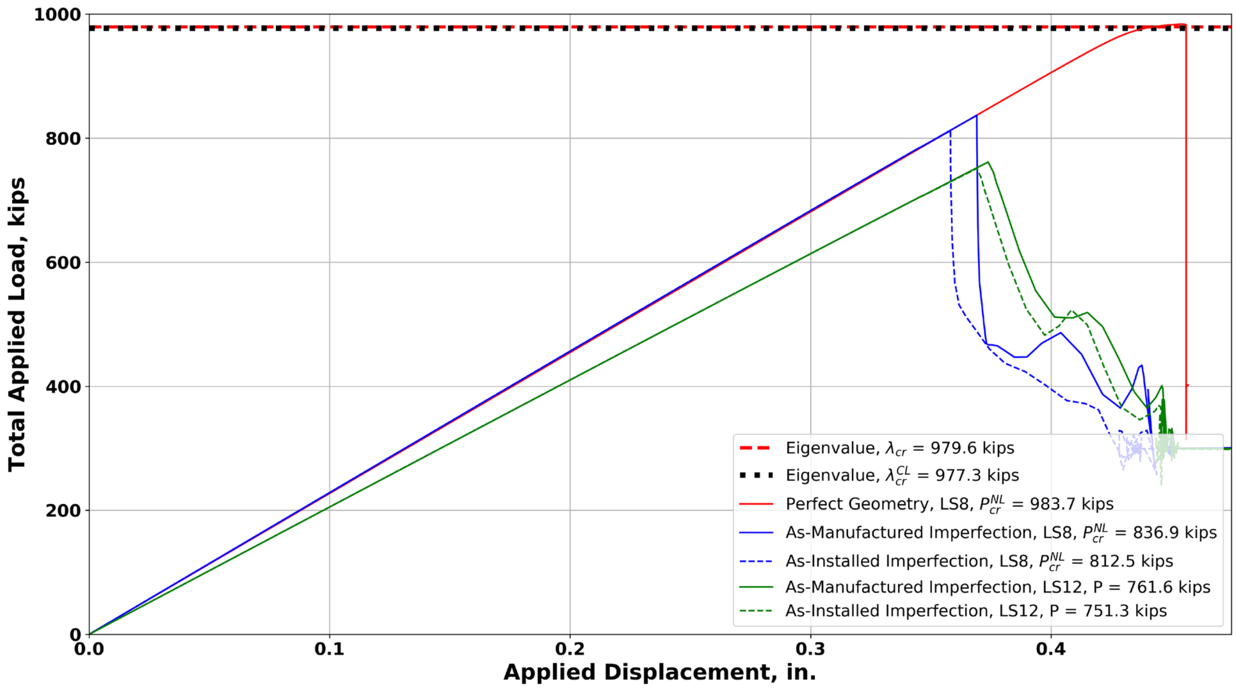

Figure 23. Comparison of responses with differing geometry and loading for CTA8.2B finite element analyses.

The midsurface radial position contour plot for the updated FEM with the as-installed imperfection is shown in Figure 24. Since the shell thickness was assumed to remain constant between the two models, the shell thickness contour is the same as shown previously for the as-manufactured analysis in Figure 18.

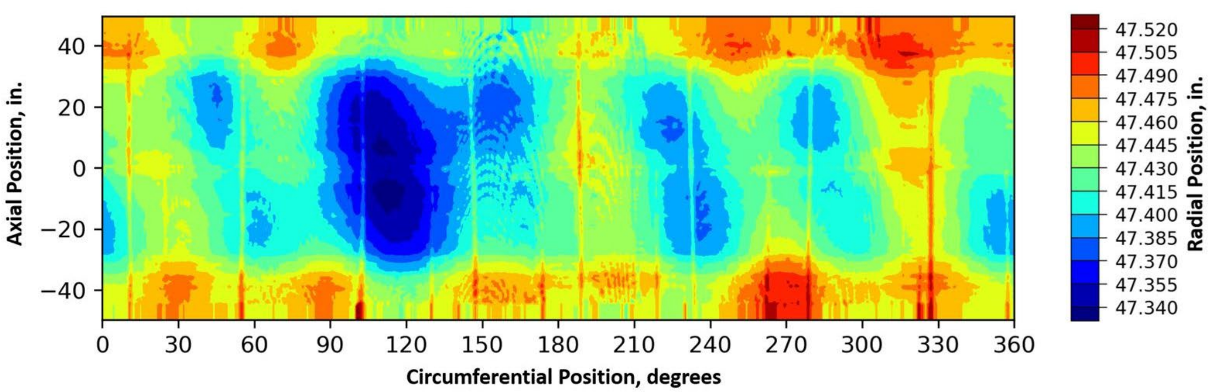

Figure 24. FEM as-installed radial midsurface position contour.

As the DIC-based OML surface data was used to update the radial imperfections, there was a noticeable change in OML surface positions between the as-manufactured and as-installed geometries. The OML surfaces for the as-manufactured and as-installed geometry are shown in Figure 3 and Figure 25, respectively.

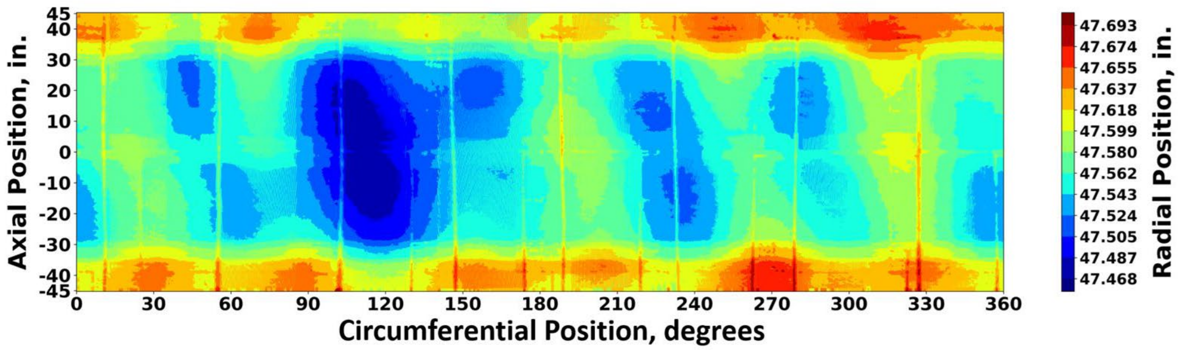

Figure 25. As-installed OML surface radial position contour.

The vertically oriented features of larger radial position in the as-installed OML surface were a result of interpolation between DIC systems. Though these features were included in the analysis because they were a part of the dataset, there was no indication they influenced the predicted buckling response. A comparison to characterize the change in radial position between the as-manufactured and as-installed geometry was made by subtracting the as-manufactured radial position from the as-installed radial position, and a plot of this changed radial position is shown in Figure 26. The contours of Figure 26 clearly indicate the origins of the six circumferential undulations first shown in Figure 24. Between the as-manufactured structured light scanning and the installation into the test facility, the radial position of the test article changed pattern in a significant (but still small in magnitude) manner in the number of wavelengths around the test article circumference.

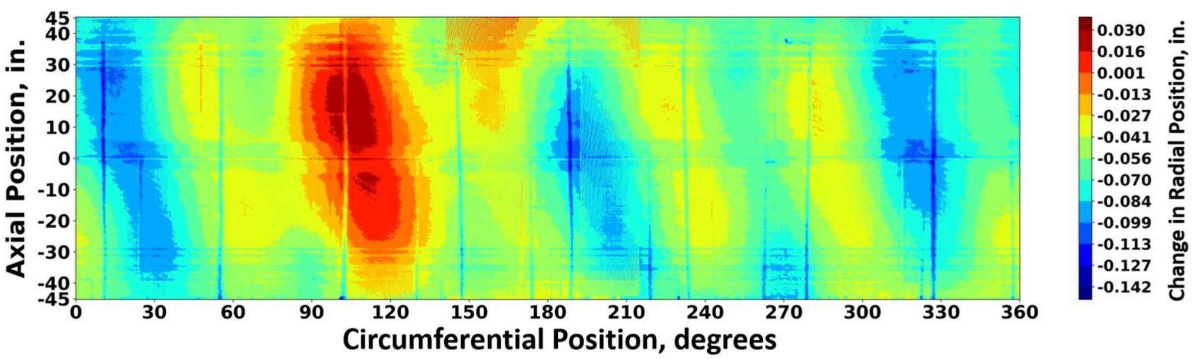

Figure 26. Change in radial position between the as-manufactured and as-installed midsurfaces.

When the FEM with the as-installed geometry was subjected to the LS12 loading conditions of 90% axial compression combined with 10% bending over the 0° circumferential position, buckling initiation was predicted to occur at 751.3 kips with an initial radial inward buckle near the 27.5-in. axial and 344° circumferential location. The as-installed predicted buckling initiation load was 10.3 kips, or approximately 1.35%, lower than the as-manufactured predicted buckling initiation load. The predicted axial position of the buckling initiation site stayed the same for models with both imperfection shapes, but the circumferential location of the buckling initiation site for the as-installed FEM was 4° farther away from the direction of maximum bending and closer to the experimental buckling initiation location as will be discussed later. Contours of predicted axial and radial displacements and axial and hoop strains at the predicted buckling initiation load of 751.3 kips are shown in Figure 27, Figure 28, Figure 29, and Figure 30, respectively. Minimal changes can be observed between the FEM as-manufactured and as-installed axial displacement contours shown in Figure 19 and Figure 27, respectively. The ranges of the radial displacement contours are comparatively similar for the FEM as-manufactured and as-installed imperfections in Figure 20 and Figure 28, but the patterns of the contours changed. Whereas the as-manufactured radial displacement contours are characterized by larger radially outward displacements over the area of bending at 0° with a few localized dimples and minimal radially outward displacement circumferentially opposite, the as-installed radial displacement contours are characterized by many more localized dimples whiles observing the trend of radially outward displacements over the area of bending. The number and distribution of local radially-inward dimples is larger and is observed to occur across the majority of the test article acreage. Axial and circumferential strain contours between the as-manufactured (Figure 21 and Figure 22, respectively) and the as-installed (Figure 29 and Figure 30, respectively) imperfections were of similar contour patterns, but the as-installed strains were slightly reduced in magnitude. The reduced strain magnitudes for the as-installed predictions were attributed to the slightly lower predicted buckling load of 751.3 kips for the as-installed FEM versus the 761.6 kips for the as-manufactured FEM.

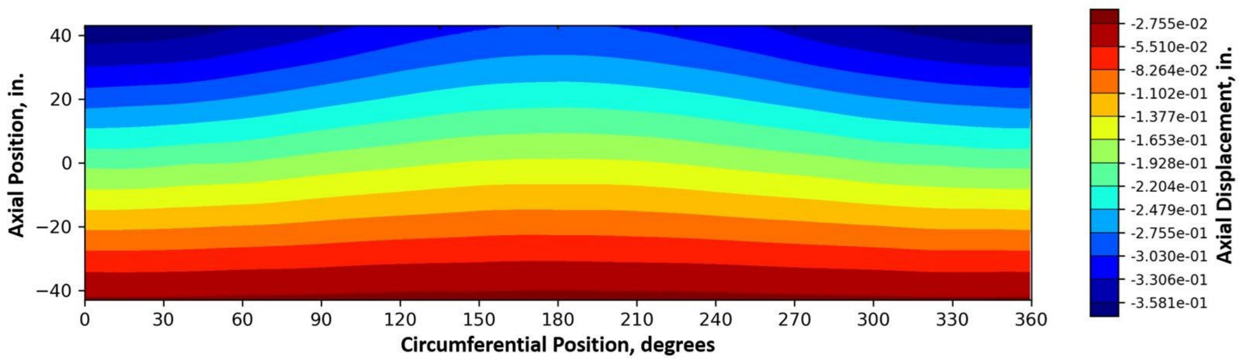

Figure 27. FEM as-installed axial displacement contour at predicted buckling load.

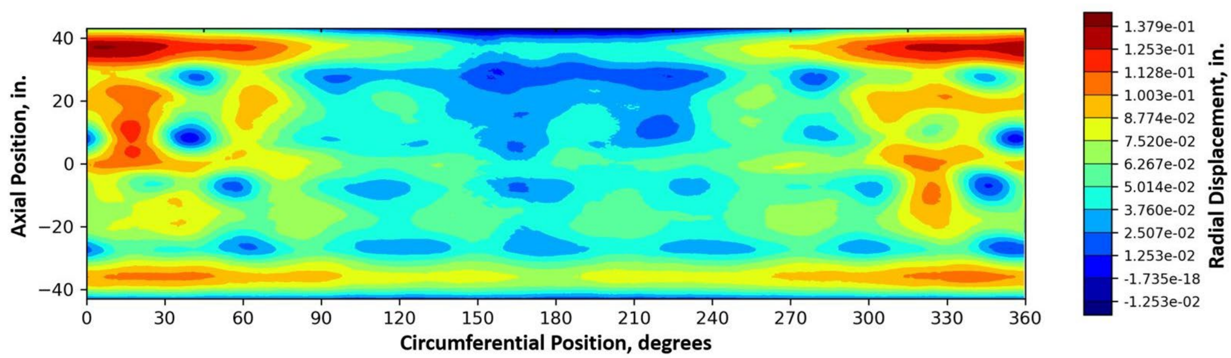

Figure 28. FEM as-installed radial displacement contour at predicted buckling load.

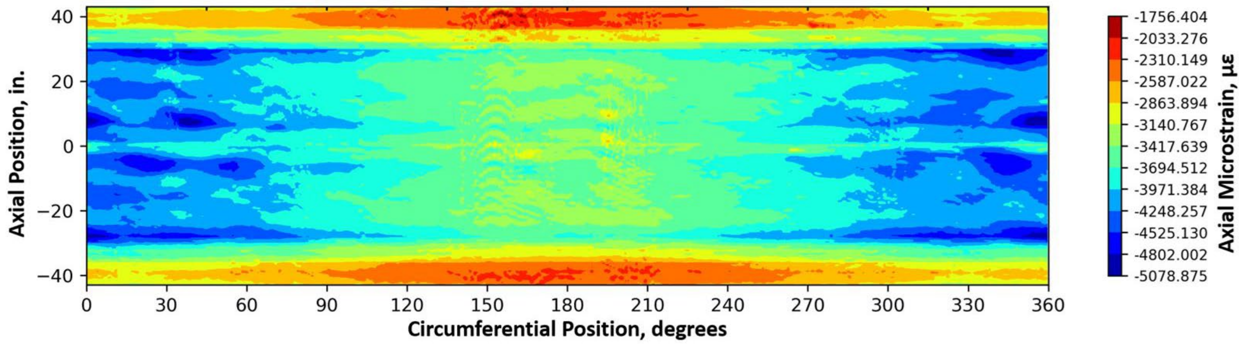

Figure 29. FEM as-installed axial strain contour at predicted buckling load.

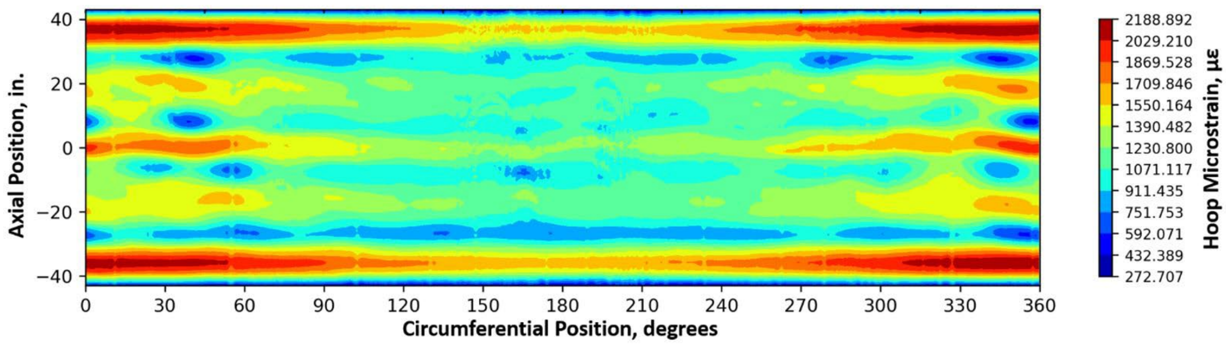

Figure 30. FEM as-installed hoop strains at predicted buckling load.

As previously reported, the experimental maximum load was 704.9 kips with an observed buckling initiation location near 27.5-in. axial and 331° circumferential location. When compared with the predictions from the model with the as-installed imperfections, the test article failed at 93.8% of the predicted maximum load and approximately 13° (or approximately 10.4 inches) away from the predicted primary buckling initiation location. Contours of the DIC-measured experimentally observed axial and radial displacements and axial and hoop strains before buckling initiated are shown in Figure 31, Figure 32, Figure 33, and Figure 34, respectively. As the test article failed 46.4 kips lower than predicted by the FEM as-installed configuration, contour comparisons of the DIC-measured displacements and strains to the numerical predictions closer to the experimental failure load are needed. The axial and radial displacements and axial and hoop strains extracted from the FEM as-installed configuration at a load of 705.3 kips, or merely 0.4 kips higher than the recorded experimental maximum load at buckling initiation, are shown in Figure 35, Figure 36, Figure 37, and Figure 38, respectively. The legend ranges between each DIC- and FEM contour pair were also made identical to aid comparison between experimental data and numerical predictions.

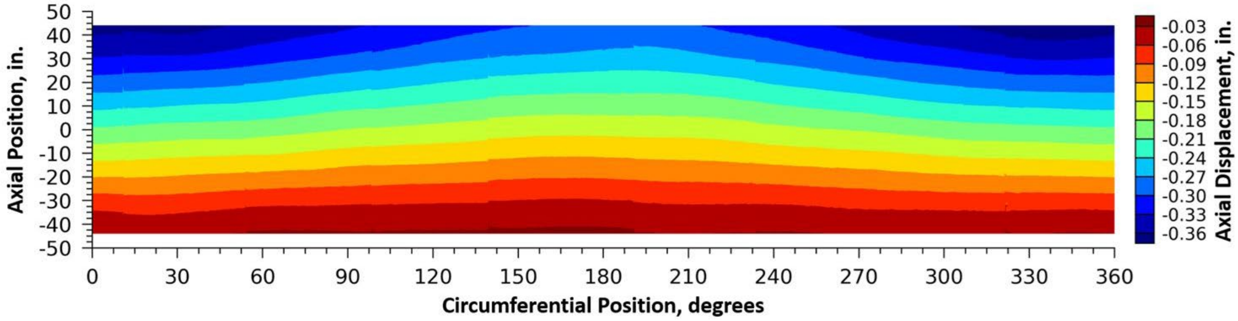

Figure 31. DIC-based axial displacement contour at experimental buckling load.

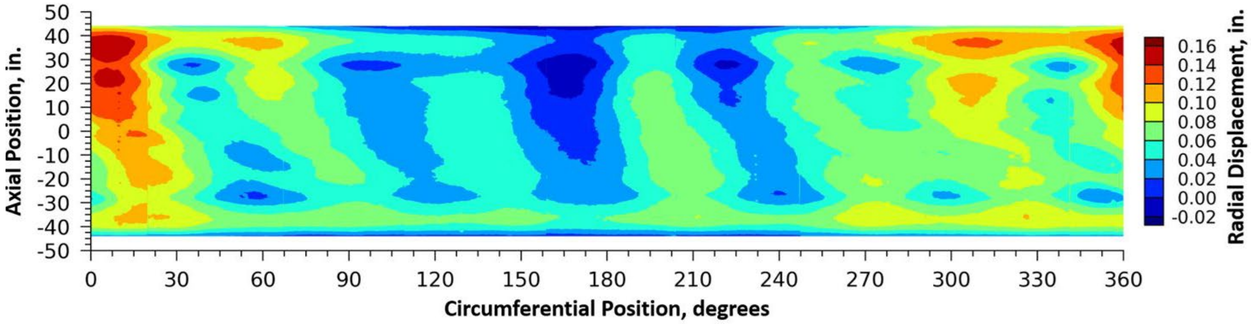

Figure 32. DIC-based radial displacement contour at experimental buckling load.

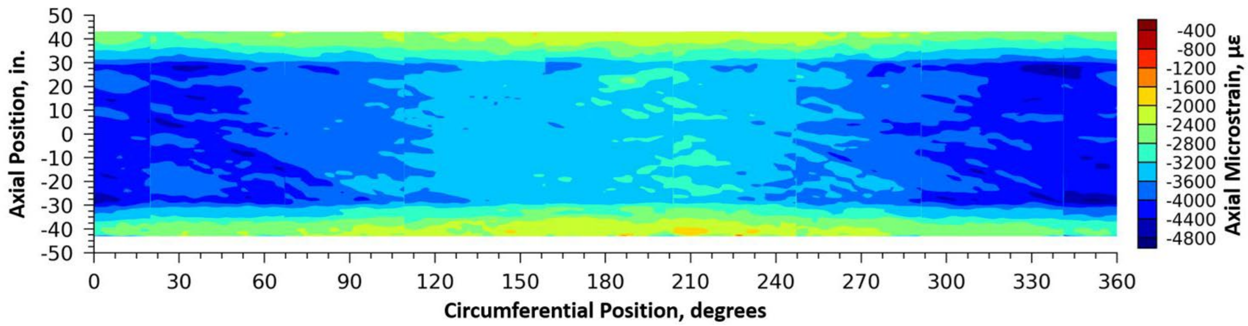

Figure 33. DIC-based axial strain contour at experimental buckling load.

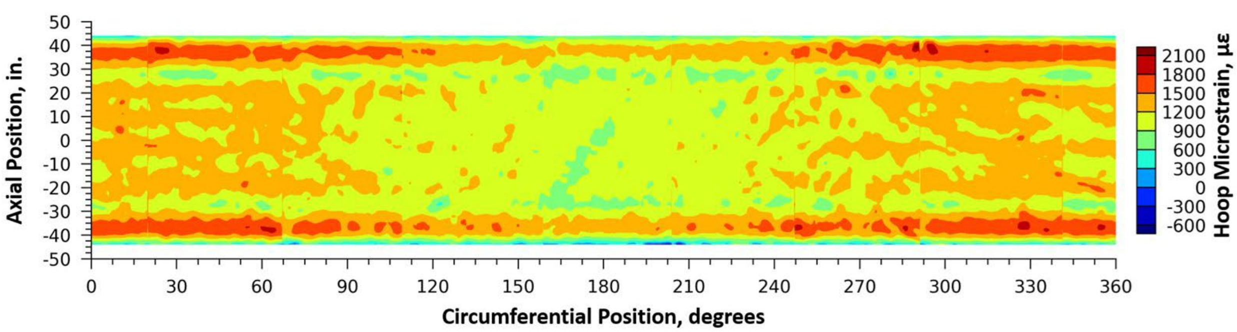

Figure 34. DIC-based hoop strain contour at experimental buckling load.

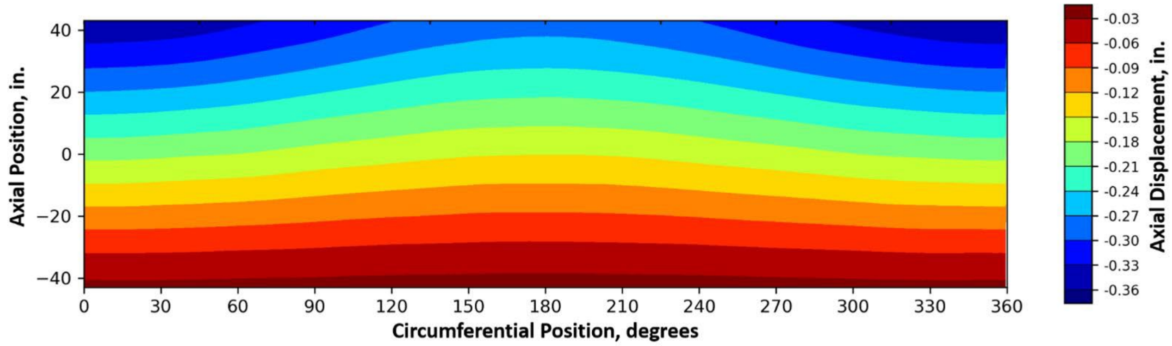

Figure 35. FEM as-installed axial displacement contour at 705.3 kips total load.

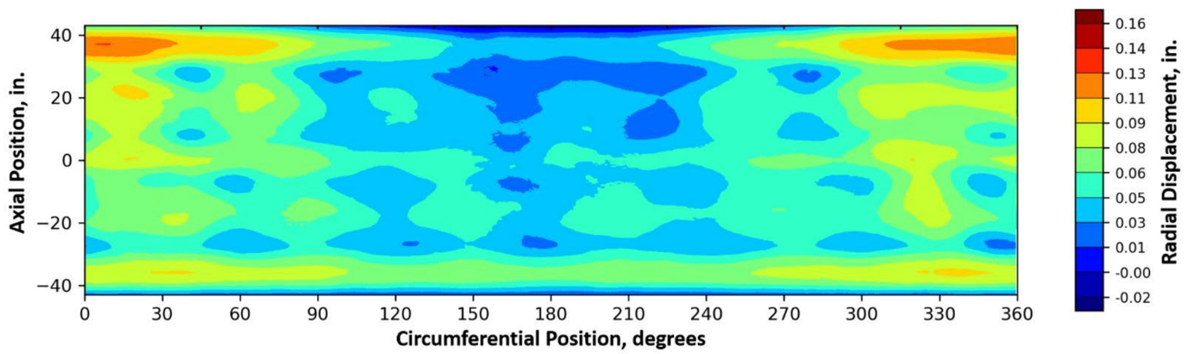

Figure 36. FEM as-installed radial displacement contour at 705.3 kips total load.

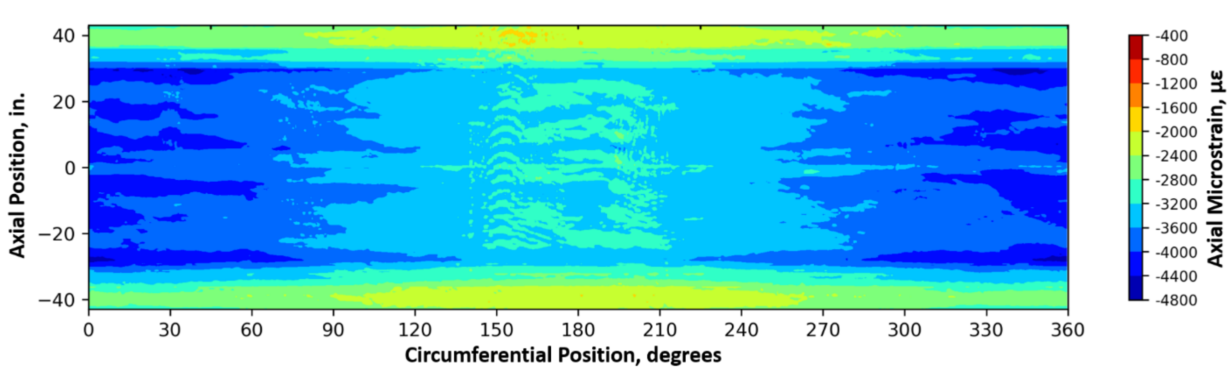

Figure 37. FEM as-installed axial strain contour at 705.3 kips total load.

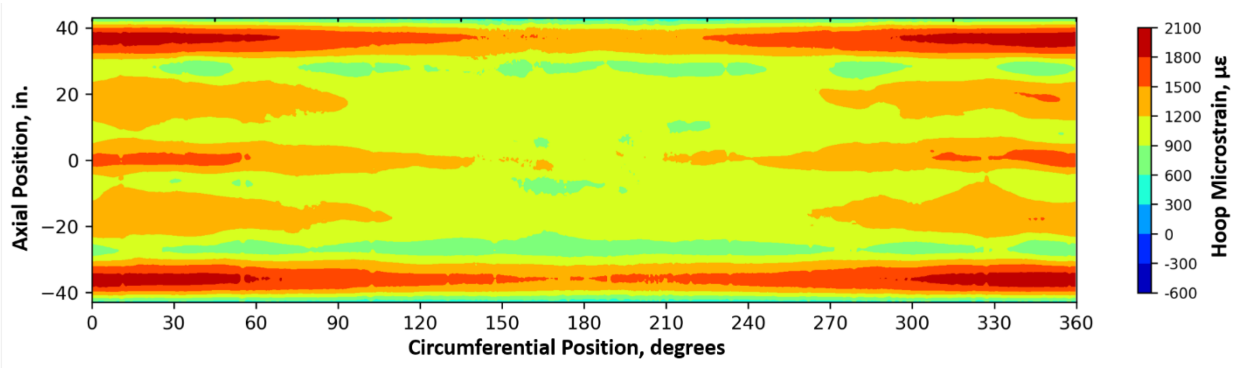

Figure 38. FEM as-installed hoop strain contour at 705.3 kips total load.

After the global loss of stiffness of the test article and before the failure mode could be identified, the control system switched to a position hold, as desired in the load control system, but the controlling displacement sensor output an erroneous displacement measurement due to the shockwave produced by the dynamic buckling event which led to actuation of the hydraulics and ultimately the failure of one of the associated load lines. It was determined after the test that the Temposonic transducer on one of the load lines had become detached from the load line. This caused anomalous signals to be sent to the control system when placed in displacement control because the control system was attempting to reposition the load line to correct the anomalous reading. In actuality, this caused the load line to enter compression, buckle, and shear off from the attachment pin at the actuator. Posttest inspection of CTA8.2B concluded that structural failure resulted from buckling initiation within the acreage of the test article. A photograph of the failure initiation location taken from the OML side is shown in Figure 39.

There were elements of agreement between the pretest predictions with the as-installed radial displacement contour whereby distinct features were common in both the analyses and the experiment. However, there were also notable differences. Both the analysis and experiment exhibited the same number and approximate position of 12 circumferential half-waves corresponding to localized regions of larger and smaller radial displacements. Half-waves are observed in the analysis as shown in both Figure 28 and Figure 36 and in the experiment as shown in Figure 32. There is broad agreement between the predicted and recorded axial displacement contours and predicted and recorded axial and hoop strain contours. The radial displacement contours exhibit the most difference between prediction and record in the sense that the FEM as-installed radial displacement contour in Figure 36 depicts a response with numerous inward and outward dimples in what may be described as a waffle pattern exhibiting a skewed direction away from purely axial and circumferential alignment. The recorded axial displacement contour in Figure 32, while also indicating local dimples, primarily exhibits longer wavelengths resembling troughs along the axial length of the test article. The same skewed behavior of the troughs is in excellent agreement with the same skewed angle as the waffle pattern from the pretest predictions.

The ranges of the scales between analysis and experimental contours differ at each respective buckling load, with the experimental contours typically having larger ranges (higher highs and lower lows) than their corresponding analysis contour counterparts at predicted buckling loads. A larger range in the experimental contour (Figure 32) was most clearly observed in the radial displacements where the inward-bending dimples have approximately 0.03-in. more displacement than predicted (Figure 28).

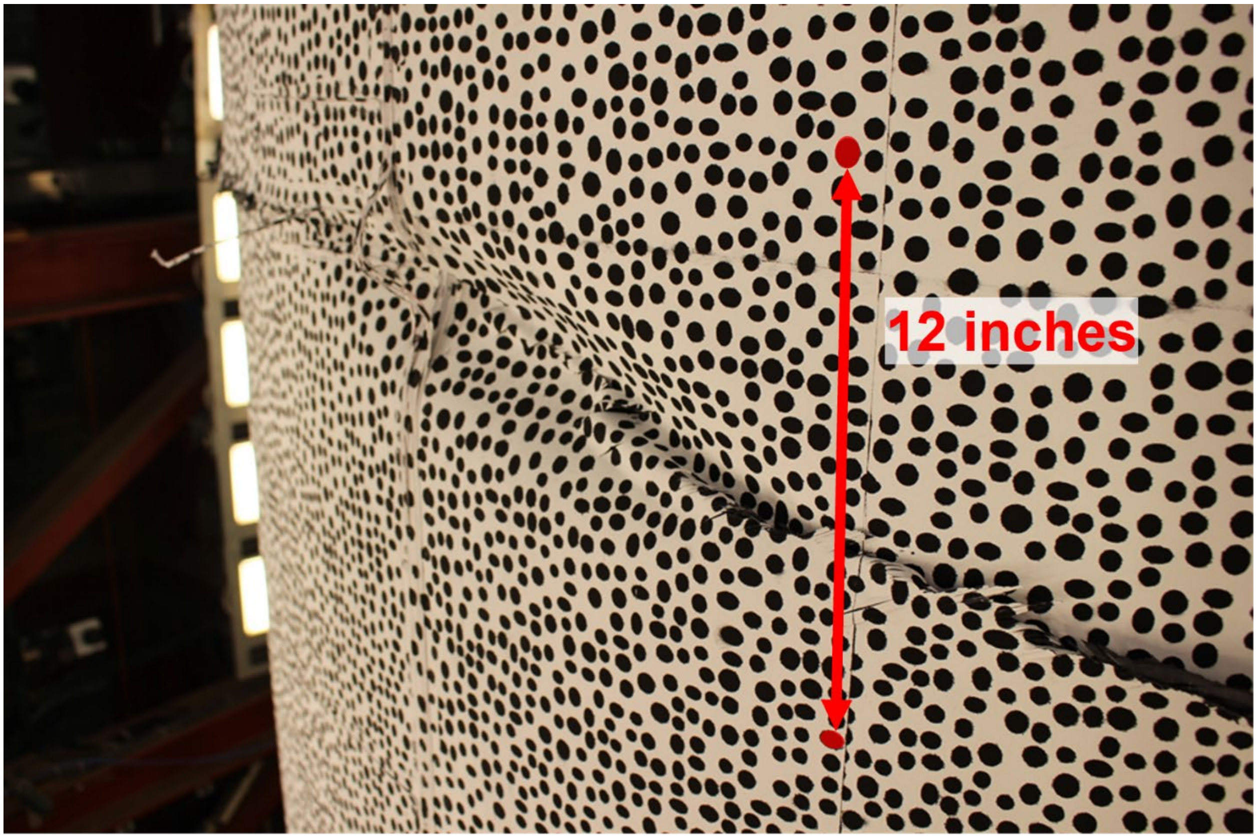

Figure 39. Photograph of the experimental buckling initiation location and propagated failure.

In addition to the radial displacement contours, the axial displacement contours also exhibit slight differences between the experimental (Figure 31) and predicted (Figure 27) behavior whereby the maximum experimental axial displacement was larger than predicted by slightly less than 0.03-in. The circumferential position of maximum axial end-shortening was near 0° in the predictions, but the location of maximum experimental axial end-shortening was shifted to between the 337°-345° position as shown in Figure 31. The shifted position of maximum axial end-shortening was also observed in other data such as the EDIs for axial end-shortening and is discussed later in this section. A comparison of the predicted and experimentally observed total load versus end-shortening is shown in Figure 40.

The total load values in Figure 40 were the summed loads from each of the eight load lines. The end-shortening was an average of four end-shortening calculations taken at the 0°, 90°, 180°, and 270° circumferential positions. Each end-shortening calculation was the difference between the axial displacement of an EDI attached to the top of the test article and the axial displacement of an EDI attached to the bottom of the test article for the same circumferential location as provided by the equations for δ_{D000A}, δ_{D090A}, δ_{D180A}, and δ_{D270A}. For example, the end-shortening calculation at the 0° circumferential position would be the difference between axial EDIs D317A and D113A, at 90° the difference between axial EDIs D318A and D114A, etc. The average of the four end-shortening calculations produce a single, global end-shortening history.

The test article was more compliant by approximately 8.6% at failure when comparing the end-shortening as calculated from the axial EDIs to their analysis-based equivalent. Also shown in Figure 40 is an end-shortening extracted by the low-speed DIC system.

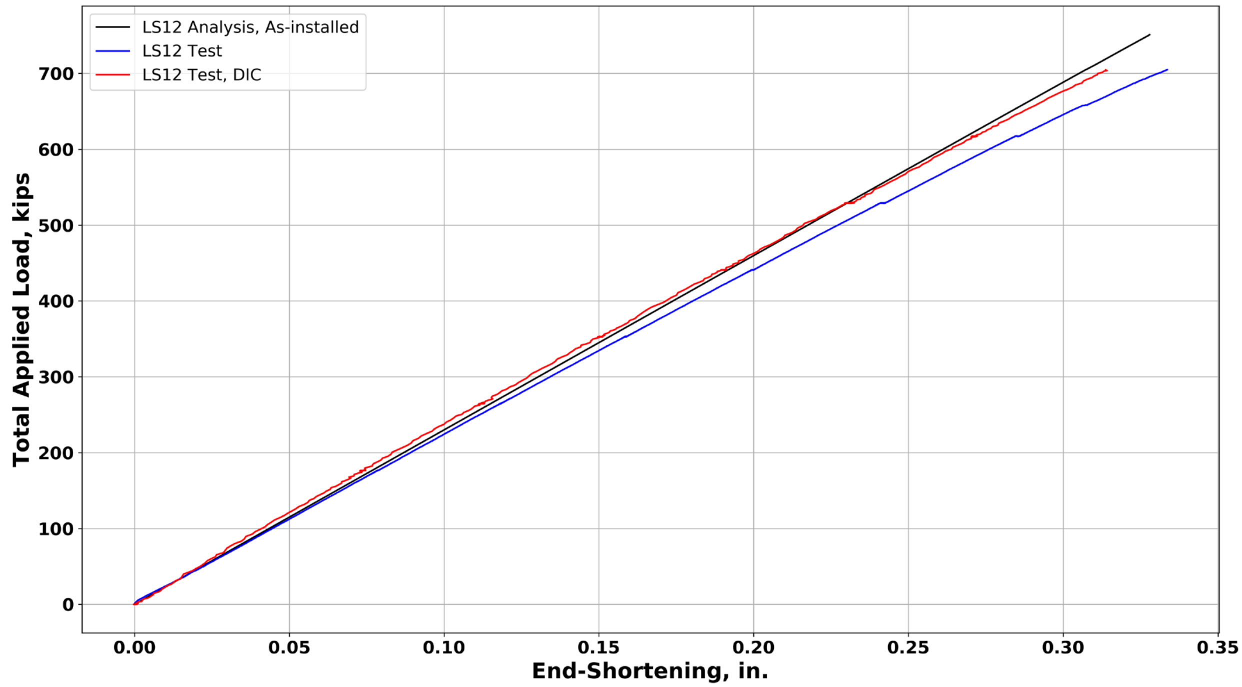

Figure 40. Test and analysis load versus end-shortening response.

Though the DIC-based end-shortening shows better agreement to the predictions, the axial length over which the DIC data was extracted was slightly shorter than the corresponding lengths extracted in the predictions and the experimental EDIs. The locations of points used for the DIC-based end-shortening were at 45-in. above and below the test article midlength and located at 0°, 90°, 180°, and 270° circumferentially. Because of the difference in extraction positions between the DIC-based axial displacements and the EDIs, the DIC-based end-shortening was not an exact comparison. When accounting for the abbreviated length by scaling to the full test article length, the DIC end-shortening would more closely agree with the experimental EDIs rather than the analysis.

Slight jogs (increasing displacement without change in load) in the experimental curve of Figure 40 at loads near 352 kips, 440 kips, 529 kips, and 617 kips were observed. The jogs up to and including the one at 617 kips were attributed to continued axial displacement during planned holds in the load sequence. The cause of the continued displacement was never definitively determined. Another jog was observed near 656 kips, but there was no planned hold at this point in the load sequence. Instead, the jog at 656 kips was attributed to a sudden event associated with a loud audible emission from the test article. The effect of the nonlinear event was observed in most of the instrumentation around the test article including instrumentation at the opposite circumferential position of maximum bending. Increased granularity in the test data, and observation of the nonlinear event at 656 kips, was possible when observing the individual axial EDI displacement calculations. Total load versus the four end-shortening calculations from axial EDI sensors, the corresponding calculations from the as-installed geometry analysis, and DIC-based end-shortening are shown in Figure 41.

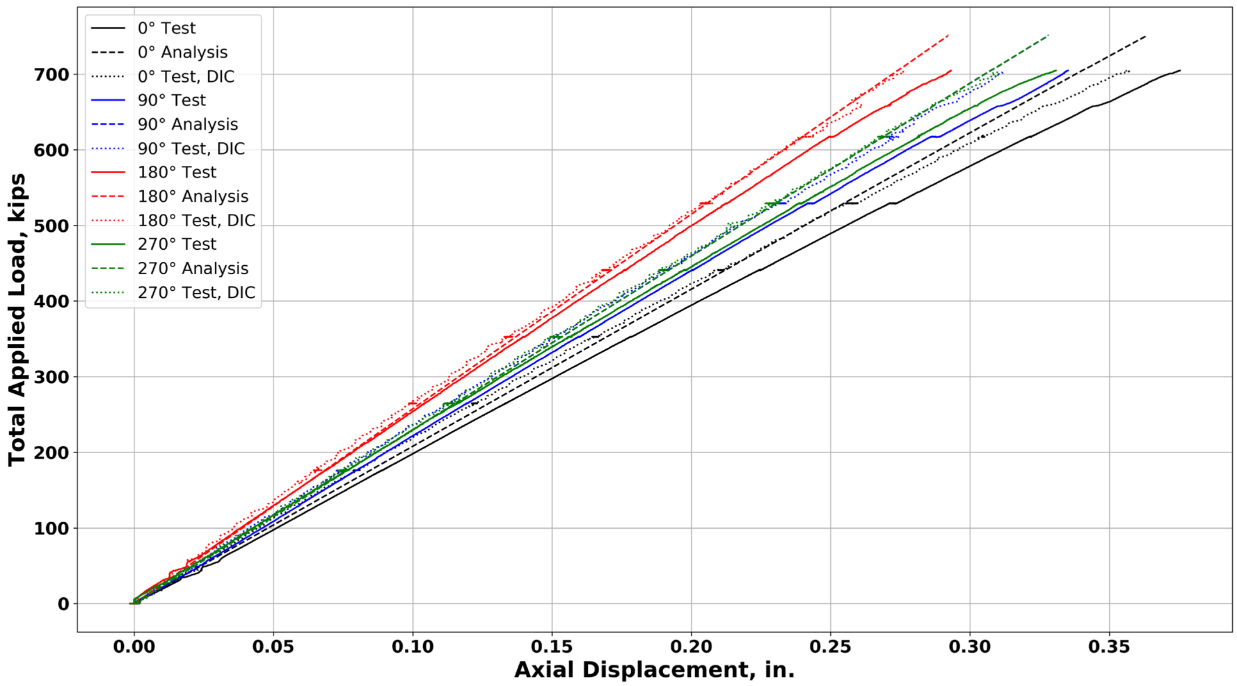

Figure 41. Test and analysis load versus axial EDI response.

Though the predicted responses for the 90° and 270° axial displacements (dashed blue and green, respectively) were coincident, the experimental responses indicate the 90° position (solid blue) of the test article underwent more end shortening than the 270° position (solid green) as denoted by the larger value of end shortening shown with the blue curve. As in Figure 40, the experimental response indicates a more compliant article than predicted. Slight nonlinearity in the experimental response after 656 kips was observed for the 90° and 270° locations. An increase in compliance was observed at the 270° location while a small but distinct decrease in compliance was observed at the 90° location after 656 kips but before failure.

The cause of the nonlinearity at 656 kips was unresolved, but one conclusion that could be inferred was that the audible emission event at 656 kips caused the change in compliance such that the load control system applied increased displacement rates around the 270° location to maintain the as-specified load distribution requirements for the load sequence.

Even finer granularity of the loading may be observed when inspecting the total load versus displacement data measured at the individual load lines. Two load lines are shown per figure, and the load lines are grouped in each figure based on the similar loads imparted on the test article from the load sequence specification provided in Table 11. For example, load line 2 and 3 were intended to have similar loading as were load lines 4 and 1, 8 and 5, and 7 and 6 and are shown in Figure 42, Figure 43, Figure 44, and Figure 45, respectively. Equivalent pretest predictions load versus displacement are shown along with the experimental data. The load line displacements are negative because of the sign conventions defined for the test. The hydraulic actuators apply a tensile load into the load lines by displacing downwards (hence negative values) and, as previously stated, tension applied to the load lines resulted in compression applied to the test article.

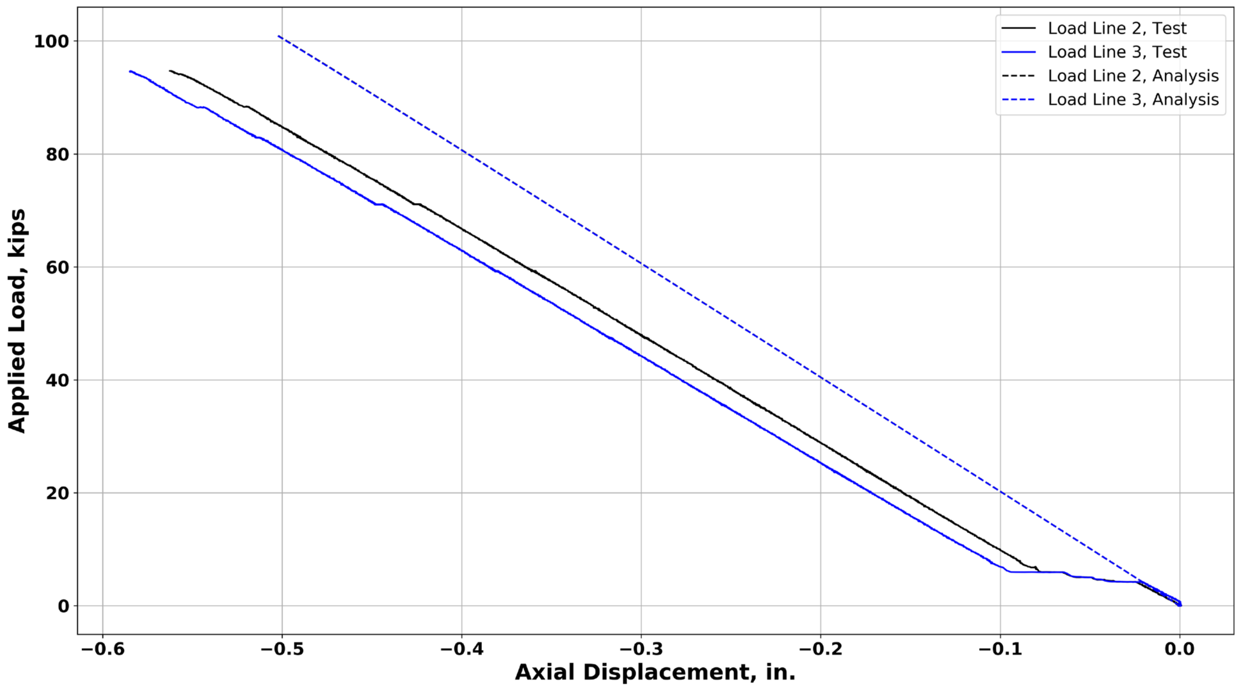

Figure 42. Load line response about location of applied bending.

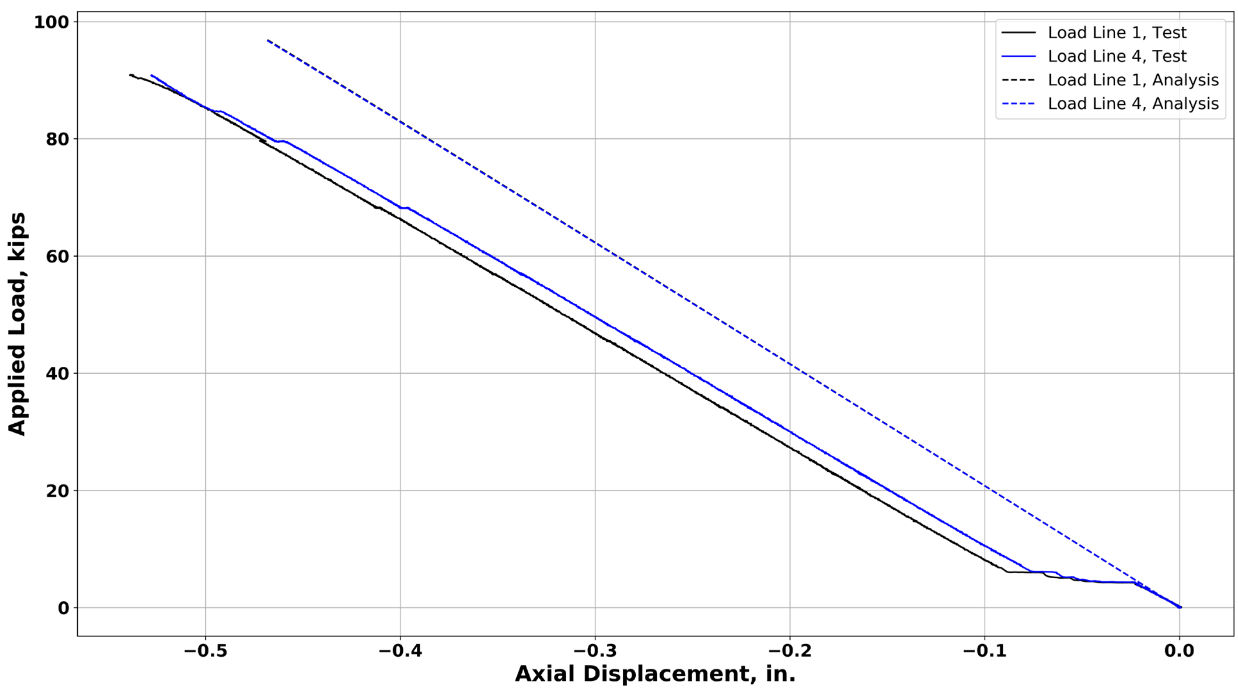

Figure 43. Load line 1 and 4 response.

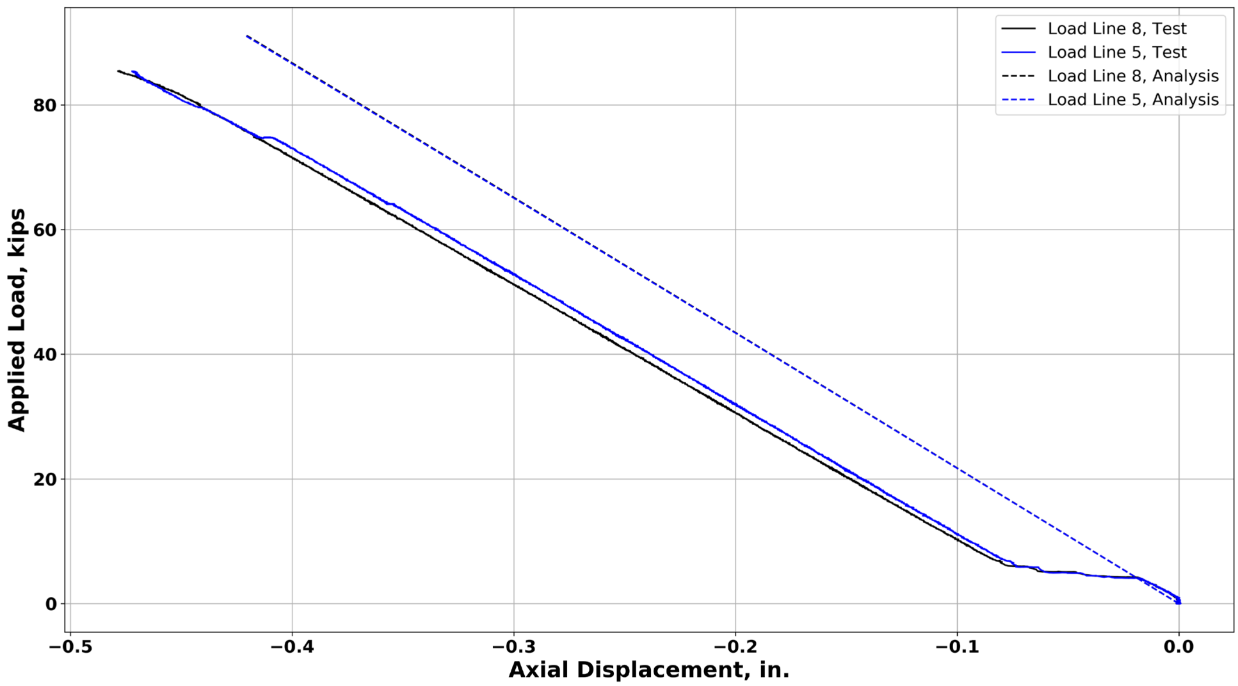

Figure 44. Load line 8 and 5 response.

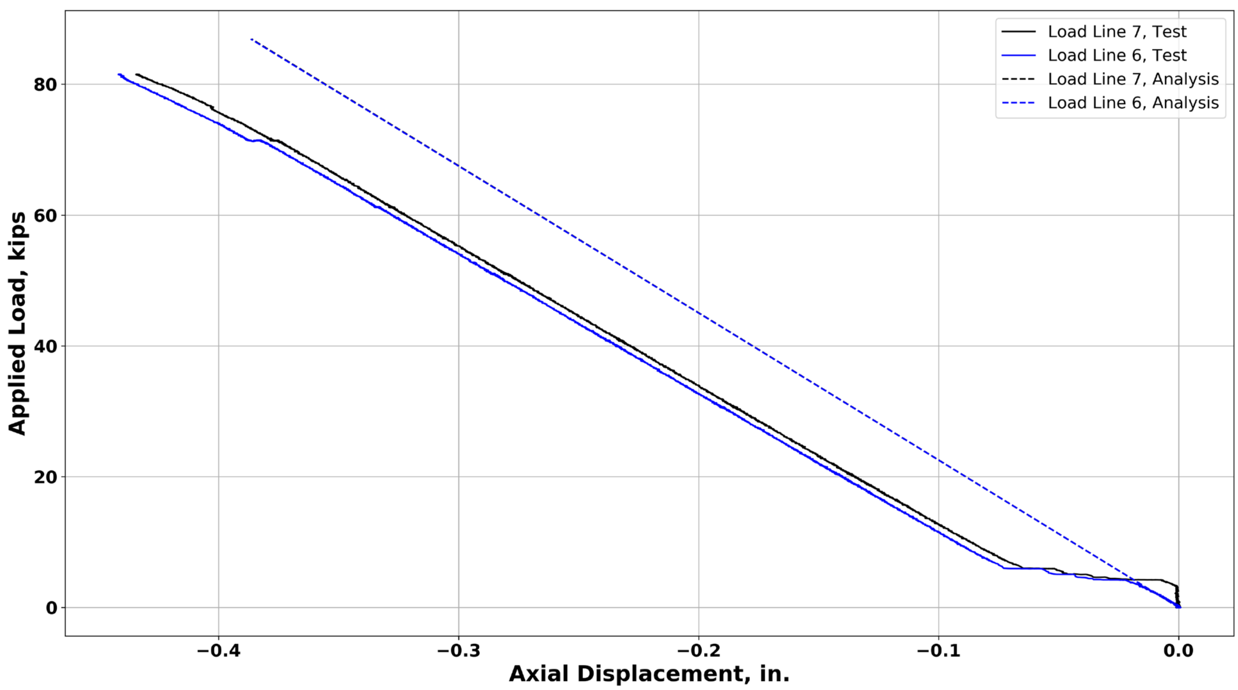

Figure 45. Load line response opposite location of applied bending.

Within the initial 0.1-in. of applied displacement, there was pronounced nonlinearity in the experimental data due to the transition from compressive to tensile loads in the load lines. The transition occurs as the weight of the upper loading structure was gradually imparted upon the test article. After the full weight of the structure was supported by the test article, there was a brief period where the pin connected to the clevis and eye bracket (parts 90M11182-4, 90M11267-4, and 90M11268-5 used to connect the load lines to the upper loading structure in the test facility and shown in Figure 6) shift position due to fitting tolerances. During this transition period, there was extra displacement to move through the tolerance until where the load lines then contribute compressive loads to the test article beyond the weight of the upper loading structure. In addition to the excess displacement during the transition from compression to tensile loads in the load lines, the experimental data from the load lines indicate a slightly more compliant response than predicted by analysis in support of the previously discussed experimental observations. Brief jogs in the displacement during the previously discussed load sequence holds and again at 656 kips were clearly indicated by the horizontal shifts in the load line data.

Numerous strain gauges were instrumented for testing CTA8.2B. A brief overview of the nomenclature and positioning of select strain gauges is presented, and a discussion on the general agreement with pretest predictions follows.

Back-to-back strain gauges were instrumented on both the OML and IML surfaces of CTA8.2B in a repeating grid pattern. Gauge nomenclature begins with specifying whether the gauge was on the OML or IML surface. A gauge number consisting of three digits indicates the specific gauge number and was associated with the strain gauge map in the Appendix. All gauges on the OML surface consisted of odd numbers, and all gauges on the IML surface consisted of even numbers. Back-to-back gauges (those at the same axial and circumferential position but on the OML and IML surfaces) were sequentially numbered. The last part of the gauge identification was whether the gauge channel was either an axial or hoop strain data channel. For example, gauge OML009A was on the OML surface tracking axial strain located at the -29-in. axial and 0° circumferential position whereas IML010A was at the same location on the IML surface.

Strain gauges OML009A, OML011A, OML013A, OML015A, and OML017A were located on the OML surface at the 0° circumferential position at -29-in., -14-in., 0-in., 14-in., and 29-in. axial locations from the midline, respectively, and LS12 load versus strain responses are shown in Figure 46. Agreement between the experimental test and pretest predictions was overall considered reasonably good with many of the predicted strains within 10% of the recorded strains until failure. The nonlinearity at 656 kips was observed in gauges OML009A and OML011A in the AFT section of the acreage, but the gauges in the FWD section (i.e. OML017A) did not observe much response to the event. Gauge OML017A exhibited the least agreement with the predicted strain, but the observed response was within family. Correspondingly, strain gauges IML010A, IML012A, IML014A, IML016A, and IML018A were located on the IML surface at the same respective axial and circumferential positions. LS12 load versus strain responses for these IML gauges are shown in Figure 47. Lower agreement was observed between the IML experimental test gauges and pretest predictions compared to the OML as the predictions were approximately 500 microstrain in deviation at the instance of failure. Additionally, all of the IML gauges in Figure 47 exhibited lower strain magnitudes than predicted except for the midline location which exhibited larger strain magnitude than predicted. As the deviations from predictions were consistent throughout loading during LS12, the disagreement is unlikely to be the result of localized material failure or other nonlinear events such as the audible emissions heard during loading. Instead, the consistent disagreement throughout loading indicate that the FEM as-installed configuration insufficiently captured the geometric state or loading introduction effects of the test article. Since the OML gauges were in overall good agreement at the same locations, differences between the FEM as-installed analysis and the state of the test article about 0° appear restricted to the IML surface.

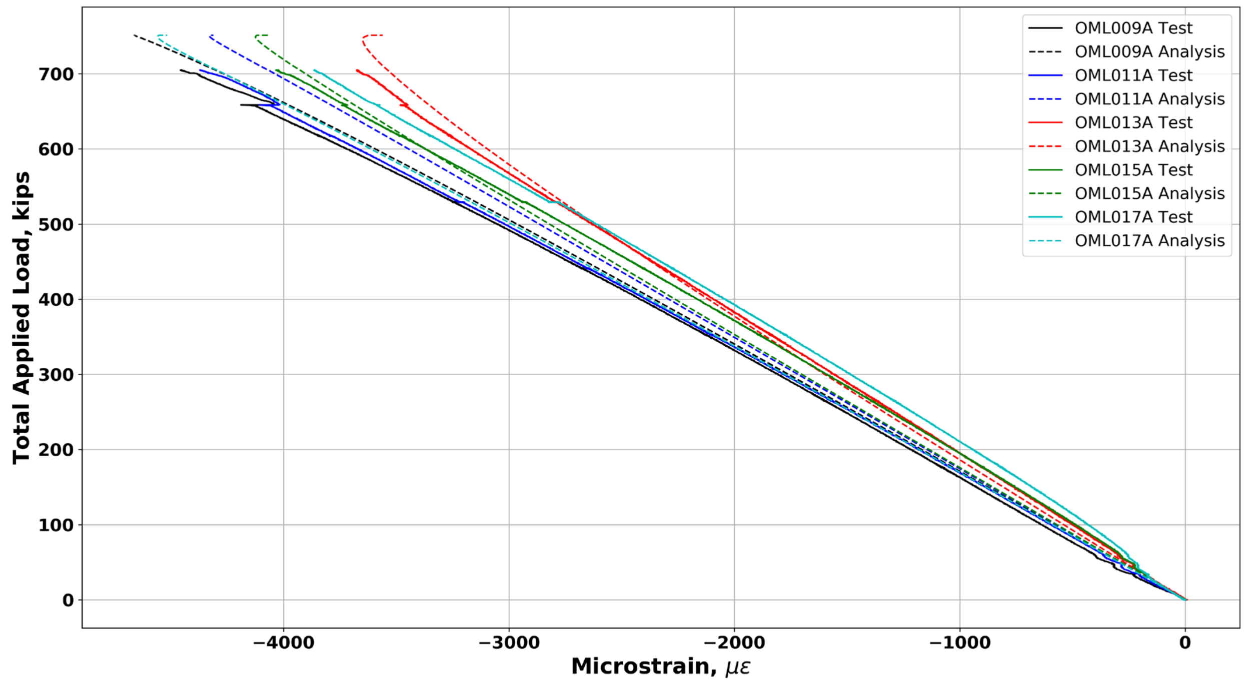

Figure 46. Strain history for axial OML acreage gauges about 0°.

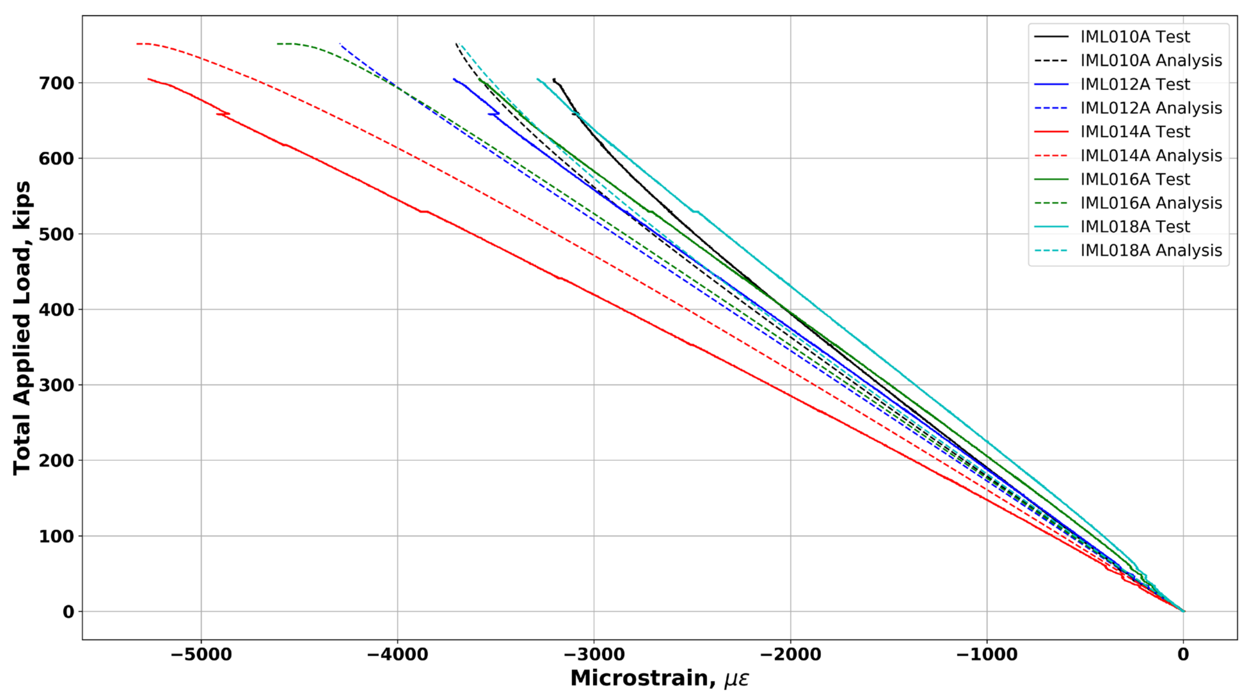

Figure 47. Strain history for axial IML acreage gauges about 0°.

Strain gauges numbered 035 through 044 were at the OML and IML 45° circumferential position at -29-in., -14-in., 0-in., 14-in., and 29-in. axial locations and are shown in Figure 48 and Figure 49. Agreement between the experimental test and pretest predictions was again within 10%.

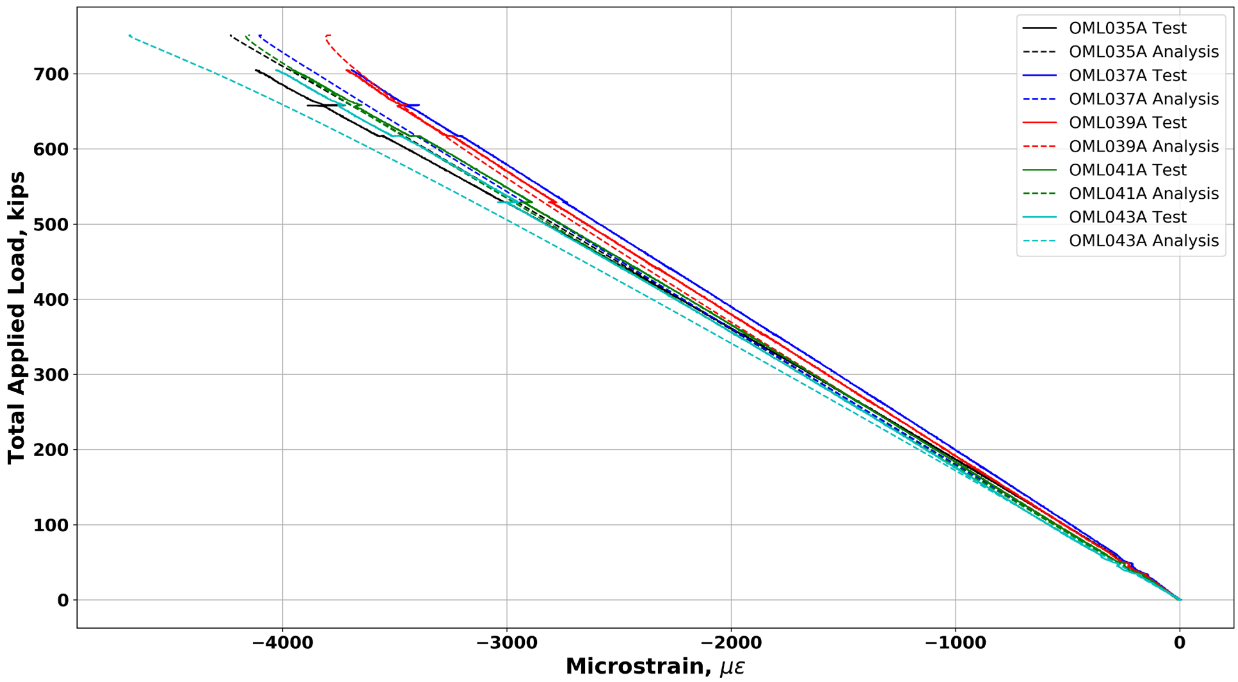

Figure 48. Strain history for axial OML acreage gauges about 45°.

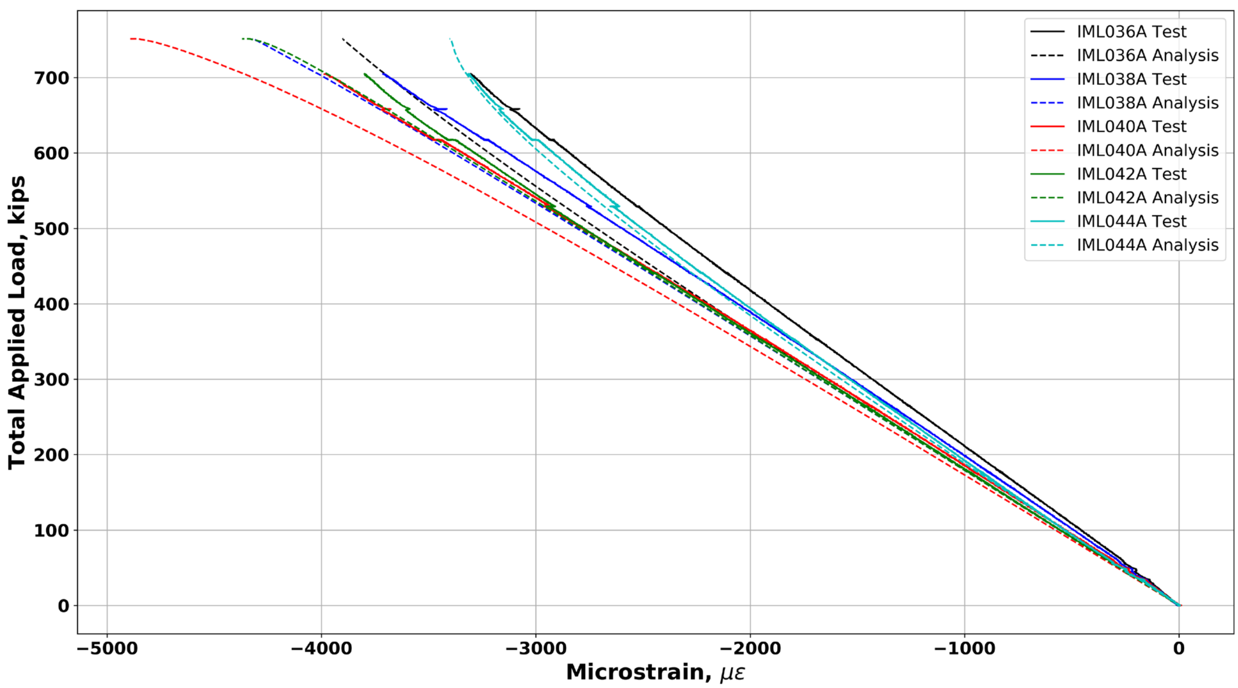

Figure 49. Strain history for axial IML acreage gauges about 45°.

Strain gauges numbered 191 through 200 were at the OML and IML 315° circumferential position at -29-in., -14-in., 0-in., 14-in., and 29-in. axial locations and are shown in Figure 50 and Figure 51. Agreement between the experimental test and pretest predictions was within 10%.

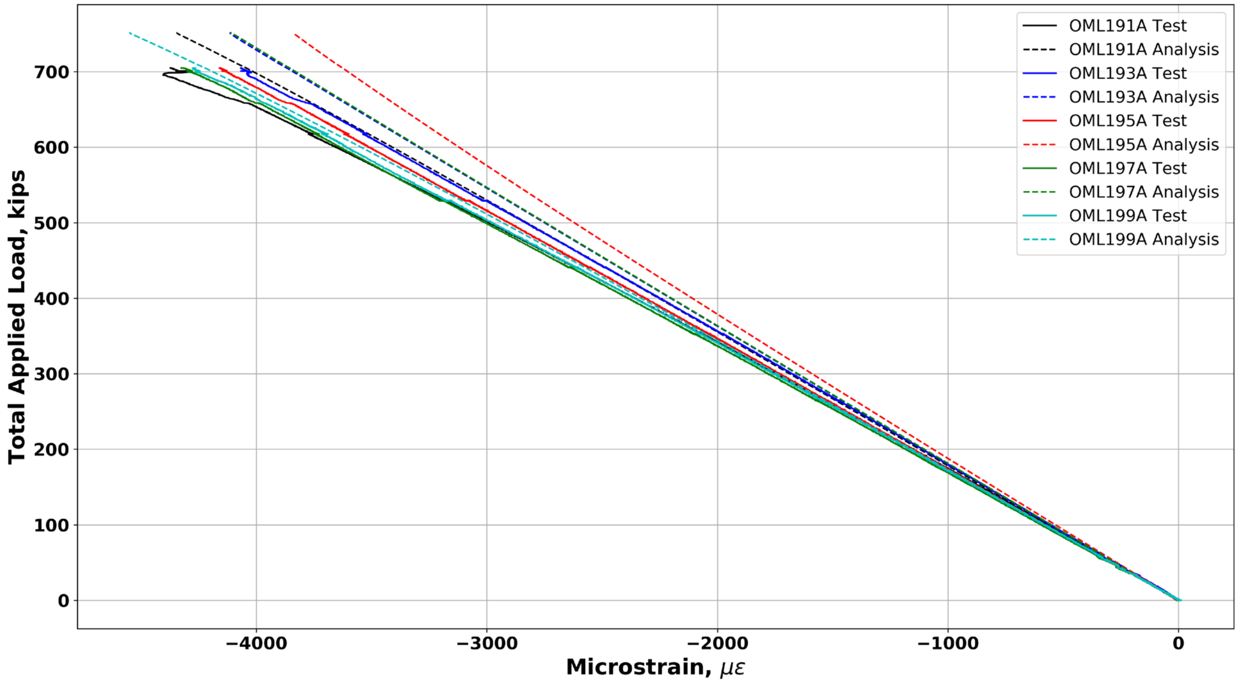

Figure 50. Strain history for axial OML acreage gauges about 315°.

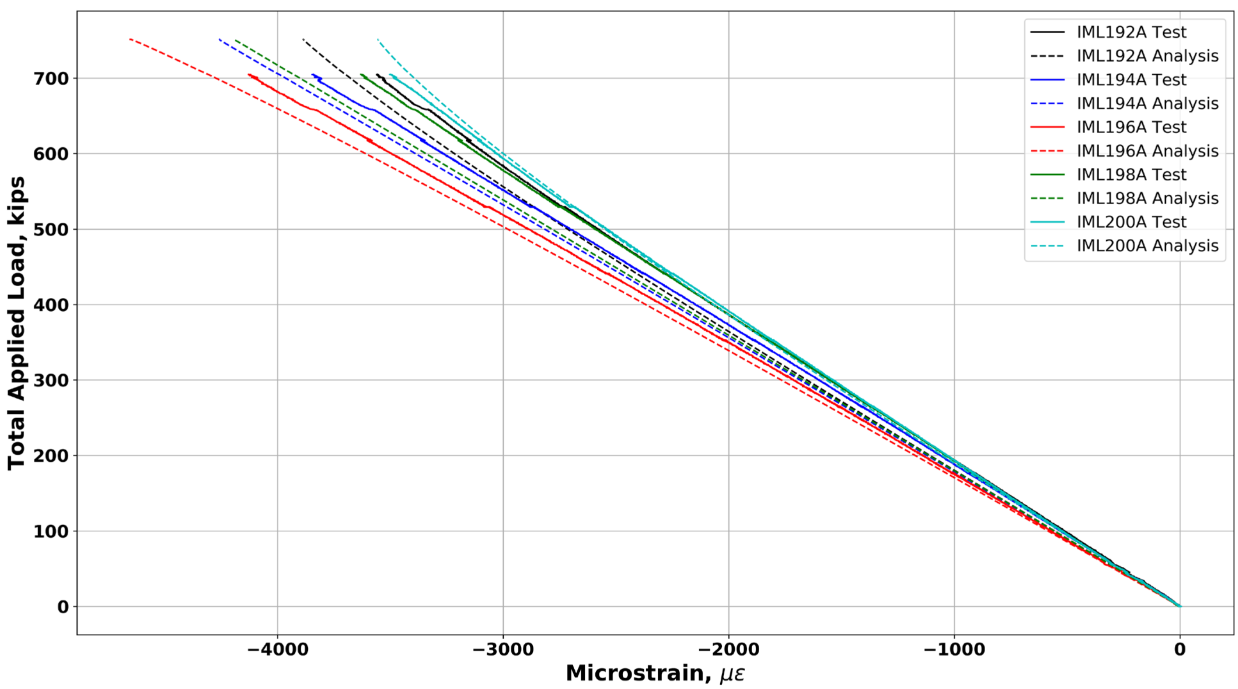

Figure 51. Strain history for axial IML acreage gauges about 315°.

Strain gauges numbered 113 through 122 were at the OML and IML 180° circumferential position at -29-in., -14-in., 0-in., 14-in., and 29-in. axial locations and are shown in Figure 52 and Figure 53. Disagreement between the experimental test and pretest predictions was typically more than 10%. For the IML gauges, the recorded strains indicated a less compliant response (over predicted strains for a given load) while the OML gauges recorded strains that indicated a more compliant response (under predicted strains for a given load).

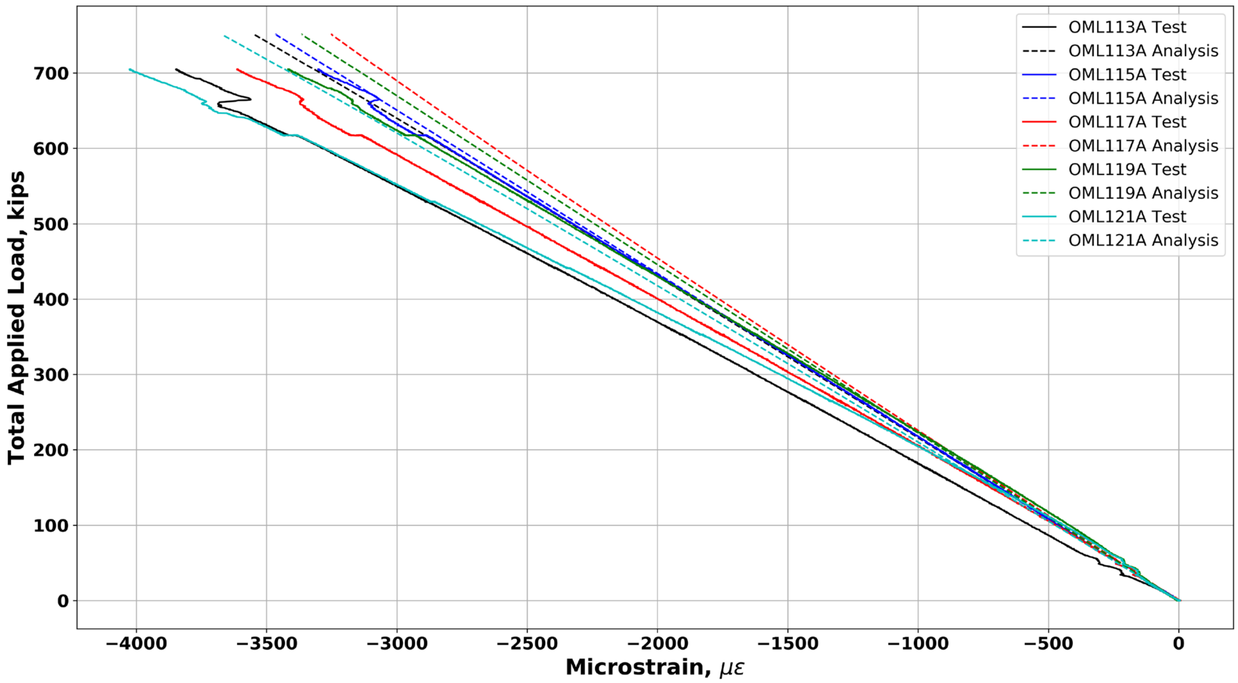

Figure 52. Strain history for axial OML acreage gauges about 180°.

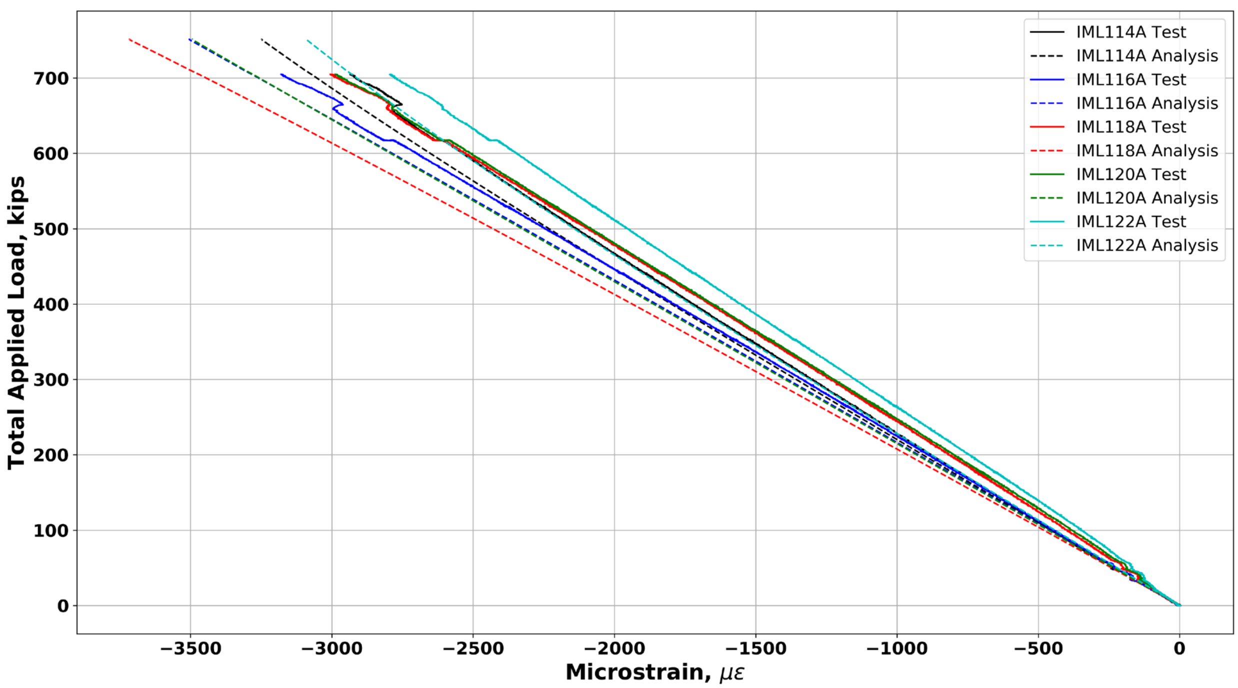

Figure 53. Strain history for axial IML acreage gauges about 180°.

The gauges at the 180° circumferential position also captured strain responses that provide possible insight into the previously discussed axial displacement jogs. Specifically, gauges on both the IML and OML at 180° observed an increase in strain at the event at 617 kips. The event that occurred at 656 kips caused decrease in strain. One conclusion that could be inferred from this response is that one side of the potting, though coated in release agent, suddenly slipped against the attachment ring at 617 kips and the other side slipped against the end ring at 656 kips. The change in boundary conditions (from one of high friction or effectively clamped) to one of sliding could reasonably result in the behavior observed in the AFT 180° acreage strain gauge responses. Complex boundary interaction is often difficult to accurately predict even with the well-development numerical models that were used. The HS-DIC contours were critical to determine the buckling initiation location. High-speed cameras collected images at 10,000 fps as previously mentioned. This rate results in an image being taken every 0.0001 of a second. A radial displacement contour created from images captured four frames (or 0.0004 seconds) before buckling initiation could be detected is shown in Figure 54.

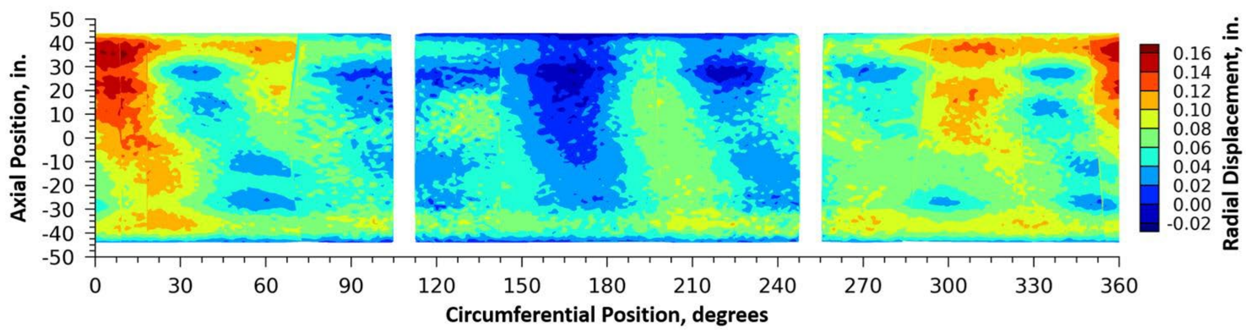

Figure 54. HS-DIC radial displacement contour four frames before buckling initiation.

There was excellent agreement of the contours in Figure 54 and Figure 32 (the last low-speed DIC contour prior to failure). Three high-speed image frames (or 0.0003 seconds) after that shown in Figure 54, possible formation of an inward-deforming feature was observed near the 27.5-in. axial and 331° circumferential position of the test article and is encircled with a dashed overlay in Figure 55. The next frame collected (or 0.0001 seconds) after the one shown in Figure 55 was determined to be the buckling initiation moment which led to global failure of CTA8.2B and is shown in Figure 56. The location of buckling initiation is denoted again with an encircled dashed overlay.

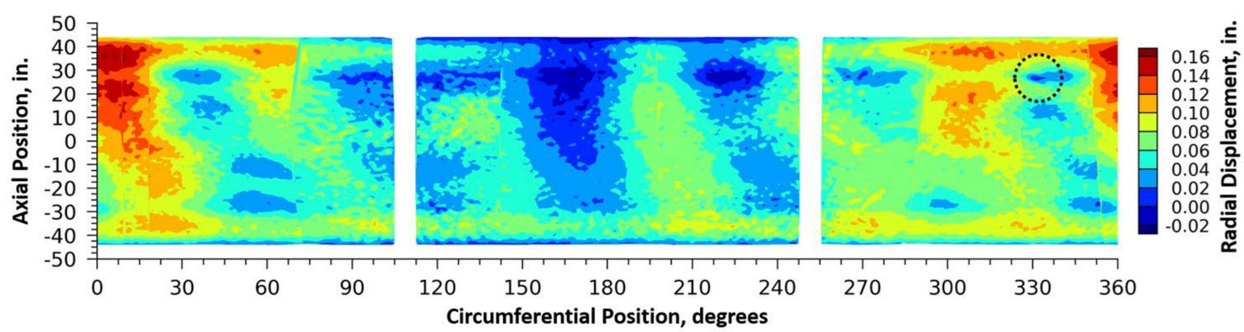

Figure 55. HS-DIC radial displacement contour one frame before buckling initiation.

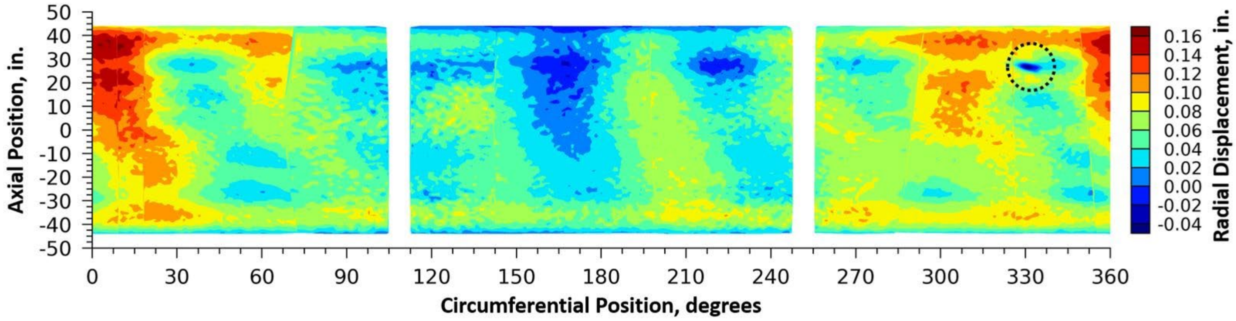

Figure 56. HS-DIC radial displacement contour at buckling initiation.

After initial inspection of the test data, posttest analyses were conducted in an attempt to increase the agreement of the analysis with the buckling load and overall response observed in the experiment. Two primary posttest analysis were investigated. The first was created using an updated radial midsurface position based on DIC data collected between the conclusion of the last noncritical load sequence and the failure load sequence. It was speculated that this updated geometry was influential if the OML surface geometry of the test article had changed between installation and LS12, but after analysis was conducted, the updated geometry as implemented was not as influential. The pre-LS12 based imperfections did not improve the test-analysis correlation.

A second posttest analysis attempted to capture the slightly skewed location of maximum bending about the 340° circumferential location observed from test data. The values in Table 11 were modified to impart maximum bending around the 340° location in the analysis, but like the pre-LS12 based imperfection analysis, bending over 340° did not increase test-analysis correlation. The pretest analysis using the as-installed radial-midsurface position and as-manufactured shell thickness geometric imperfections was the analysis that exhibited the best test-analysis correlation for CTA8.2B. The test article failed at 93.8% of the predicted maximum load and approximately 13° (or approximately 10.4 inches) away from a primary buckling initiation location when the as-installed imperfections were used in the analysis. One of the primary goals for the SBKF project was to update buckling knockdown factors for thin cylindrical shell designs and validate numerical methods for analysis-based shell buckling design guidelines. Using the guidelines recommended in NASA SP-8007 for the class of orthotropic shell representing CTA8.2B, the calculated knockdown factor is 0.562, or a 43.8% reduction from the linear critical buckling load. Geometrically nonlinear analysis of a FEM using the as-installed radial and thickness geometric imperfections predicted a buckling load at 751.3 kips which is 76.9% of, or a 23.1% reduction from, the linear buckling load. CTA8.2B failed at 704.9 kips which is 72.1% of, or a 27.9% reduction from, the linear buckling load. The analysis-based modeling methods used for CTA8.2B indicate there is conservatism in the buckling knockdown factor design guidelines.

5.0 Concluding Remarks

CTA8.2B was the fourth composite test article designed and tested as part of the SBKF project. CTA8.2B was intentionally designed to induce global buckling prior to structural strength failure. The 8-ft diameter, 100-in. long test article was designed by researchers at NASA LaRC in the Structural Mechanics and Concepts Branch and was manufactured with an automated fiber placement robotic machine for the facesheets, hand placement for the honeycomb core, and an autoclave process for curing of the structure by the Composite Technology Center at NASA MSFC. The honeycomb-core sandwich composite shell was constructed with carbon-epoxy facesheets composed of unidirectional IM7/8552-1 carbon fiber-epoxy prepreg and Hexcel 3.1 and 8.1 pcf aluminum core. Numerous types of instrumentation and photographic/video systems were utilized during the test including strain gages, displacement transducers, load cells, and low-speed and high-speed digital image correlation. Seven of the load sequences, LS1 – LS6 and LS10, were considered subcritical load sequences where failure was neither intended nor expected to occur. The combined compression and bending load sequence to failure was LS12. The experimental maximum load was 704.9 kips with an observed buckling initiation location near 27.5-in. axial and 331° circumferential location.

The predicted linear bucking load, P_{cr}, of the geometrically perfect test article with nominal material properties and metallic attachment rings (approximating the clamped boundary conditions at both ends) and subjected to a uniform compression load was 979,643 lbf. The corresponding critical bending linear buckling moment was calculated to be 23.51x10^6 in-lbf. The predicted linear buckling load under combined 90% axial compression and 10% bending load, P_{cr}^{CL}, was 977,283 lb. Geometrically nonlinear analyses of a finite element model with measured as-manufactured radial midsurface position and shell thickness imperfections with the entire test apparatus predicted the axial buckling load, P_{cr}^{NL}, equal to 836,900 lbf, and a total predicted buckling load of 761,600 lbf for combined axial compression and 10% bending in the 0° direction.

Geometrically nonlinear analysis of a finite element model with measured as-installed radial midsurface position imperfections, collected by the low-speed DIC system after the test article was installed into the test structure, and the as-manufactured shell thickness imperfections predicted a total buckling load of 751,300 lbf for combined axial compression and 10% bending in the 0° direction. The test article failed at 93.8% of the predicted nonlinear maximum load (and 72.1% of the linear buckling combined load) and approximately 13° (or approximately 10.4 inches) away from a primary buckling initiation location when the as-installed imperfections were used in the analysis. The as-installed geometric imperfections resulted in the analysis (of either pre- or posttest) with response closest to the experiment. Two posttest studies based on observed experimental response were conducted. The first was to use the radial midsurface position imperfection based on DIC data collected prior to beginning LS12, and the second was to induce bending over the 340° circumferential location as observed during LS12. Neither posttest study improved the test-analysis agreement over the pretest prediction based on the as-installed geometric imperfections. The observed continued axial displacements in the load lines during planned holds indicated one example of the test article differing from the FEM as-installed configuration and was not investigated through analysis. Other aspects of the test setup that could have contributed to potential test-analysis correlation differences and that were not investigated include uneven load application or less than ideal boundary conditions as observed through maximum bending over the 340° circumferential location, nonlinear material behavior as potentially observed through the nonlinear experimental load-displacement response, and material damage or failure as indicated by the audible emissions from the test article during loading. Each one of the aspects are known candidates for possible causes of nonlinearity and are left for possible future effort to enhance the analysis models. The difference between the FEM as-installed configuration and the experimental buckling load of 6.2% is considered quite reasonable given the suggested knockdown factor called for a suggested knockdown of 43.8%.

6.0 References

[1] Koiter, W. T., "On the Stability of Elastic Equilibrium," (in Dutch), H. J. Paris, Amsterdam, Holland, 1945; translation available as AFFDL-TR-70-25, February, 1970, Wright-Patterson Air Force Base.

[2] Anon., "Bucking of Thin Walled Circular Cylinders, NASA Space Vehicle Design Criteria," NASA SP-8007, November 2020.

[3] Hilburger, M. W. "Developing the Next Generation Shell Buckling Design Factors and Technologies," *53rd AIAA/ASME/ASCE/AHS/ASC Structures, Structural Dynamics, and Materials Conference,* AIAA 2012-1686, Honolulu, HI, April 23-26, 2012.

[4] Song, K., Schultz, M. R., Kosztowny, C. J. R., Przekop, A., Gardner, N. W., and Rudd, M. T., "Buckling Test and Analysis of the 8-Foot-Diameter Sandwich Composite Cylinder Test Article CTA8.3 as Part of the Shell Buckling Knockdown Factor Project: Test Dates 16-19 December 2019," NASA TM-20210024768, NASA Langley Research Center, Hampton, VA, January, 2022.

[5] Przekop, A., Schultz, M. R., Kosztowny, C. J. R., Gardner, N. W., Song, K., and Rudd, M. T., "Buckling Test and Analysis of the 8-Foot-Diameter Sandwich Composite Cylinder Test Article CTA8.2 as Part of the Shell Buckling Knockdown Factor Project: Test Dates 5-7 December 2017," NASA TM-20210024095, NASA Langley Research Center, Hampton, VA, May 2022.

[6] Schultz, M. R., Sleight, D. W., Gardner, N. W., Rudd, M. T., Hilburger, M. W., Palm, T., and Oldfield, N. J., "Test and Analysis of a Buckling-Critical Large-Scale Sandwich Composite Cylinder," *2018 AIAA SciTech Forum*, AIAA 2018-1693, Kissimmee, FL, January 8-12, 2018. doi: 10.2514/6.2018-1693.

[7] Schultz, M. R., and Kosztowny, C. J. R., "Shell Buckling Knockdown Factor Project SBKF-P3-CYL-CTA8.2B Test Plan 0.3 - Initial Release," NASA Langley Research Center, Hampton, VA, October 28, 2020.

[8] Hall, N., "Test and Checkout Procedure: Shell Buckling Knockdown Factor Project Test #13 CTA8.2B, SST-ED3.3-TCP-02," NASA Marshall Space Flight Center, Huntsville, AL, October 26, 2020.

[9] Hung, Y. Y. "Shearography: A New Optical Method For Strain Measurement And Nondestructive Testing," *Optical Engineering*, Vol. 21, No. 3, 1982. doi: 10.1117/12.7972920.

[10] Zhang, S. "High-Speed 3D Shape Measurement with Structured Light Methods: A Review," *Optics and Lasers in Engineering*, Vol. 106, February, 2018. doi: 10.1016/j.optlaseng.2018.02.017.

[11] Anon., Micorox Standard Grout Product Datasheet. https://www.micorco.com/wp-content/uploads/2014/03/Micorox-Standard-Grout-PDF-3-2014.pdf., retrieved August 26, 2021.

[12] Anon., Locktite Frekote 700-NC Technical Datasheet. http://tds.henkel.com/tds5/Studio/ShowPDF/243 NEW-EN?pid=FREKOTE 700NC&format=MTR&subformat=REAC&language=EN&plant=WERCS.pdf, retrieved

August 26, 2021.

[13] Bomarito, G. F., Hochhalter, J. D., and Ruggles, T. J. "Development of Optimal Multiscale Patterns for Digital Image Correlation via Local Grayscale Variation," *Experimental Mechanics*, Vol. 58, No. 7, November, 2018. doi: 10.1007/s11340-017-0348-1.

[14] Abaqus Standard, Software Package, Version 2018, SIMULIA, Providence, RI, 2018.

[15] Przekop, A., Schultz, M. R., Kosztowny, C. J. R., Song, K., Lindell, M. C., Hilburger, M. W., and Rudd, M. T., "Design and Analysis of Buckling-Critical Large-Scale Sandwich Composite Cylindrical Test Articles," NASA TM-20205008667, NASA Langley Research Center, Hampton, VA, November, 2020.

[16] Abaqus Analysis Guide, User Manual, Version 2018, SIMULIA, Providence, RI, 2018.

[17] Song, K., Satyanarayana, A., Przekop, A., and Schultz, M. R., "Development of a Numerical Modeling Approach for Buckling Analysis of Sandwich Composite Cylindrical Shells with Selected Results," NASA TM 20210013939, NASA Langley Research Center, Hampton, VA, April, 2021.

[18] Kosztowny, C. J. R. "Implementing Geometric Surface Imperfections into Sandwich Composite Cylinder Finite Element Method Models," AIAA 2021-0439, *2021 AIAA SciTech Forum*, January 19-21, 2021. doi: 10.2514/6.2021-0439.

Appendix – Drawings

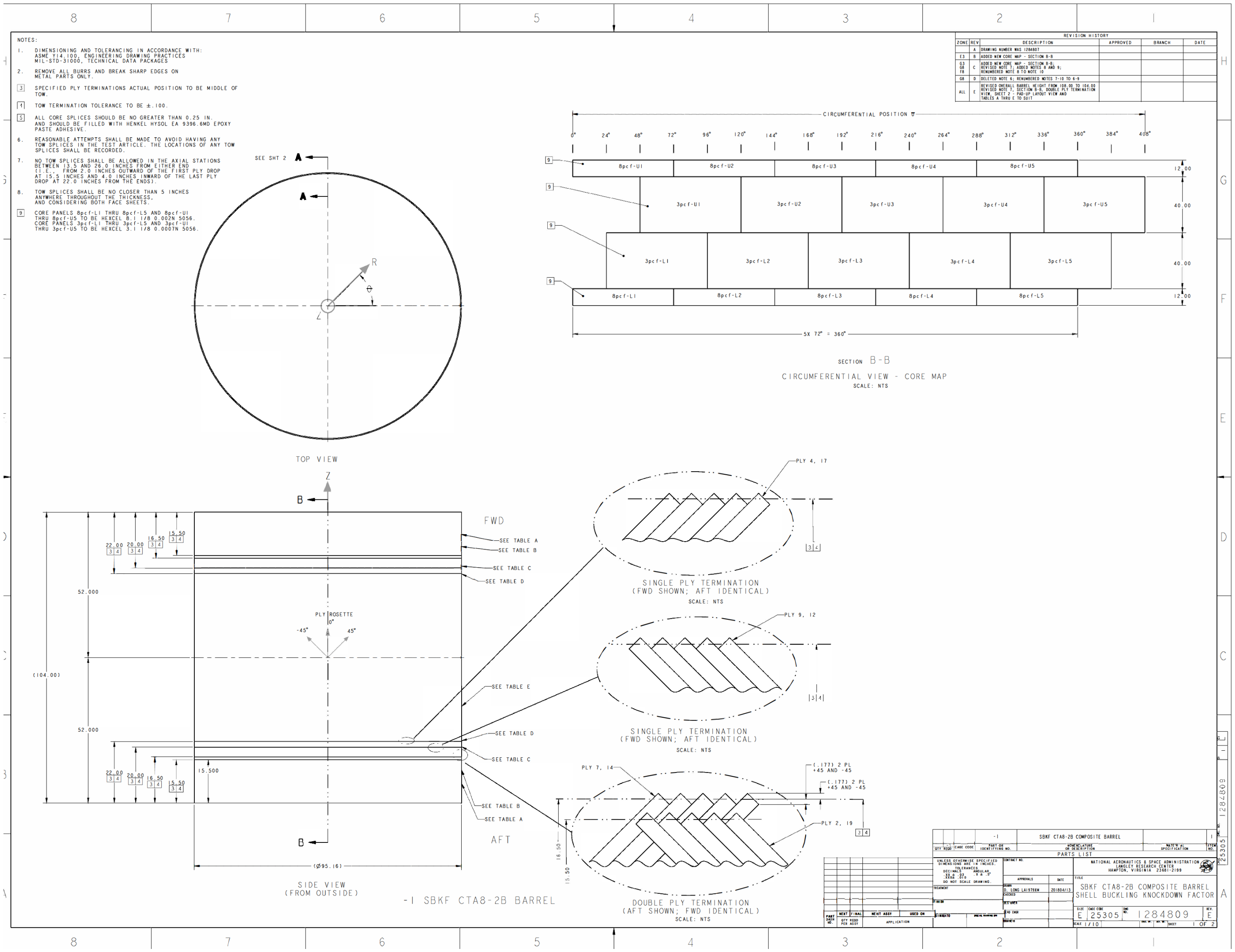

Figure 57. CTA8.2B fabrication drawing.

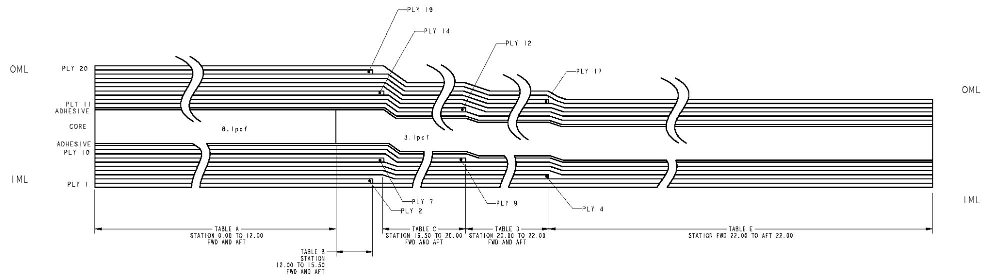

TABLE A
BETWEEN STATIONS 0.00 AND 12.00 (BOTH FWD AND AFT)

SEQUENCE	PLY NUMBER	MATERIAL	THICKNESS	ORIENTATION	COMMENTS
1	PLY 1	IM7/8552-1 190 gsm 0.5-in. tow	.0071	60	
2	PLY 2	IM7/8552-1 190 gsm 0.5-in. tow	.0071	-45	PADUP PLY
3	PLY 3	IM7/8552-1 190 gsm 0.5-in. tow	.0071	-60	
4	PLY 4	IM7/8552-1 190 gsm 0.5-in. tow	.0071	45	PADUP PLY
5	PLY 5	IM7/8552-1 190 gsm 0.5-in. tow	.0071	0	
6	PLY 6	IM7/8552-1 190 gsm 0.5-in. tow	.0071	0	
7	PLY 7	IM7/8552-1 190 gsm 0.5-in. tow	.0071	45	PADUP PLY
8	PLY 8	IM7/8552-1 190 gsm 0.5-in. tow	.0071	-60	
9	PLY 9	IM7/8552-1 190 gsm 0.5-in. tow	.0071	-45	PADUP PLY
10	PLY 10	IM7/8552-1 190 gsm 0.5-in. tow	.0071	60	
11	ADHESIVE FILM	CYTEC FM 300-2M 0.06 PSF	(.010)		FULL COVERAGE
12	CORE	HEXCEL 8.1 1/8 0.002N 5056	.200 ± .002		AS SHOWN
13	ADHESIVE FILM	CYTEC FM 300-2M 0.06 PSF	(.010)		FULL COVERAGE
14	PLY 11	IM7/8552-1 190 gsm 0.5-in. tow	.0071	60	
15	PLY 12	IM7/8552-1 190 gsm 0.5-in. tow	.0071	-45	PADUP PLY
16	PLY 13	IM7/8552-1 190 gsm 0.5-in. tow	.0071	-60	
17	PLY 14	IM7/8552-1 190 gsm 0.5-in. tow	.0071	45	PADUP PLY
18	PLY 15	IM7/8552-1 190 gsm 0.5-in. tow	.0071	0	
19	PLY 16	IM7/8552-1 190 gsm 0.5-in. tow	.0071	0	
20	PLY 17	IM7/8552-1 190 gsm 0.5-in. tow	.0071	45	PADUP PLY
21	PLY 18	IM7/8552-1 190 gsm 0.5-in. tow	.0071	-60	
22	PLY 19	IM7/8552-1 190 gsm 0.5-in. tow	.0071	-45	PADUP PLY
23	PLY 20	IM7/8552-1 190 gsm 0.5-in. tow	.0071	60	

TABLE B
BETWEEN STATIONS 12.00 AND 15.50 (BOTH FWD AND AFT)

SEQUENCE	PLY NUMBER	MATERIAL	THICKNESS	ORIENTATION	COMMENTS
1	PLY 1	IM7/8552-1 190 gsm 0.5-in. tow	.0071	60	
2	PLY 2	IM7/8552-1 190 gsm 0.5-in. tow	.0071	-45	PADUP PLY
3	PLY 3	IM7/8552-1 190 gsm 0.5-in. tow	.0071	-60	
4	PLY 4	IM7/8552-1 190 gsm 0.5-in. tow	.0071	45	PADUP PLY
5	PLY 5	IM7/8552-1 190 gsm 0.5-in. tow	.0071	0	
6	PLY 6	IM7/8552-1 190 gsm 0.5-in. tow	.0071	0	
7	PLY 7	IM7/8552-1 190 gsm 0.5-in. tow	.0071	45	PADUP PLY
8	PLY 8	IM7/8552-1 190 gsm 0.5-in. tow	.0071	-60	
9	PLY 9	IM7/8552-1 190 gsm 0.5-in. tow	.0071	-45	PADUP PLY
10	PLY 10	IM7/8552-1 190 gsm 0.5-in. tow	.0071	60	
11	ADHESIVE FILM	CYTEC FM 300-2M 0.06 PSF	(.010)		FULL COVERAGE
12	CORE	HEXCEL 3.1 1/8 0.0007N 5056	.200 ± .002		AS SHOWN
13	ADHESIVE FILM	CYTEC FM 300-2M 0.06 PSF	(.010)		FULL COVERAGE
14	PLY 11	IM7/8552-1 190 gsm 0.5-in. tow	.0071	60	
15	PLY 12	IM7/8552-1 190 gsm 0.5-in. tow	.0071	-45	PADUP PLY
16	PLY 13	IM7/8552-1 190 gsm 0.5-in. tow	.0071	-60	
17	PLY 14	IM7/8552-1 190 gsm 0.5-in. tow	.0071	45	PADUP PLY
18	PLY 15	IM7/8552-1 190 gsm 0.5-in. tow	.0071	0	
19	PLY 16	IM7/8552-1 190 gsm 0.5-in. tow	.0071	0	
20	PLY 17	IM7/8552-1 190 gsm 0.5-in. tow	.0071	45	PADUP PLY
21	PLY 18	IM7/8552-1 190 gsm 0.5-in. tow	.0071	-60	
22	PLY 19	IM7/8552-1 190 gsm 0.5-in. tow	.0071	-45	PADUP PLY
23	PLY 20	IM7/8552-1 190 gsm 0.5-in. tow	.0071	60	

TABLE C
BETWEEN STATIONS 16.50 - 20.00 (BOTH FWD AND AFT)

SEQUENCE	PLY NUMBER	MATERIAL	THICKNESS	ORIENTATION	COMMENTS
1	PLY 1	IM7/8552-1 190 gsm 0.5-in. tow	.0071	60	
2	PLY 3	IM7/8552-1 190 gsm 0.5-in. tow	.0071	-60	
3	PLY 4	IM7/8552-1 190 gsm 0.5-in. tow	.0071	45	PADUP PLY
4	PLY 5	IM7/8552-1 190 gsm 0.5-in. tow	.0071	0	
5	PLY 6	IM7/8552-1 190 gsm 0.5-in. tow	.0071	0	
6	PLY 8	IM7/8552-1 190 gsm 0.5-in. tow	.0071	-60	
7	PLY 9	IM7/8552-1 190 gsm 0.5-in. tow	.0071	-45	PADUP PLY
8	Ply.10	IM7/8552-1 190 gsm 0.5-in. tow	.0071	60	
9	ADHESIVE FILM	CYTEC FM 300-2M 0.06 PSF	(.010)		FULL COVERAGE
10	CORE	HEXCEL 3.1 1/8 0.0007N 5056	.200 ± .002		AS SHOWN
11	ADHESIVE FILM	CYTEC FM 300-2M 0.06 PSF	(.010)		FULL COVERAGE
12	PLY 11	IM7/8552-1 190 gsm 0.5-in. tow	.0071	60	
13	PLY 12	IM7/8552-1 190 gsm 0.5-in. tow	.0071	-45	PADUP PLY
14	PLY 13	IM7/8552-1 190 gsm 0.5-in. tow	.0071	-60	
15	PLY 15	IM7/8552-1 190 gsm 0.5-in. tow	.0071	0	
16	PLY 16	IM7/8552-1 190 gsm 0.5-in. tow	.0071	0	
17	PLY 17	IM7/8552-1 190 gsm 0.5-in. tow	.0071	45	PADUP PLY
18	PLY 18	IM7/8552-1 190 gsm 0.5-in. tow	.0071	-60	
19	PLY 20	IM7/8552-1 190 gsm 0.5-in. tow	.0071	60	

TABLE D
BETWEEN STATIONS 20.00 AND 22.00 (BOTH FWD AND AFT)

SEQUENCE	PLY NUMBER	MATERIAL	THICKNESS	ORIENTATION	COMMENTS
1	PLY 1	IM7/8552-1 190 gsm 0.5-in. tow	.0071	60	
2	PLY 3	IM7/8552-1 190 gsm 0.5-in. tow	.0071	-60	
3	PLY 4	IM7/8552-1 190 gsm 0.5-in. tow	.0071	45	PADUP PLY
4	PLY 5	IM7/8552-1 190 gsm 0.5-in. tow	.0071	0	
5	PLY 6	IM7/8552-1 190 gsm 0.5-in. tow	.0071	0	
6	PLY 8	IM7/8552-1 190 gsm 0.5-in. tow	.0071	-60	
7	PLY 10	IM7/8552-1 190 gsm 0.5-in. tow	.0071	60	
8	ADHESIVE FILM	CYTEC FM 300-2M 0.06 PSF	(.010)		FULL COVERAGE
9	CORE	HEXCEL 3.1 1/8 0.0007N 5056	.200 ± .002		AS SHOWN
10	ADHESIVE FILM	CYTEC FM 300-2M 0.06 PSF	(.010)		FULL COVERAGE
11	PLY 11	IM7/8552-1 190 gsm 0.5-in. tow	.0071	60	
12	PLY 13	IM7/8552-1 190 gsm 0.5-in. tow	.0071	-60	
13	PLY 15	IM7/8552-1 190 gsm 0.5-in. tow	.0071	0	
14	PLY 16	IM7/8552-1 190 gsm 0.5-in. tow	.0071	0	
15	PLY 17	IM7/8552-1 190 gsm 0.5-in. tow	.0071	45	PADUP PLY
16	PLY 18	IM7/8552-1 190 gsm 0.5-in. tow	.0071	-60	
17	PLY 20	IM7/8552-1 190 gsm 0.5-in. tow	.0071	60	

TABLE E
BETWEEN STATIONS FWD 22.00 AND AFT 22.00

SEQUENCE	PLY NUMBER	MATERIAL	THICKNESS	ORIENTATION	COMMENTS
1	PLY 1	IM7/8552-1 190 gsm 0.5-in. tow	.0071	60	
2	PLY 3	IM7/8552-1 190 gsm 0.5-in. tow	.0071	-60	
3	PLY 5	IM7/8552-1 190 gsm 0.5-in. tow	.0071	0	
4	PLY 6	IM7/8552-1 190 gsm 0.5-in. tow	.0071	0	
5	PLY 8	IM7/8552-1 190 gsm 0.5-in. tow	.0071	-60	
6	PLY 10	IM7/8552-1 190 gsm 0.5-in. tow	.0071	60	
7	ADHESIVE FILM	CYTEC FM 300-2M 0.06 PSF	(.010)		FULL COVERAGE
8	CORE	HEXCEL 3.1 1/8 0.0007N 5056	.200 ± .002		AS SHOWN
9	ADHESIVE FILM	CYTEC FM 300-2M 0.06 PSF	(.010)		FULL COVERAGE
10	PLY 11	IM7/8552-1 190 gsm 0.5-in. tow	.0071	60	
11	PLY 13	IM7/8552-1 190 gsm 0.5-in. tow	.0071	-60	
12	PLY 15	IM7/8552-1 190 gsm 0.5-in. tow	.0071	0	
13	PLY 16	IM7/8552-1 190 gsm 0.5-in. tow	.0071	0	
14	PLY 18	IM7/8552-1 190 gsm 0.5-in. tow	.0071	-60	
15	PLY 20	IM7/8552-1 190 gsm 0.5-in. tow	.0071	60	

NASA
LANGLEY RESEARCH CENTER
HAMPTON, VA 23681-2199

DRAWN D. LONG LA1978XM	SIZE E	CAGE CODE 25305	DWG. NO. 1284809	REV. E
CHECKED	SCALE NONE		SHEET 2 OF 2	

Figure 58. CTA8.2B layup drawing.

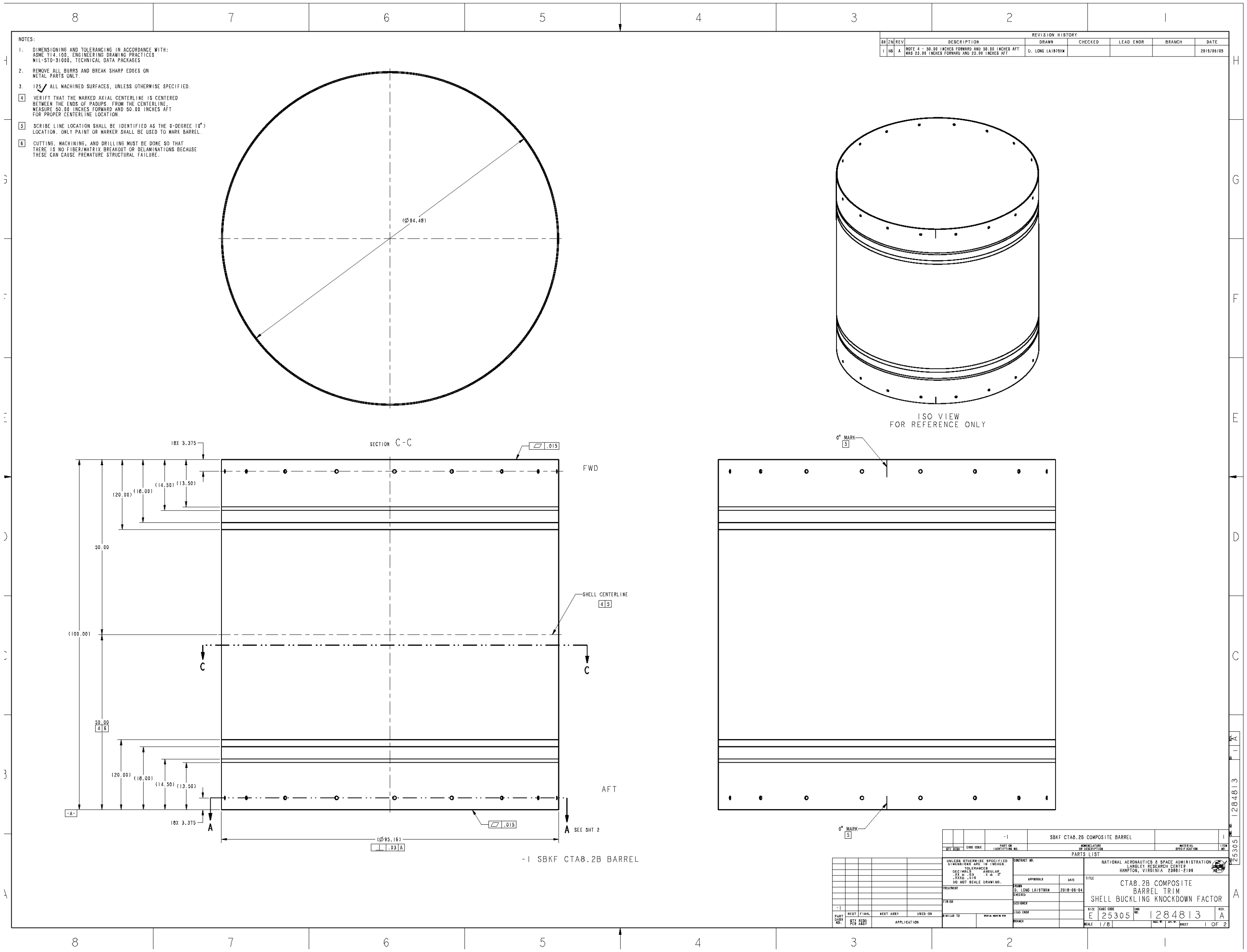

Figure 59. CTA8.2B trim drawing.

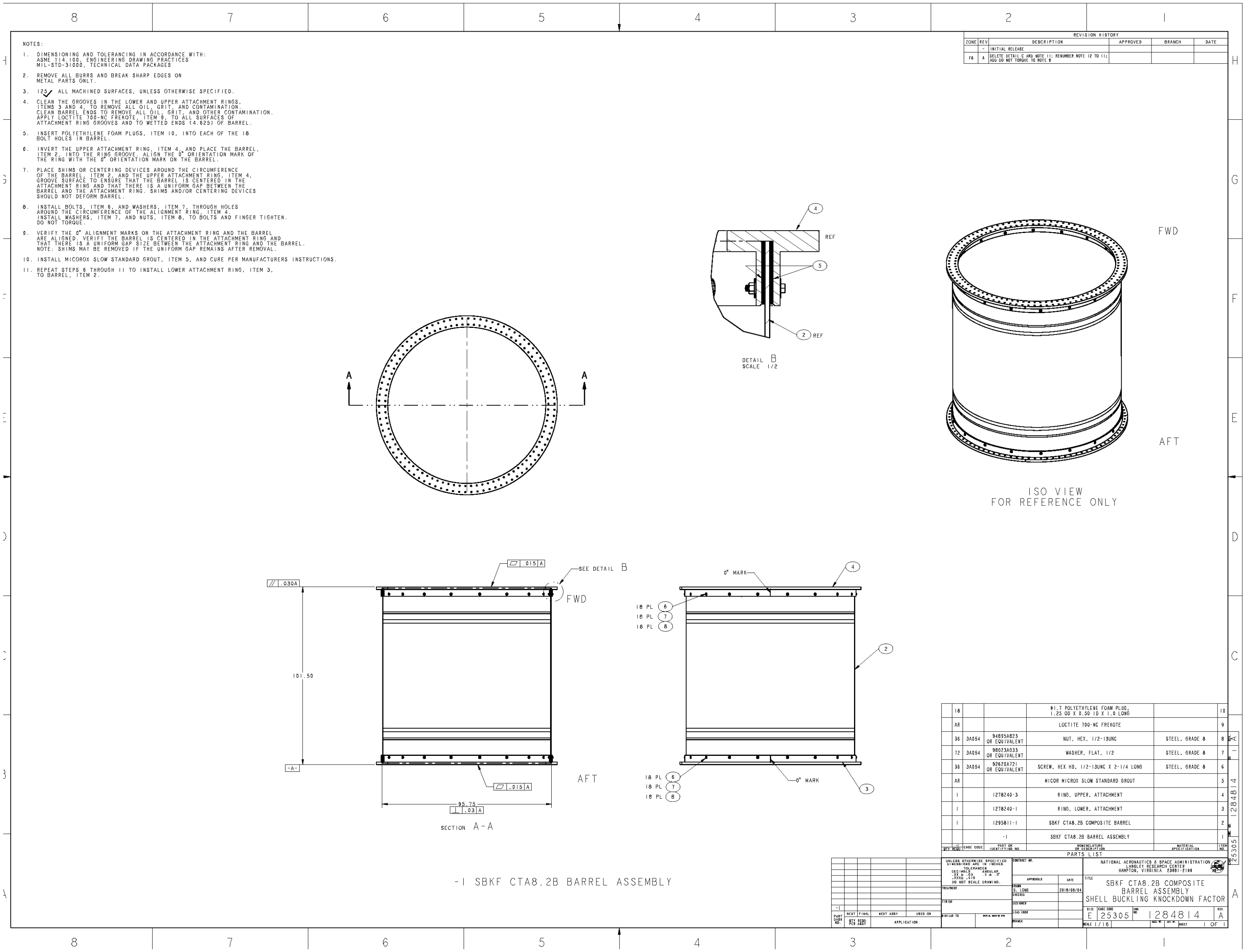

Figure 60. CTA8.2B assembly drawing.

REVISION HISTORY							
ZONE	REV	DESCRIPTION	DRAWN	CHECKED	LEAD ENGR	BRANCH	DATE

NOTES:

1. DIMENSIONING AND TOLERANCING IN ACCORDANCE WITH:
   ASME Y14.100, ENGINEERING DRAWING PRACTICES
   MIL-STD-31000, TECHNICAL DATA PACKAGES

$\boxed{2}$ ALL ODD NUMBERED GAGES ARE ON THE OML SURFACE. ALL EVEN NUMBER GAGES, SHOWN IN ( ) ON SHEET 2, ARE ON THE IML SURFACE.

$\boxed{3}$ ALL OML AND IML GAGES ARE NUMBERED FROM THE AFT END OF THE BARREL TO THE FWD END OF THE BARREL STARTING AT THE 0° HOOP POSITION.

$\boxed{4}$ THE CIRCUMFERENTIAL (HOOP) POSITIONS SHALL BE DETERMINED BY THE 4 TOOLING LINES ON THE IML AND 4 MEASURED LOCATIONS. THE 4 TOOLING LINES WILL BE 0, 90, 180, AND 270 DEGREE LINES. THE 4 MEASURED LOCATIONS WILL BE MARKED AS FOLLOWS:

A. MEASURE DISTANCE FROM 0 TO 90 DEGREE TOOLING LINES AT TOP, CENTER, AND BOTTOM.
B. AVERAGE THE MEASUREMENTS AND DIVIDE BY 2 TO GET THE 45 DEGREE LINE.
C. MARK THE 45 DEGREE LINE FROM TOP AND BOTTOM.
D. AVERAGE THE MEASUREMENTS AND DIVIDE BY 2 TO GET THE 22.5 DEGREE LINE.
E. MARK THE 22.5 DEGREE LINE FROM TOP AND BOTTOM.
F. REPEAT FOR 67.5, 112.5, 135, 157.5, 202.5, 225, 247.5, 292.5, 315 AND 337.5 DEGREE LINES.

$\boxed{5}$ ALL OML GAGES ARE TO BE POSITIONED BACK-TO-BACK WITH RESPECT TO THE CORRESPONDING IML GAGES.

OML - GAGE CHART

GAGE NO	GAGE TYPE	A - AXIAL H - HOOP	AXIAL DIMENSION ±.050 (FROM CENTERLINE)	HOOP POSITION
001	CEA-06-187UW-350	A	-44.5	0°
003A	CEA-06-125UT-350	A	-38	0°
003H	CEA-06-125UT-350	H	-38	0°
005	CEA-06-187UW-350	A	-34	0°
007	CEA-06-187UW-350	A	-31	0°
009	CEA-06-187UW-350	A	-29	0°
011	CEA-06-187UW-350	A	-14.5	0°
013A	CEA-06-125UT-350	A	0	0°
013H	CEA-06-125UT-350	H	0	0°
015	CEA-06-187UW-350	A	14.5	0°
017	CEA-06-187UW-350	A	29	0°
019	CEA-06-187UW-350	A	31	0°
021	CEA-06-187UW-350	A	34	0°
023A	CEA-06-125UT-350	A	38	0°
023H	CEA-06-125UT-350	H	38	0°
025	CEA-06-187UW-350	A	44.5	0°
027	CEA-06-187UW-350	A	-44.5	45°
029A	CEA-06-125UT-350	A	-38	45°
029H	CEA-06-125UT-350	H	-38	45°
031	CEA-06-187UW-350	A	-34	45°
033	CEA-06-187UW-350	A	-31	45°
035	CEA-06-187UW-350	A	-29	45°
037	CEA-06-187UW-350	A	-14.5	45°
039A	CEA-06-125UT-350	A	0	45°
039H	CEA-06-125UT-350	H	0	45°
041	CEA-06-187UW-350	A	14.5	45°
043	CEA-06-187UW-350	A	29	45°
045	CEA-06-187UW-350	A	31	45°
047	CEA-06-187UW-350	A	34	45°
049A	CEA-06-125UT-350	A	38	45°
049H	CEA-06-125UT-350	H	38	45°
051	CEA-06-187UW-350	A	44.5	45°
053	CEA-06-187UW-350	A	-44.5	90°
055A	CEA-06-125UT-350	A	-38	90°
055H	CEA-06-125UT-350	H	-38	90°
057	CEA-06-187UW-350	A	-34	90°
059	CEA-06-187UW-350	A	-31	90°
061	CEA-06-187UW-350	A	-29	90°
063	CEA-06-187UW-350	A	-14.5	90°
065A	CEA-06-125UT-350	A	0	90°
065H	CEA-06-125UT-350	H	0	90°
067	CEA-06-187UW-350	A	14.5	90°
069	CEA-06-187UW-350	A	29	90°
071	CEA-06-187UW-350	A	31	90°
073	CEA-06-187UW-350	A	34	90°
075A	CEA-06-125UT-350	A	38	90°
075H	CEA-06-125UT-350	H	38	90°
077	CEA-06-187UW-350	A	44.5	90°
079	CEA-06-187UW-350	A	-44.5	135°
081A	CEA-06-125UT-350	A	-38	135°
081H	CEA-06-125UT-350	H	-38	135°
083	CEA-06-187UW-350	A	-34	135°
085	CEA-06-187UW-350	A	-31	135°
087	CEA-06-187UW-350	A	-29	135°
089	CEA-06-187UW-350	A	-14.5	135°
091A	CEA-06-125UT-350	A	0	135°
091H	CEA-06-125UT-350	H	0	135°
093	CEA-06-187UW-350	A	14.5	135°
095	CEA-06-187UW-350	A	29	135°
097	CEA-06-187UW-350	A	31	135°
099	CEA-06-187UW-350	A	34	135°
101A	CEA-06-125UT-350	A	38	135°
101H	CEA-06-125UT-350	H	38	135°
103	CEA-06-187UW-350	A	44.5	135°

OML - GAGE CHART

GAGE NO	GAGE TYPE	A - AXIAL H - HOOP	AXIAL DIMENSION ±.050 (FROM CENTERLINE)	HOOP POSITION
105	CEA-06-187UW-350	A	-44.5	180°
107A	CEA-06-125UT-350	A	-38	180°
107H	CEA-06-125UT-350	H	-38	180°
109	CEA-06-187UW-350	A	-34	180°
111	CEA-06-187UW-350	A	-31	180°
113	CEA-06-187UW-350	A	-29	180°
115	CEA-06-187UW-350	A	-14.5	180°
117A	CEA-06-125UT-350	A	0	180°
117H	CEA-06-125UT-350	H	0	180°
119	CEA-06-187UW-350	A	14.5	180°
121	CEA-06-187UW-350	A	29	180°
123	CEA-06-187UW-350	A	31	180°
125	CEA-06-187UW-350	A	34	180°
127A	CEA-06-125UT-350	A	38	180°
127H	CEA-06-125UT-350	H	38	180°
129	CEA-06-187UW-350	A	44.5	180°
131	CEA-06-187UW-350	A	-44.5	225°
133A	CEA-06-125UT-350	A	-38	225°
133H	CEA-06-125UT-350	H	-38	225°
135	CEA-06-187UW-350	A	-34	225°
137	CEA-06-187UW-350	A	-31	225°
139	CEA-06-187UW-350	A	-29	225°
141	CEA-06-187UW-350	A	-14.5	225°
143A	CEA-06-125UT-350	A	0	225°
143H	CEA-06-125UT-350	H	0	225°
145	CEA-06-187UW-350	A	14.5	225°
147	CEA-06-187UW-350	A	29	225°
149	CEA-06-187UW-350	A	31	225°
151	CEA-06-187UW-350	A	34	225°
153A	CEA-06-125UT-350	A	38	225°
153H	CEA-06-125UT-350	H	38	225°
155	CEA-06-187UW-350	A	44.5	225°
157	CEA-06-187UW-350	A	-44.5	270°
159A	CEA-06-125UT-350	A	-38	270°
159H	CEA-06-125UT-350	H	-38	270°
161	CEA-06-187UW-350	A	-34	270°
163	CEA-06-187UW-350	A	-31	270°
165	CEA-06-187UW-350	A	-29	270°
167	CEA-06-187UW-350	A	-14.5	270°
169A	CEA-06-125UT-350	A	0	270°
169H	CEA-06-125UT-350	H	0	270°
171	CEA-06-187UW-350	A	14.5	270°
173	CEA-06-187UW-350	A	29	270°
175	CEA-06-187UW-350	A	31	270°
177	CEA-06-187UW-350	A	34	270°
179A	CEA-06-125UT-350	A	38	270°
179H	CEA-06-125UT-350	H	38	270°
181	CEA-06-187UW-350	A	44.5	270°
183	CEA-06-187UW-350	A	-44.5	315°
185A	CEA-06-125UT-350	A	-38	315°
185H	CEA-06-125UT-350	H	-38	315°
187	CEA-06-187UW-350	A	-34	315°
189	CEA-06-187UW-350	A	-31	315°
191	CEA-06-187UW-350	A	-29	315°
193	CEA-06-187UW-350	A	-14.5	315°
195A	CEA-06-125UT-350	A	0	315°
195H	CEA-06-125UT-350	H	0	315°
197	CEA-06-187UW-350	A	14.5	315°
199	CEA-06-187UW-350	A	29	315°
201	CEA-06-187UW-350	A	31	315°
203	CEA-06-187UW-350	A	34	315°
205A	CEA-06-125UT-350	A	38	315°
205H	CEA-06-125UT-350	H	38	315°
207	CEA-06-187UW-350	A	44.5	315°

OML - GAGE CHART

GAGE NO	GAGE TYPE	A - AXIAL H - HOOP	AXIAL DIMENSION ±.050 (FROM CENTERLINE)	HOOP POSITION
209	CEA-06-187UW-350	A	-44.5	22.5°
211	CEA-06-187UW-350	A	44.5	22.5°
213	CEA-06-187UW-350	A	-44.5	67.5°
215	CEA-06-187UW-350	A	44.5	67.5°
217	CEA-06-187UW-350	A	-44.5	112.5°
219	CEA-06-187UW-350	A	44.5	112.5°
221	CEA-06-187UW-350	A	-44.5	157.5°
223	CEA-06-187UW-350	A	44.5	157.5°
225	CEA-06-187UW-350	A	-44.5	202.5°
227	CEA-06-187UW-350	A	44.5	202.5°
229	CEA-06-187UW-350	A	-44.5	247.5°
231	CEA-06-187UW-350	A	44.5	247.5°
233	CEA-06-187UW-350	A	-44.5	292.5°
235	CEA-06-187UW-350	A	44.5	292.5°
237	CEA-06-187UW-350	A	-44.5	337.5°
239	CEA-06-187UW-350	A	44.5	337.5°

IML - GAGE CHART

GAGE NO	GAGE TYPE	A - AXIAL H - HOOP	AXIAL DIMENSION ±.050 (FROM CENTERLINE)	HOOP POSITION
002	CEA-06-187UW-350	A	-44.5	0°
004A	CEA-06-125UT-350	A	-38	0°
004H	CEA-06-125UT-350	H	-38	0°
006	CEA-06-187UW-350	A	-34	0°
008	CEA-06-187UW-350	A	-31	0°
010	CEA-06-187UW-350	A	-29	0°
012	CEA-06-187UW-350	A	-14.5	0°
014A	CEA-06-125UT-350	A	0	0°
014H	CEA-06-125UT-350	H	0	0°
016	CEA-06-187UW-350	A	14.5	0°
018	CEA-06-187UW-350	A	29	0°
020	CEA-06-187UW-350	A	31	0°
022	CEA-06-187UW-350	A	34	0°
024A	CEA-06-125UT-350	A	38	0°
024H	CEA-06-125UT-350	H	38	0°
026	CEA-06-187UW-350	A	44.5	0°
028	CEA-06-187UW-350	A	-44.5	45°
030A	CEA-06-125UT-350	A	-38	45°
030H	CEA-06-125UT-350	H	-38	45°
032	CEA-06-187UW-350	A	-34	45°
034	CEA-06-187UW-350	A	-31	45°
036	CEA-06-187UW-350	A	-29	45°
038	CEA-06-187UW-350	A	-14.5	45°
040A	CEA-06-125UT-350	A	0	45°
040H	CEA-06-125UT-350	H	0	45°
042	CEA-06-187UW-350	A	14.5	45°
044	CEA-06-187UW-350	A	29	45°
046	CEA-06-187UW-350	A	31	45°
048	CEA-06-187UW-350	A	0034	45°
050A	CEA-06-125UT-350	A	38	45°
050H	CEA-06-125UT-350	H	38	45°
052	CEA-06-187UW-350	A	44.5	45°
054	CEA-06-187UW-350	A	-44.5	90°
056A	CEA-06-125UT-350	A	-38	90°
056H	CEA-06-125UT-350	H	-38	90°
058	CEA-06-187UW-350	A	-34	90°
060	CEA-06-187UW-350	A	-31	90°
062	CEA-06-187UW-350	A	-29	90°
064	CEA-06-187UW-350	A	-14.5	90°
066A	CEA-06-125UT-350	A	0	90°
066H	CEA-06-125UT-350	H	0	90°
068	CEA-06-187UW-350	A	14.5	90°
070	CEA-06-187UW-350	A	29	90°
072	CEA-06-187UW-350	A	31	90°
074	CEA-06-187UW-350	A	34	90°
076A	CEA-06-125UT-350	A	38	90°
076H	CEA-06-125UT-350	H	38	90°
078	CEA-06-187UW-350	A	44.5	90°
080	CEA-06-187UW-350	A	-44.5	135°
082A	CEA-06-125UT-350	A	-38	135°
082H	CEA-06-125UT-350	H	-38	135°
084	CEA-06-187UW-350	A	-34	135°
086	CEA-06-187UW-350	A	-31	135°
088	CEA-06-187UW-350	A	-29	135°
090	CEA-06-187UW-350	A	-14.5	135°
092A	CEA-06-125UT-350	A	0	135°
092H	CEA-06-125UT-350	H	0	135°
094	CEA-06-187UW-350	A	14.5	135°
096	CEA-06-187UW-350	A	29	135°
098	CEA-06-187UW-350	A	31	135°
100	CEA-06-187UW-350	A	34	135°
102A	CEA-06-125UT-350	A	38	135°
102H	CEA-06-125UT-350	H	38	135°
104	CEA-06-187UW-350	A	44.5	135°

IML - GAGE CHART

GAGE NO	GAGE TYPE	A - AXIAL H - HOOP	AXIAL DIMENSION ±.050 (FROM CENTERLINE)	HOOP POSITION
106	CEA-06-187UW-350	A	-44.5	180°
108A	CEA-06-125UT-350	A	-38	180°
108H	CEA-06-125UT-350	H	-38	180°
110	CEA-06-187UW-350	A	-34	180°
112	CEA-06-187UW-350	A	-31	180°
114	CEA-06-187UW-350	A	-29	180°
116	CEA-06-187UW-350	A	-14.5	180°
118A	CEA-06-125UT-350	A	0	180°
118H	CEA-06-125UT-350	H	0	180°
120	CEA-06-187UW-350	A	14.5	180°
122	CEA-06-187UW-350	A	29	180°
124	CEA-06-187UW-350	A	31	180°
126	CEA-06-187UW-350	A	34	180°
128A	CEA-06-125UT-350	A	38	180°
128H	CEA-06-125UT-350	H	38	180°
130	CEA-06-187UW-350	A	44.5	180°
132	CEA-06-187UW-350	A	-44.5	225°
134A	CEA-06-125UT-350	A	-38	225°
134H	CEA-06-125UT-350	H	-38	225°
136	CEA-06-187UW-350	A	-34	225°
138	CEA-06-187UW-350	A	-31	225°
140	CEA-06-187UW-350	A	-29	225°
142	CEA-06-187UW-350	A	-14.5	225°
144A	CEA-06-125UT-350	A	0	225°
144H	CEA-06-125UT-350	H	0	225°
146	CEA-06-187UW-350	A	14.5	225°
148	CEA-06-187UW-350	A	29	225°
150	CEA-06-187UW-350	A	31	225°
152	CEA-06-187UW-350	A	34	225°
154A	CEA-06-125UT-350	A	38	225°
154H	CEA-06-125UT-350	H	38	225°
156	CEA-06-187UW-350	A	44.5	225°
158	CEA-06-187UW-350	A	-44.5	270°
160A	CEA-06-125UT-350	A	-38	270°
160H	CEA-06-125UT-350	H	-38	270°
162	CEA-06-187UW-350	A	-34	270°
164	CEA-06-187UW-350	A	-31	270°
166	CEA-06-187UW-350	A	-29	270°
168	CEA-06-187UW-350	A	-14.5	270°
170A	CEA-06-125UT-350	A	0	270°
170H	CEA-06-125UT-350	H	0	270°
172	CEA-06-187UW-350	A	14.5	270°
174	CEA-06-187UW-350	A	29	270°
176	CEA-06-187UW-350	A	31	270°
178	CEA-06-187UW-350	A	34	270°
180A	CEA-06-125UT-350	A	38	270°
180H	CEA-06-125UT-350	H	38	270°
182	CEA-06-187UW-350	A	44.5	270°
184	CEA-06-187UW-350	A	-44.5	315°
186A	CEA-06-125UT-350	A	-38	315°
186H	CEA-06-125UT-350	H	-38	315°
188	CEA-06-187UW-350	A	-34	315°
190	CEA-06-187UW-350	A	-31	315°
192	CEA-06-187UW-350	A	-29	315°
194	CEA-06-187UW-350	A	-14.5	315°
196A	CEA-06-125UT-350	A	0	315°
196H	CEA-06-125UT-350	H	0	315°
198	CEA-06-187UW-350	A	14.5	315°
200	CEA-06-187UW-350	A	29	315°
202	CEA-06-187UW-350	A	31	315°
204	CEA-06-187UW-350	A	34	315°
206A	CEA-06-125UT-350	A	38	315°
206H	CEA-06-125UT-350	H	38	315°
208	CEA-06-187UW-350	A	44.5	315°

IML - GAGE CHART

GAGE NO	GAGE TYPE	A - AXIAL H - HOOP	AXIAL DIMENSION ±.050 (FROM CENTERLINE)	HOOP POSITION
210	CEA-06-187UW-350	A	-44.5	22.5°
212	CEA-06-187UW-350	A	44.5	22.5°
214	CEA-06-187UW-350	A	-44.5	67.5°
216	CEA-06-187UW-350	A	44.5	67.5°
218	CEA-06-187UW-350	A	-44.5	112.5°
220	CEA-06-187UW-350	A	44.5	112.5°
222	CEA-06-187UW-350	A	-44.5	157.5°
224	CEA-06-187UW-350	A	44.5	157.5°
226	CEA-06-187UW-350	A	-44.5	202.5°
228	CEA-06-187UW-350	A	44.5	202.5°
230	CEA-06-187UW-350	A	-44.5	247.5°
232	CEA-06-187UW-350	A	44.5	247.5°
234	CEA-06-187UW-350	A	-44.5	292.5°
236	CEA-06-187UW-350	A	44.5	292.5°
238	CEA-06-187UW-350	A	-44.5	337.5°
240	CEA-06-187UW-350	A	44.5	337.5°

ALL SHEETS ARE REV LEVEL -

PARTS LIST

QTY REQD	CAGE CODE	PART OR IDENTIFYING NO.	NOMENCLATURE OR DESCRIPTION	MATERIAL SPECIFICATION	ITEM NO.
48		CEA-06-125UT-350	STRAIN GAUGE, 350 OHM, TEE		3
192		CEA-06-187UW-350	STRAIN GAUGE, 350 OHM, UNIAXIAL		2
1		1284814-1	CTA8.2B BARREL ASSEMBLY	MATERIAL:5 MATERIAL2:5	1

PART DASH NO.	QTY REQD PER ASSY NEXT	QTY REQD PER ASSY FINAL	APPLICATION NEXT ASSY	APPLICATION USED ON
-1		1	FINAL	SBKF CTA8.2B

UNLESS OTHERWISE SPECIFIED DIMENSIONS ARE IN INCHES.
TOLERANCES
DECIMALS .XX ± .03 .XXX± .010
ANGULAR .X ± .5°
DO NOT SCALE DRAWING.

TREATMENT

FINISH

SIMILAR TO

SPECIAL MARKING STD

CONTRACT NO.

APPROVALS	DATE
DRAWN D. LONG LAI9T9XM	2019-11-07
CHECKED	
DESIGNER	
LEAD ENGR	
BRANCH	

NATIONAL AERONAUTICS & SPACE ADMINISTRATION
LANGLEY RESEARCH CENTER
HAMPTON, VIRGINIA 23681-2199

TITLE
SBKF CTA8.2B
COMPOSITE BARREL
INSTRUMENTATION ASSEMBLY

SIZE E | CAGE CODE 25305 | DWG NO. 1286637 | REV. -
SCALE 1/8 | CALC. WT. | ACT. WT. | SHEET 1 OF 2

CAGE 25305 | DWG. NO. 1286637 | SH 1 | REV. -

Figure 61. CTA8.2B instrumentation tables.

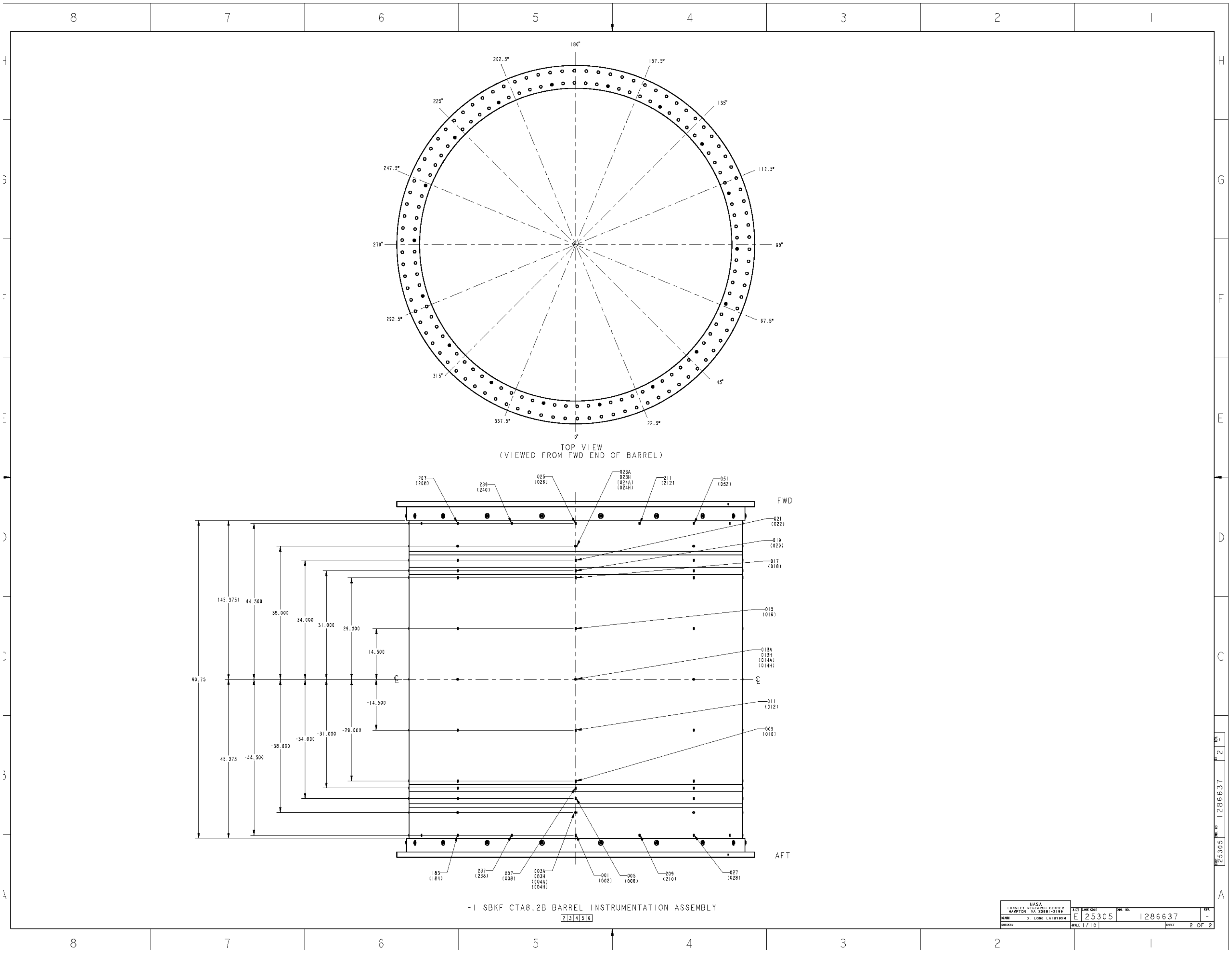

Figure 62. CTA8.2B instrumentation drawing.

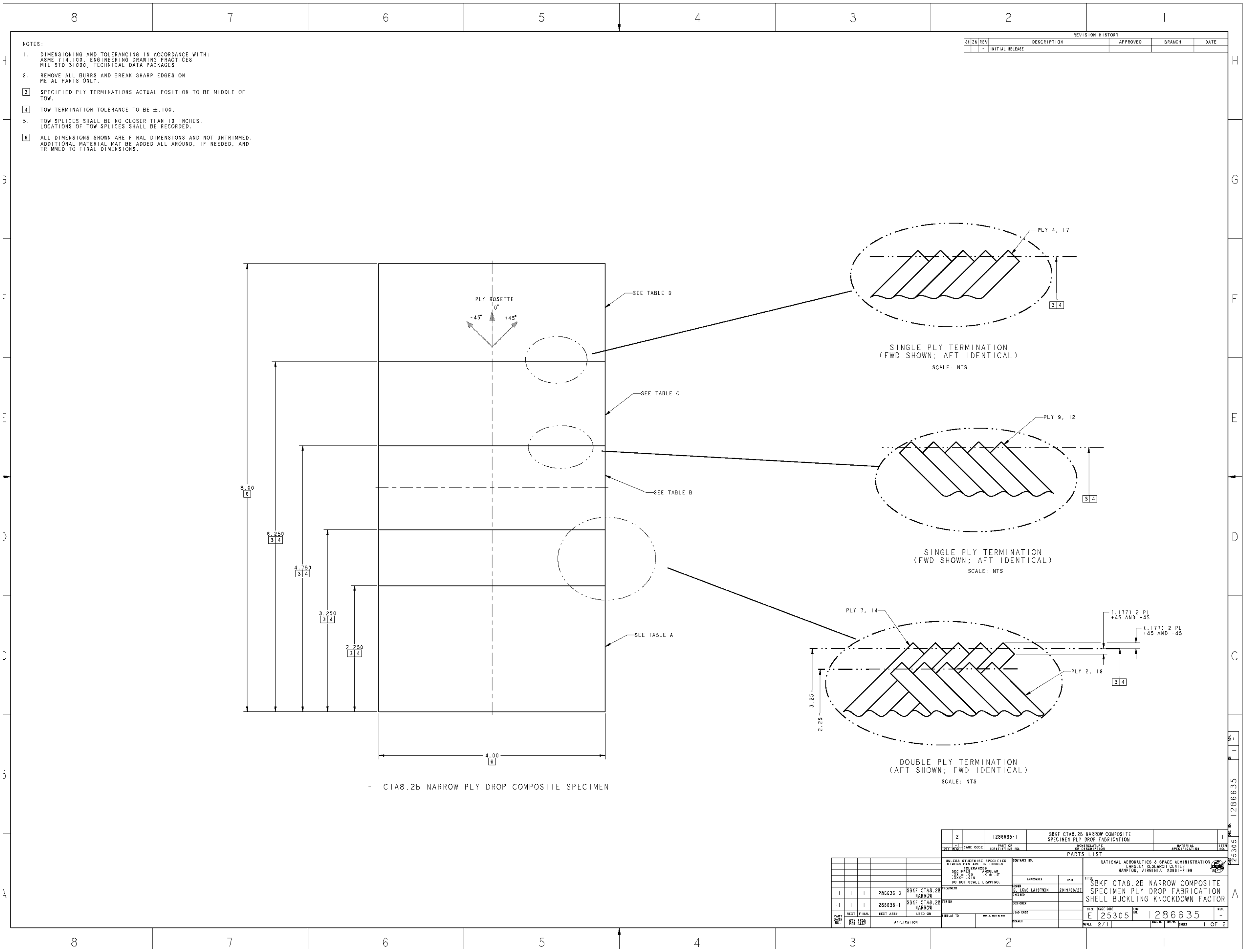

Figure 63. CTA8.2B ply drop specimen drawing.

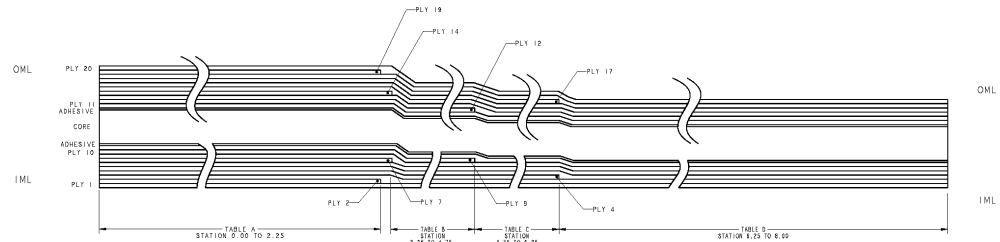

PAD-UP LAYOUT
SCALE: NTS

TABLE A
BETWEEN STATIONS 0 TO 2.25

SEQUENCE	PLY NUMBER	MATERIAL	THICKNESS	ORIENTATION	COMMENTS
1	PLY 1	IM7/8552-1 190 gsm 0.5-in. tow	.0071	60	
2	PLY 2	IM7/8552-1 190 gsm 0.5-in. tow	.0071	-45	PADUP PLY
3	PLY 3	IM7/8552-1 190 gsm 0.5-in. tow	.0071	-60	
4	PLY 4	IM7/8552-1 190 gsm 0.5-in. tow	.0071	45	PADUP PLY
5	PLY 5	IM7/8552-1 190 gsm 0.5-in. tow	.0071	0	
6	PLY 6	IM7/8552-1 190 gsm 0.5-in. tow	.0071	0	
7	PLY 7	IM7/8552-1 190 gsm 0.5-in. tow	.0071	45	PADUP PLY
8	PLY 8	IM7/8552-1 190 gsm 0.5-in. tow	.0071	-60	
9	PLY 9	IM7/8552-1 190 gsm 0.5-in. tow	.0071	-45	PADUP PLY
10	PLY 10	IM7/8552-1 190 gsm 0.5-in. tow	.0071	60	
11	ADHESIVE FILM	CYTEC FM 300-2M 0.06 PSF	(.010)		FULL COVERAGE
12	CORE	HEXCEL 3.1 1/8 0.0007N 5056	.200 ±.002		AS SHOWN
13	ADHESIVE FILM	CYTEC FM 300-2M 0.06 PSF	(.010)		FULL COVERAGE
14	PLY 11	IM7/8552-1 190 gsm 0.5-in. tow	.0071	60	
15	PLY 12	IM7/8552-1 190 gsm 0.5-in. tow	.0071	-45	PADUP PLY
16	PLY 13	IM7/8552-1 190 gsm 0.5-in. tow	.0071	-60	
17	PLY 14	IM7/8552-1 190 gsm 0.5-in. tow	.0071	45	PADUP PLY
18	PLY 15	IM7/8552-1 190 gsm 0.5-in. tow	.0071	0	
19	PLY 16	IM7/8552-1 190 gsm 0.5-in. tow	.0071	0	
20	PLY 17	IM7/8552-1 190 gsm 0.5-in. tow	.0071	45	PADUP PLY
21	PLY 18	IM7/8552-1 190 gsm 0.5-in. tow	.0071	-60	
22	PLY 19	IM7/8552-1 190 gsm 0.5-in. tow	.0071	-45	PADUP PLY
23	PLY 20	IM7/8552-1 190 gsm 0.5-in. tow	.0071	60	

TABLE B
BETWEEN STATION 3.25 - 4.75

SEQUENCE	PLY NUMBER	MATERIAL	THICKNESS	ORIENTATION	COMMENTS
1	PLY 1	IM7/8552-1 190 gsm 0.5-in. tow	.0071	60	
2	PLY 3	IM7/8552-1 190 gsm 0.5-in. tow	.0071	-60	
3	PLY 4	IM7/8552-1 190 gsm 0.5-in. tow	.0071	45	PADUP PLY
4	PLY 5	IM7/8552-1 190 gsm 0.5-in. tow	.0071	0	
5	PLY 6	IM7/8552-1 190 gsm 0.5-in. tow	.0071	0	
6	PLY 8	IM7/8552-1 190 gsm 0.5-in. tow	.0071	-60	
7	PLY 9	IM7/8552-1 190 gsm 0.5-in. tow	.0071	-45	PADUP PLY
8	Ply.10	IM7/8552-1 190 gsm 0.5-in. tow	.0071	60	
9	ADHESIVE FILM	CYTEC FM 300-2M 0.06 PSF	(.010)		FULL COVERAGE
10	CORE	HEXCEL 3.1 1/8 0.0007N 5056	.200 ±.002		AS SHOWN
11	ADHESIVE FILM	CYTEC FM 300-2M 0.06 PSF	(.010)		FULL COVERAGE
12	PLY 11	IM7/8552-1 190 gsm 0.5-in. tow	.0071	60	
13	PLY 12	IM7/8552-1 190 gsm 0.5-in. tow	.0071	-45	PADUP PLY
14	PLY 13	IM7/8552-1 190 gsm 0.5-in. tow	.0071	-60	
15	PLY 15	IM7/8552-1 190 gsm 0.5-in. tow	.0071	0	
16	PLY 16	IM7/8552-1 190 gsm 0.5-in. tow	.0071	0	
17	PLY 17	IM7/8552-1 190 gsm 0.5-in. tow	.0071	45	PADUP PLY
18	PLY 18	IM7/8552-1 190 gsm 0.5-in. tow	.0071	-60	
19	PLY 20	IM7/8552-1 190 gsm 0.5-in. tow	.0071	60	

TABLE C
BETWEEN STATION 4.75 TO 6.25

SEQUENCE	PLY NUMBER	MATERIAL	THICKNESS	ORIENTATION	COMMENTS
1	PLY 1	IM7/8552-1 190 gsm 0.5-in. tow	.0071	60	
2	PLY 3	IM7/8552-1 190 gsm 0.5-in. tow	.0071	-60	
3	PLY 4	IM7/8552-1 190 gsm 0.5-in. tow	.0071	45	PADUP PLY
4	PLY 5	IM7/8552-1 190 gsm 0.5-in. tow	.0071	0	
5	PLY 6	IM7/8552-1 190 gsm 0.5-in. tow	.0071	0	
6	PLY 8	IM7/8552-1 190 gsm 0.5-in. tow	.0071	-60	
7	PLY 10	IM7/8552-1 190 gsm 0.5-in. tow	.0071	60	
8	ADHESIVE FILM	CYTEC FM 300-2M 0.06 PSF	(.010)		FULL COVERAGE
9	CORE	HEXCEL 3.1 1/8 0.0007N 5056	.200 ±.002		AS SHOWN
10	ADHESIVE FILM	CYTEC FM 300-2M 0.06 PSF	(.010)		FULL COVERAGE
11	PLY 11	IM7/8552-1 190 gsm 0.5-in. tow	.0071	60	
12	PLY 13	IM7/8552-1 190 gsm 0.5-in. tow	.0071	-60	
13	PLY 15	IM7/8552-1 190 gsm 0.5-in. tow	.0071	0	
14	PLY 16	IM7/8552-1 190 gsm 0.5-in. tow	.0071	0	
15	PLY 17	IM7/8552-1 190 gsm 0.5-in. tow	.0071	45	PADUP PLY
16	PLY 18	IM7/8552-1 190 gsm 0.5-in. tow	.0071	-60	
17	PLY 20	IM7/8552-1 190 gsm 0.5-in. tow	.0071	60	

TABLE D
BETWEEN STATION 6.25 TO 8.00

SEQUENCE	PLY NUMBER	MATERIAL	THICKNESS	ORIENTATION	COMMENTS
1	PLY 1	IM7/8552-1 190 gsm 0.5-in. tow	.0071	60	
2	PLY 3	IM7/8552-1 190 gsm 0.5-in. tow	.0071	-60	
3	PLY 5	IM7/8552-1 190 gsm 0.5-in. tow	.0071	0	
4	PLY 6	IM7/8552-1 190 gsm 0.5-in. tow	.0071	0	
5	PLY 8	IM7/8552-1 190 gsm 0.5-in. tow	.0071	-60	
6	PLY 10	IM7/8552-1 190 gsm 0.5-in. tow	.0071	60	
7	ADHESIVE FILM	CYTEC FM 300-2M 0.06 PSF	(.010)		FULL COVERAGE
8	CORE	HEXCEL 3.1 1/8 0.0007N 5056	.200 ±.002		AS SHOWN
9	ADHESIVE FILM	CYTEC FM 300-2M 0.06 PSF	(.010)		FULL COVERAGE
10	PLY 11	IM7/8552-1 190 gsm 0.5-in. tow	.0071	60	
11	PLY 13	IM7/8552-1 190 gsm 0.5-in. tow	.0071	-60	
12	PLY 15	IM7/8552-1 190 gsm 0.5-in. tow	.0071	0	
13	PLY 16	IM7/8552-1 190 gsm 0.5-in. tow	.0071	0	
14	PLY 18	IM7/8552-1 190 gsm 0.5-in. tow	.0071	-60	
15	PLY 20	IM7/8552-1 190 gsm 0.5-in. tow	.0071	60	

NASA
LANGLEY RESEARCH CENTER
HAMPTON, VA 23681-2199

DRAWN D. LONG LA1978XN	SIZE E	CAGE CODE 25305	DWG. NO. 1286635	REV. -
CHECKED	SCALE NONE		SHEET 2 OF 2	

Figure 64. CTA8.2B ply drop specimen layup drawing.